

QUASARS PROBING QUASARS VIII. THE PHYSICAL PROPERTIES OF THE COOL CIRCUMGALACTIC MEDIUM SURROUNDING $z \sim 2-3$ MASSIVE GALAXIES HOSTING QUASARSMARIE WINGYEE LAU^{1,2}, J. XAVIER PROCHASKA², JOSEPH F. HENNAWT³*Draft version August 15, 2016*

ABSTRACT

We characterize the physical properties of the cool $T \sim 10^4$ K circumgalactic medium surrounding $z \sim 2-3$ quasar host galaxies, which are predicted to evolve into present day massive ellipticals. Using a statistical sample of 14 quasar pairs with projected separation < 300 kpc and high dispersion, high S/N spectra, we find extreme kinematics with low metal ion lines typically spanning ≈ 500 km s⁻¹, exceeding any previously studied galactic population. The CGM is significantly enriched, even beyond the virial radius, with a median metallicity $[M/H] \approx -0.6$. The α/Fe abundance ratio is enhanced, suggesting that halo gas is primarily enriched by core-collapse supernovae. The projected cool gas mass within the virial radius is estimated to be $1.9 \times 10^{11} M_\odot (R_\perp/160 \text{ kpc})^2$, accounting for $\approx 1/3$ of the galaxy halo baryonic budget. The ionization state of CGM gas increases with projected distance from the foreground quasars, contrary to expectation if the quasar dominates the ionizing radiation flux. However, we also found peculiarities not exhibited in the CGM of other galaxy populations. In one absorption system, we may be detecting unresolved fluorescent Ly α emission, and another system shows strong N V lines. Taken together these anomalies suggest that transverse sightlines are at least in some cases possibly illuminated. We also discovered a peculiar case where detection of the C II fine structure line implies an electron density $> 100 \text{ cm}^{-3}$ and subparsec scale gas clumps.

Subject headings: galaxies: formation – galaxies: halos – galaxies: clusters: intracluster medium – intergalactic medium – quasars: general – quasars: absorption lines

1. INTRODUCTION

The circumgalactic medium (CGM) is defined as the gaseous halo extending approximately 20–300 kpc from galaxies. It is the site of interplay between outflows from galaxies and accretion onto galaxies. Together these flows fuel, drain, heat, and enrich the CGM of dark matter halos. The impact of these processes on galaxy evolution and the enrichment of the intergalactic medium (IGM) remain open questions. The hot-phase CGM, or the intracluster medium, has been detected in X-rays at $z \lesssim 1$ from the halos of massive galaxy clusters (e.g. Kravtsov & Borgani 2012; Sato et al. 2007; Mushotzky et al. 1996). A warm-hot phase CGM traced by O VI is also observed for individual galaxy halos (Tumlinson et al. 2011; Peeples et al. 2014). The cool phase CGM, however, is typically too diffuse or low mass to directly detect far beyond the Local Group (e.g. Oosterloo et al. 2007; Oosterloo & van Gorkom 2005). Instead, one is compelled to search in absorption using background sources whose sightlines pass close to foreground galaxies (e.g. Bergeron & Boisse 1991; Lanzetta et al. 1995; Chen et al. 2010; Prochaska et al. 2011).

Our understanding of the low- z CGM is greatly advanced by the COS-Halos survey. The survey presented a statistical sample of high dispersion spectra that resolve the H I Lyman series and many diagnostic metal ion transition lines of the CGM surrounding L^* galaxies. The COS-Halos survey has demonstrated that, in

addition to being a mediator for baryon recycling between galaxies and the intergalactic medium, the CGM also carries a significant portion of the baryonic budget of galaxy halos. Thus the CGM is essential in addressing the galaxy halo missing baryon problem (Tumlinson et al. 2013; Werk et al. 2014).

In the low- z universe, outflows preferentially occur in star forming galaxies with appreciable star formation rates (Rupke et al. 2005; Martin 2005; Rubin et al. 2014). At higher redshifts, when the star formation density is higher, these galactic winds occur for galaxies of a wide range in mass (Rubin et al. 2010; Steidel et al. 2010). The cold inflows onto galaxies are also predicted to be more important at higher redshifts as they feed and regulate the higher star formation rates (Kereš et al. 2005; Erb 2008). In addition, at $z \sim 2-3$, when both the universal star formation rate and active galactic nuclei activity peak, theories have predicted quasar driven outflows may couple with galaxy evolution by injecting heat into the CGM (Scannapieco & Oh 2004; Hopkins et al. 2008). Because of the difficulty in obtaining spectra of faint galaxies, previous studies on the CGM at high- z have been largely confined to low dispersion, stacked spectra (Adelberger et al. 2005a; Steidel et al. 2010; Crighton et al. 2011). Previous data obtained that are of sufficiently high quality for performing Voigt profile analysis have focused on modest samples of Lyman break galaxies (Turner et al. 2014; Simcoe et al. 2006; Rudie et al. 2012; Crighton et al. 2013, 2015).

It has been found the CGM of Lyman break galaxies exhibit strong enhancement in metal ion absorption out to ≈ 200 kpc relative to the IGM average both in the transverse direction and in the line-of-sight direction to the galaxies. Because Lyman break galaxies inhabit dark

¹ Email: lwymarie@ucolick.org² Department of Astronomy and Astrophysics, UCO/Lick Observatory, University of California, 1156 High Street, Santa Cruz, CA 95064, USA³ Max-Planck-Institut für Astronomie, Königstuhl 17, D-69115 Heidelberg, Germany

matter halos $\lesssim 10^{12} M_{\odot}$ (Adelberger et al. 2005b), the majority of them are not predicted to evolve into the present day, massive, red and dead, elliptical galaxies. To study mechanisms for maintaining or quenching massive galaxy formation, one would preferably perform a similar experiment using background sightlines that pass close to more massive galaxies.

As a primary goal to assess the CGM of the most massive galaxies at $z \sim 2-3$, we have performed the “Quasars Probing Quasars” (QPQ) survey⁴ to inform the processes of massive galaxy formation. Quasars are bright and easily observed at cosmological distances. In an ongoing survey we select closely projected quasar pairs from $\sim 10^6$ quasars from SDSS, BOSS and 2dF surveys (Bovy et al. 2011, 2012). We performed follow-up spectroscopy to confirm the pairs on 4 m class telescope including the 3.5 m telescope at Apache Point Observatory, the Mayall 4 m telescope at Kitt Peak National Observatory, the Multiple Mirror 6.5 m telescope, and the Calar Alto Observatory 3.5 m telescope. Our continuing effort to discover quasar pairs is described in Hennawi et al. (2006b, 2010). Detailed methodology of the QPQ experiment is described in (Prochaska et al. 2013a, hereafter QPQ6). To date, we have confirmed ≈ 700 pairs to within 1 Mpc projected separation. In the series of QPQ papers, statistical inferences have generally been limited to results from low dispersion, stacked spectra, such as covering fractions and equivalent widths (Hennawi & Prochaska 2007; Prochaska et al. 2013b, 2014, hereafter QPQ2, QPQ5 and QPQ7). In the third paper of the QPQ series (Prochaska & Hennawi 2009, hereafter QPQ3), we have reported a detailed analysis of the CGM surrounding one foreground quasar, using echelle resolution, high signal-to-noise ratio spectra. The previous QPQ studies, which suggested that properties of the CGM of QPQ are different from the LBGs, provoked questions about the physics of massive galaxy formation.

The previous QPQ studies have yet to find definitive signatures of quasar feedback in the cool CGM, either. They provoked questions about the nature of quasar feedback. Quasars are the most luminous objects in the Universe and are thought to be powered by infall of matter onto a supermassive black hole at the center of a galaxy. On sub-kpc scales, quasars may ionize and accelerate dense clumps of material, manifested as broad absorption line features (Weymann et al. 1991; Trump et al. 2006). Because of the enormous energy liberated by quasars, quasar feedback is often invoked on larger scales as the energy source that quench star formation in massive galaxies (Kimm et al. 2009; Lu et al. 2012) (but see Gabor et al. 2011).

The degree to which a quasar can influence its host galaxy on kpc scales is less clear. The massive stars in the galaxy and the quasar may produce a significant flux of ionizing photons that would photoionize the surrounding gas on scales of at least tens of kpc. The line-of-sight proximity effect would suppress H I absorption along the line-of-sight to a quasar because of the enhanced photoionization rate in its vicinity, but may yield a greater abundance of highly ionized gas, manifested in e.g. N V and O VI (Tripp et al. 2008; Simcoe et al. 2002; D’Odorico et al. 2008). The same may not hold for the

transverse proximity effect, which is the expected suppression in Lyman- α forest opacity observed in another background sightline transverse to the quasar, caused by the ionizing flux of the foreground quasar (Gonçalves et al. 2008). This will not occur if the quasar emits anisotropically due to obscuration effects in AGN unification models, where the accreting black hole is centered within a torus of dust and gas (Antonucci 1993), or if the quasar emits episodically in short burst durations (Croft 2004; Martini 2004; Hopkins et al. 2005). In Hennawi et al. (2006a, hereafter QPQ1), QPQ2 and Hennawi & Prochaska (2013, hereafter QPQ4), we discussed the transverse proximity effect as it applies to optically thick absorbers in the quasar environment, and argued that most of the optically thick systems observed in background sightlines are likely not illuminated by the quasar. These results are consistent with the results of complementary work done on $z \sim 1$ quasars using low dispersion spectra of projected quasar pairs (Bowen et al. 2006; Farina et al. 2013, 2014; Johnson et al. 2015). They have revealed Mg II absorption in the CGM along the background sightlines coincident with the foreground quasar’s redshift, of strengths consistent with the CGM surrounding non-quasar host galaxies of similar masses.

On the other hand, in the current galaxy formation paradigm, every massive galaxy has undergone a luminous quasar phase, making high redshift quasars the progenitors of dormant supermassive black holes found in the center of nearly all bulge dominated galaxies (Kormendy & Richstone 1995). Moreover, strong clustering of luminous quasars has been measured in various quasar surveys (e.g. Porciani et al. 2004; White et al. 2012). The recent work White et al. (2012) found that at $z \approx 2.4$, when star forming activity peaks, the projected autocorrelation function takes the form $\xi_{QQ} = (r/r_0)^{-1}$, where the correlation length $r_0 = 8.4 h^{-1}$ comoving Mpc implies dark halo masses of $M_{\text{halo}} \approx 10^{12.5} M_{\odot}$. Thus quasar hosts are the progenitors of the present day, massive, red and dead galaxies, whose physical processes that quench their star formation remain poorly constrained.

As we will frequently refer to other results from the Quasars Probing Quasars series, we briefly review the methodology and the results of each paper. In QPQ1 (Hennawi et al. 2006a) we introduced a novel technique of using projected quasar pairs to study the physical state of the gas in $z \sim 2-3$ quasar environments. Spectroscopic observations of the background quasar in each pair reveals the nature of the IGM transverse to the foreground quasar on scales of tens of kpc to several Mpc. We searched 149 background quasar spectra for optically thick absorption in the vicinity of luminous foreground quasars, and found a high covering fraction to strong H I absorbers. In QPQ2 (Hennawi & Prochaska 2007) we compared the statistics of this optically thick absorption in background sightlines near the redshift of the foreground quasars, to that observed along the line of sight to the foreground quasars. We found the clustering pattern of strong H I systems around quasars to be highly anisotropic, and we argued that the foreground quasars anisotropically or intermittently emit their ionizing radiation. In QPQ3 (Prochaska & Hennawi 2009) we presented an echelle spectrum of a projected quasar pair, which resolved the velocity field and revealed the physi-

⁴ <http://www.qpqsurvey.org>

cal properties of the gas at ≈ 100 kpc from the foreground quasar. This gas shows extreme kinematics, an enrichment exceeding 1/10 solar metallicity, and has a temperature $T \approx 10^4$ K. In QPQ4 (Hennawi & Prochaska 2013) we simultaneously studied the quasar CGM in absorption and emission. We found that quasar powered Ly α fluorescence is generally absent from the absorbers observed in background sightlines, which implies the foreground quasars do not illuminate the surrounding gas. In QPQ5 (Prochaska et al. 2013b) we used an enlarged sample of 74 closely projected quasar pair spectra to study the CGM of quasar host galaxies. We reported a covering fraction of $\approx 60\%$ to optically thick, metal enriched gas within the virial radius ≈ 160 kpc. In QPQ6 (Prochaska et al. 2013a), with a sample enlarged to ≈ 650 quasar pairs, we confirmed the high incidence of optically thick gas in excess to IGM average extends to at least 1 physical Mpc transverse to the foreground quasars. The clustering found well exceeds CGM scales, which implies the gas may arise in large scale structures. This enhanced H I absorption measured exceeds that of other galaxy populations, consistent with quasars being hosted by massive dark matter halos. In QPQ7 (Prochaska et al. 2014) we surveyed the incidence and absorption strength of metal line transitions. We found the cool CGM around $z \sim 2$ quasars is the pinnacle amongst galaxies observed at all epochs, regarding covering fraction and equivalent width of H I Ly α and low ions.

To summarize, the QPQ series suggests a massive, enriched and cool CGM surrounding massive galaxies at $z \sim 2$, despite the presence of a luminous quasar whose ionizing flux is sufficient to suppress the local H I Ly α opacity. Until recently, state-of-the-art cosmological (Meiksin et al. 2015; Rahmati et al. 2015) and zoom-in (Fumagalli et al. 2014; Faucher-Giguère et al. 2015) simulations of galaxy formation have had difficulties in reproducing the high covering fractions of optically thick gas seen in the QPQ work, even if one ignores quasar radiation. As explained in Faucher-Giguère et al. (2016), Rahmati et al. (2015) compared QPQ6 results with simulated halos that are typically more massive than the QPQ6 sample. We note the recent work Faucher-Giguère et al. (2016) were able to reproduce high covering fractions of optically thick gas in massive halos, without invoking quasar feedback.

Questions raised by previous QPQ studies can only be answered if we can map the kinematics, ionization structure, relative chemical abundance patterns, the presence or absence of a hot collisionally ionized phase, and the volume density and size of the absorbing clouds, using a statistical sample of high dispersion, high S/N spectra, which is the aim of this eighth paper in the series. This manuscript is summarized as follows. In Section 2, we describe the spectral dataset that comprises QPQ8, including the criteria for selecting the subsample from the QPQ survey, the new observations and data reductions, and precise quasar redshift measurements. In Section 3, we present the metal ion and H I absorption velocity profiles and their column density measurements, as well as modeling of the ionization state of the absorption systems. In Section 4, we constrain the kinematics, the relative chemical abundances, the surface density profiles of the CGM gas, the volume density and the linear size

of the absorbers, and discuss peculiarities of the QPQ8 sample compared to expectations for the $z \sim 2$ cool CGM surrounding quasars. In Section 5, we conclude with our key findings. In the Appendix we describe our treatment of the self blended C IV doublet in our kinematic analysis, and then we present figures and tables for the absorption associated to each of the foreground quasars in the sample. This is a lengthy manuscript. The casual reader may wish to focus their attention on Section 4 which discusses the results and implications. Throughout this manuscript we adopt a Λ CDM cosmology with $\Omega_M = 0.26$, $\Omega_\Lambda = 0.74$, and $H_0 = 70$ km s $^{-1}$ Mpc $^{-1}$. All distances are proper unless otherwise stated.

2. EXPERIMENTAL DESIGN

2.1. The QPQ8 Sample

The primary goal of this paper is to conduct a detailed absorption line analysis of a statistical sample of CGM absorbers at proper impact parameters of 20 kpc to 300 kpc from $z \sim 2$ quasars. The quasar pairs analyzed here are a subset of the sample studied previously for H I Ly α absorption and metal line absorption (C II and C IV) in QPQ6 and QPQ7 respectively. Imposed on this parent sample are selection criteria motivated by our detailed analysis of the quasar pair SDSSJ1204+0221 in QPQ3. We first required that the background quasar was observed with an echellette or echelle instrument, yielding a spectral resolution FWHM ≈ 60 km s $^{-1}$ for echellette and ≈ 8 km s $^{-1}$ for echelle. We further restricted the sample to those pairs where the average S/N at H I Ly α exceeds 9.5 per resolution element. Table 2 provides a summary for the basic specs of different data sets, including spectral resolution, wavelength coverage, and S/N. Spectra of such quality roughly resolve the H I Lyman series and yield metallicity and relative chemical abundance estimates to a precision of 0.3 dex, and would allow for the construction of photoionization models.

Together, these criteria imply a cut on the apparent magnitude of the background quasar of approximately 19.5 mag. We limited the selection to close quasar pairs with projected physical distance $R_\perp < 300$ kpc at the redshift of the foreground quasars to isolate the CGM. We imposed a cut on velocity difference between the redshifts of the two quasars > 3000 km s $^{-1}$, to avoid ambiguity in distinguishing absorption intrinsic to the background quasar from absorption associated with the foreground quasar. Finally, we required that the C II 1334 transition at the foreground quasar’s redshift lie redward of the background quasar’s Ly α forest, i.e. $(1 + z_{\text{fg}})1334.5323 \text{ \AA} > (1 + z_{\text{bg}})1215.6701 \text{ \AA}$. By placing this metal transition outside of the Ly α forest, we ensure access to a suite of rest frame far UV diagnostics free from confusion with intergalactic Ly α absorption. This requirement corresponds to a relative velocity separation $\lesssim 20000\text{--}30000$ km s $^{-1}$. Figure 1 presents the spectra of J0853-0011 as an example of such background-foreground quasar pair.

The final QPQ8 sample comprises 14 pairs. The observation journals, details related to data reduction and calibration of the 1D spectra are provided in QPQ6 and QPQ7. The spectra within the Ly α forest were previously continuum-normalized with an automated principle component analysis algorithm (Lee et al. 2012).

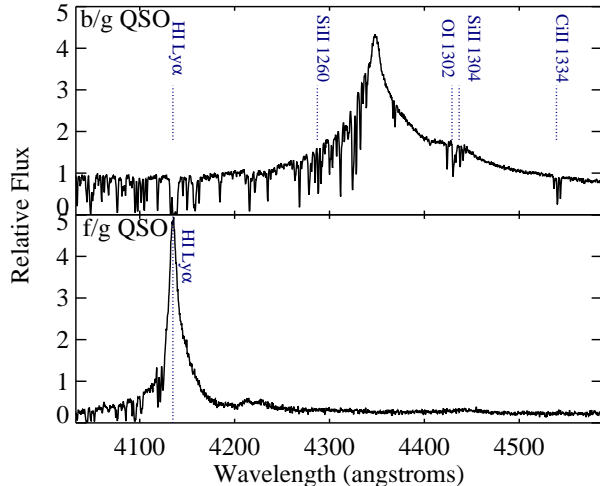


FIG. 1.— We show J0853-0011 as an example of a background-foreground quasar pair. Our line of sight to the background quasar is transverse to the foreground quasar at an impact parameter R_{\perp} , and intercepts its gaseous halo. The ionizing flux of the foreground quasar may or may not have an opening angle $< 4\pi$, and hence it may or may not suppress the cool CGM in the transverse direction. In the background quasar spectrum we see strong Ly α and metal ion absorption coincident with the foreground quasar’s redshift.

To enable the search for weak absorption lines in our higher S/N QPQ8 sample, we here manually refitted the continua. We generated a high order spline function that traces the obvious undulations and emission features of the background quasar. This analysis made use of the routine X.CONTINUUM, distributed as part of the XIDL software package⁵.

Table 1 lists the QPQ8 sample and summarizes key properties of the pairs and spectral data set. In cases where multiple spectra taken by different instruments covered the same transition, we gave preference to the higher resolution spectra provided sufficient S/N. In terms of the spectral and photometric properties of the foreground quasar, the single sightline studied in QPQ3, J1204+0221, is unremarkable. J1204+0221FG has a systemic redshift of $z = 2.4358$, while the median of the QPQ8 sample is $z = 2.4$. J1204+0221FG has a bolometric luminosity of $10^{46.2}$ erg s $^{-1}$. Thus, J1204+0221 is representative of the larger statistical sample, and it is fair for us to rely on QPQ3 to form the selection criteria for QPQ8.

2.2. Quasar Redshifts

The quasar emission redshifts z_{bg} were first taken directly from QPQ6. In QPQ6, the background quasar redshifts were taken from SDSS, while for the foreground quasars a custom line-centering algorithm was adopted to centroid one or more rest frame far UV emission lines Mg II, [C III], Si IV and C IV. We iterated a flux-weighted, line-centering scheme until the centroid converged. Typical uncertainties range from 270 km s $^{-1}$ to 790 km s $^{-1}$. This precision is sufficient to define the QPQ8 sample. To establish a robust association of absorption to the foreground quasar, however, we desire the most precise assessment of its redshift z_{fg} . Ideally, the uncertainties should be less than the peculiar motions of

gas within the massive halos hosting quasars. This requires more precise measurements for z_{fg} than the QPQ6 results.

Our approach is to measure z_{fg} from rest frame optical narrow forbidden emission lines such as [O III] 5007, or the H I Balmer series. For $z \gtrsim 2$ quasars, these lines are shifted into the near infrared. These lines have smaller systematic uncertainties of 400 km s $^{-1}$ or lower. [O III] has an average blueshift of 27 km s $^{-1}$ and a dispersion of 44 km s $^{-1}$ about this value (Boroson 2005; Richards et al. 2002). To account for this average shift due to the blue wing of the [O III] line, we added 27 km s $^{-1}$ to the vacuum rest wavelength of 5008.24 Å when computing the redshift of the line. We have quantified the H α and H β precision for an independent SDSS dataset to be 300 km s $^{-1}$ and 392 km s $^{-1}$ respectively about the systemic. We note that, in order to cover H α in the optical, these SDSS quasars need to be at low redshift and hence are often not as luminous as the quasars in our QPQ sample. For fainter quasars, H α is more peaked because of the narrow line region, and hence the redshifts will be more accurate than for a luminous sample. We are not using these redshift uncertainties in a very quantitative manner, however. We observed 13 of the 14 foreground quasars using GNIRS (Elias et al. 2006) and NIRI (Hodapp et al. 2003) on the Gemini North telescope, NIRSPEC (McLean et al. 1998) on the Keck II telescope, and/or X-SHOOTER (Vernet et al. 2011) on the Very Large Telescope. Table 3 provides a journal of the near IR observations. When Mg II 2800 is detected, the Mg II emission redshift is preferred over the H α or H β emission redshifts for its smaller uncertainty of 272 km s $^{-1}$. We have taken into account the median redshift of 97 km s $^{-1}$ of Mg II from O III (Richards et al. 2002).

The XSHOOTER spectra were reduced with a custom software package developed and kindly provided by George Becker, which includes nod sky subtraction on the slit and telluric corrections based on the European Southern Observatory SkyCalc sky model calculator (Noll et al. 2012; Jones et al. 2013; Moehler et al. 2014). Flat fielding of the detector was performed using dome flat exposures, and wavelength calibration of the near IR arm used night sky emission features. Sky subtraction implements a two dimensional b-spline algorithm and extraction was performed optimally. Significant residuals do persist at lines of the brightest sky emission. The remaining data was processed with algorithms in the LowRedux⁶ package developed primarily by one of us, JFH. The processes are similar to those for XSHOOTER. The principal difference is sky subtraction where the LowRedux algorithms first perform image subtraction of dithered (AB) exposures before fitting a b-spline to sky residuals. For all spectra, fluxing was performed with a telluric standard observed close in time and position on the sky to the scientific target.

In the following analysis, we omit the near IR observations for (1) J1145+0322FG, whose H β 4862 and [O III] 5007 lines fall outside the transmitting infrared atmospheric windows. The emission line analyzed for redshift was Mg II, as described in QPQ6; (2) J 0225+0048FG, whose H β 4862, [O III] 5007 and H α are

⁵ <http://www.icolick.org/~xavier/xidl>

⁶ <http://www.icolick.org/~xavier/LowRedux/index.html>

TABLE 1
QPQ8 SAMPLE SUMMARY

Name	f/g Quasar	z_{fg}	$\log L_{912}^a$	$\log L_{\text{bol}}^b$	g_{UV}^c	b/g Quasar	z_{bg}	R_{\perp} (kpc)	θ^d
J0225+0048	J022517.68+004821.9	2.7265	30.33	46.34	535	J022519.50+004823.7	2.820	226	27.4
J0341+0000	J034138.15+000002.9	2.1233	29.92	46.07	274	J034139.19-000012.7	2.243	190	22.1
J0409-0411	J040955.87-041126.9	1.7155	30.34	46.42	516	J040954.21-041137.1	2.000	235	26.9
J0853-0011	J085358.36-001108.0	2.4014	29.82	45.86	645	J085357.49-001106.1	2.577	112	13.2
J0932+0925	J093226.34+092526.1	2.4170	30.27	46.31	402	J093225.60+092500.2	2.602	238	28.1
J1026+4614	J102618.80+461445.2	3.3401	30.79	46.79	1119	J102616.11+461420.8	3.421	288	37.1
J1038+5027	J103857.37+502707.9	3.1322	30.90	46.90	2069	J103900.01+502652.8	3.237	233	29.4
J1144+0959	J114435.53+095921.6	2.9731	30.63	46.55	1639	J114436.65+095904.9	3.160	189	23.5
J1145+0322	J114546.54+032236.7	1.7652	29.93	46.05	559	J114546.21+032251.9	2.011	139	15.9
J1204+0221	J120417.46+022104.7	2.4358	30.17	46.19	1424	J120416.68+022110.9	2.532	112	13.2
J1420+1603	J142054.42+160333.3	2.0197	30.58	46.54	4298	J142054.92+160342.9	2.057	104	12.0
J1427-0121	J142758.88-012130.3	2.2736	30.63	46.63	17964	J142758.73-012136.1	2.354	53	6.2
J1553+1921	J155325.60+192140.9	2.0098	29.70	45.81	3056	J155325.88+192137.6	2.098	44	5.1
J1627+4605	J162738.63+460538.3	3.8137	30.66	46.69	1222	J162737.24+460609.3	4.110	253	34.1

^a The specific luminosity of the foreground quasar at the Lyman limit 912 Å, in unit of $\log \text{erg s}^{-1} \text{Hz}^{-1}$

^b The bolometric luminosity of the foreground quasar, in unit of $\log \text{erg s}^{-1} \text{Hz}^{-1}$.

^c The enhancement in flux relative to the extragalactic UV background, assuming the foreground quasar emits isotropically and a distance equal to the impact parameter R_{\perp} .

^d Angular separation between foreground and background quasar, in arcseconds.

TABLE 2
QPQ8 DATA SET SPECS

Name	b/g Quasar Instrument	Resolution in FWHM (km s^{-1})	Wavelength Coverage (Å)	S/N per Å at Lyα at z_{fg}
J0225+0048	ESI, GMOS	60, 125	3993-10556	76
0341+0000	MagE	50	3044-10254	33
0409-0411	MagE	62	3044-9459	15
0853-0011	MagE	62	3042-10285	121
0932+0925	MagE	51	3041-10284	74
J1026+4614	ESI	49	3994-10197	184
J1038+5027	ESI	48	3994-10197	70
1144+0959	MIKE	9	3307-9167	205
1145+0322	MagE	51	3042-10285	18
1204+0221	HIRES	8	3448-6422	162
J1420+1603	MagE	51	3042-10285	74
J1427-0121	MIKE, MagE	8, 50	3309-9169	157
1553+1921	MagE	51	3042-10285	33
J1627+4605	ESI	45	3989-10198	98

TABLE 3
JOURNAL OF NEAR INFRARED OBSERVATIONS

Quasar	Observatory	Instrument	Date in UT	Exposure Time (s)	Line	z_{em}	$\sigma(z_{\text{em}})$ (km s^{-1})
J0341+0000FG	Keck	MOSFIRE	2014 Oct 1	960	Hβ	2.1233	272 ^a
J0409-0411FG	Keck	MOSFIRE	2014 Oct 1	960	Hα	1.7155	272 ^a
J0853-0011FG	Keck	NIRSPEC	2010 Jan 29	4800	[OIII]	2.4014	44
J0932+0925FG	VLT	XSHOOTER	2011 Apr 4	3600	[OIII]	2.4170	44
J1038+5027FG	Gemini	NIRI	2006 May 9	4800	[OIII]	3.1323	44
J1144+0959FG	Keck	NIRSPEC	2009 Jan 7	3000	[OIII]	2.9731	44
J1204+0221FG	Gemini	GNIRS	2006 Mar 27	5440	[OIII]	2.4358	44
J1420+1603FG	VLT	XSHOOTER	2011 Apr 28	2400	Hα	2.0197	272 ^a
J1427-0121FG	Gemini	GNIRS	2006 Mar 12	7200	[OIII]	2.2736	44
J1553+1921FG	VLT	XSHOOTER	2007 Jul 17	2400	[OIII]	2.0098	44
J1627+4605FG	Gemini	NIRI	2007 May 29	14400	[OIII]	3.8137	44

^a We quantified the uncertainties for Hα emission redshift and Hβ emission redshift to be 300 km s^{-1} and 392 km s^{-1} respectively. Hence when Mg II is detected, we adopted the Mg II emission redshift instead of the near IR redshift, for its smaller uncertainty of 272 km s^{-1} .

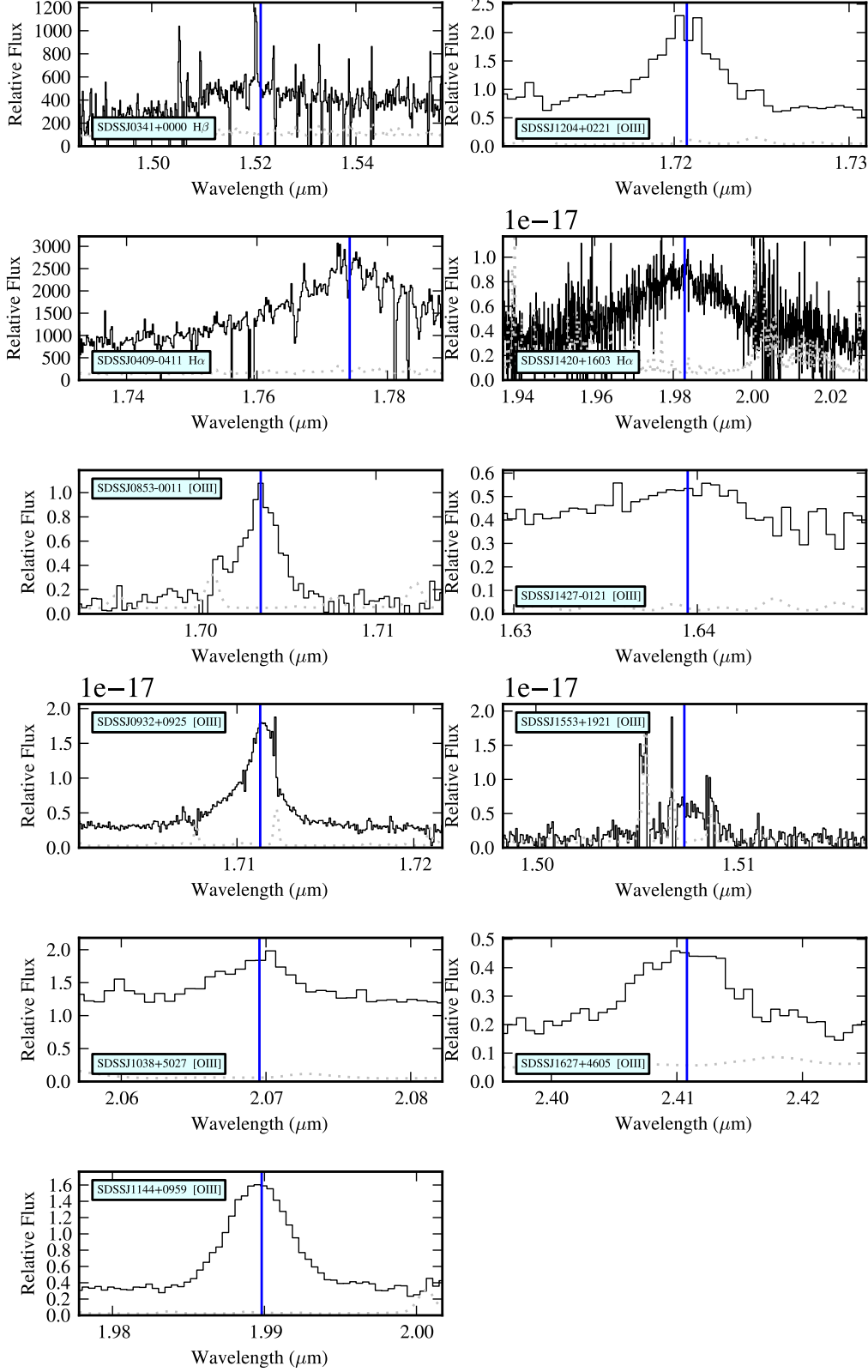


FIG. 2.— Near IR spectra of the foreground quasars for precisely determining the systemic redshift. The gray dotted curve is the 1σ uncertainty. We applied our custom centroiding algorithm on the $[\text{O III}] \lambda 5007$ emission line whenever it is present. When $[\text{O III}]$ is not detectable we used $\text{H}\alpha$ or $\text{H}\beta$. If no near IR data exists for the foreground quasar or no emission lines are found, we adopted the QPQ6 systemic redshift which is obtained by fitting the full optical spectra.

all redshifted to wavelengths of low atmospheric transmission. The emission lines analyzed for redshift were Si IV, C IV and [C III]. Although it has Mg II at observable wavelengths, it falls outside of our spectral coverage; (3) J1026+4614FG, whose H β 4862 and [O III] 5007 emission lines are weak and yield redshift estimates that are inconsistent. The emission lines analyzed for redshift were Si IV and [C III]. The quasar too has Mg II at observable wavelengths but outside of coverage. For these sources, we adopted the z_{fg} measurements from QPQ6. Figure 2 presents the near IR spectra of the 11 foreground quasars with a near IR redshift measurement. We have analyzed these data with a custom algorithm that centroids the emission lines and generates a best estimate for z_{fg} . The results and adopted uncertainties are listed in Table 3.

3. ANALYSIS

In this section, we present column density measurements for the gas associated to the foreground quasars in the QPQ8 sample. We begin with an analysis of associated metal line absorption, proceed to the H I analysis, and then describe ionization modeling of the systems. Details for the individual systems are provided in the Appendix. Here we describe the methodology and present representative examples.

3.1. Metals Absorption in Multiple Ionization States

We performed a search for associated metal line absorption within 1000 km s $^{-1}$ of z_{fg} . This search window allows for large peculiar motions in the gas which may be common in the environments of these massive galaxies (e.g. QPQ3, Johnson et al. 2015). At the median $z_{\text{fg}} = 2.4$ of our sample, this line-of-sight velocity window corresponds to 8 Mpc physical. We emphasize that strong metal lines systems of equivalent width $> 0.3 \text{ \AA}$ are rare in the intervening IGM along quasar sightlines and are dominated by C IV absorption. According to the calculations in QPQ7, the random incidence of C IV absorbers with equivalent width $> 0.3 \text{ \AA}$ is 2.1 per unit redshift. QPQ6 measured a drop in H I equivalent width and QPQ7 measured a drop in C II and C IV equivalent width with impact parameter, especially at $> 200 \text{ kpc}$. They suggest the cool CGM gas is mostly contained in proximity to central galaxy and argues against a large contribution from Mpc scales. The positive detection of any such metals within 1000 km s $^{-1}$ of z_{fg} is therefore unlikely to arise from gas at cosmological separations (see QPQ7 for further details). In Johnson et al. (2015), it was suggested that the CGM of neighboring galaxies of other host halos could contribute a significant portion of the Mg II absorption they observed around quasars. However, they plotted covering fractions due to all absorbers that fall within $\pm 1500 \text{ km s}^{-1}$, which include contributions from galaxies that are actually within 300 kpc and hence are in the same host halo.

An absorption line system bearing heavy elements was detected in 12 out of 14 cases, an incidence that greatly exceeds random expectation. Furthermore, 8 of these systems exhibit low ion transitions (e.g. C II 1334) which occurs even more rarely in random sightlines. For complex profiles, metal ion absorption well separated into distinct velocity intervals are grouped into subsystems A,

B, C, etc, and are separately analyzed in what follows. Figure 3 shows the velocity profiles for the absorption associated to J0853-0011. The gas spans approximately 650 km s $^{-1}$, which we divided into three subsystems. Although multiple ionization states, e.g. C $^{+}$ and C $^{3+}$, tend to have optical depth ratios that vary across velocity, they roughly trace one another in velocity structure.

For each subsystem associated to each foreground quasar, we measured the ionic column densities from commonly detected metal line transitions in CGM gas (e.g. Werk et al. 2013). For these measurements, we used the apparent optical depth method (AODM; Savage & Sembach 1991) which yields precise values for high spectral resolution observations. For non-detections, we report 3σ upper limits on column densities, obtained by integrating over a velocity window that encompasses most of the apparent optical depths of a subsystem.

Line saturation, however, may affect the echellette spectra ($R_{\text{FWHM}} \approx 6,000$) and we conservatively report lower limits for cases where the minimum normalized flux is below ≈ 0.4 . Metal absorption components are typically narrow $< 10 \text{ km s}^{-1}$, which is evident in the three echelle spectra included in this study. In the Appendix we show that, where the minimum normalized flux is greater than 0.4, echellette quality spectra are sufficient for accurate column density measurements. Hence with our criterion on the normalized flux, using echellette quality spectra does not introduce systematic biases.

We verified that the velocity intervals of the subsystems are chosen in a way that there is little apparent variation in the ionic ratios. The scientific results that involve assessing ionization do not sensitively depend on how many subsystems have been chosen, and we quote weighted average values of ionization parameter, chemical abundances, etc for each quasar-pair absorption system in what follows. For one absorption system, J1427-0121, for which an echelle spectrum was obtained, we fitted Voigt profiles to the unsaturated metal absorption components as discussed in the Appendix. As expected for resolved lines, the total ion column densities recovered for each subsystem agree with measurements from integration the apparent optical depths. In cases where there is no substantial ionization structure (as required for our subsystems), breaking down the absorption profile into individual components has limited scientific value. Uncertainties associated with ionization modeling and line saturation exceed the benefit gained from component-by-component fitting. Hence this study does not include a component-by-component analysis.

A brief description of each system, figures for the velocity plots, and tables of all line measurements are presented in the Appendix. Table 4 summarizes the integrated measurements for the QPQ8 sample.

3.2. Lyman Series Voigt Profile Modeling

For each system we measured the H I column density of the gas by modeling its Lyman series absorption. We have echellette or echelle resolution coverage of Ly α for every system. We also included higher order Lyman series lines where the S/N estimated from the quasar continuum exceeds 5 per pixel. When the echellette or echelle data do not cover blue enough cover for these transitions, we also used lower dispersion data when available. For many of the systems the Lyman se-

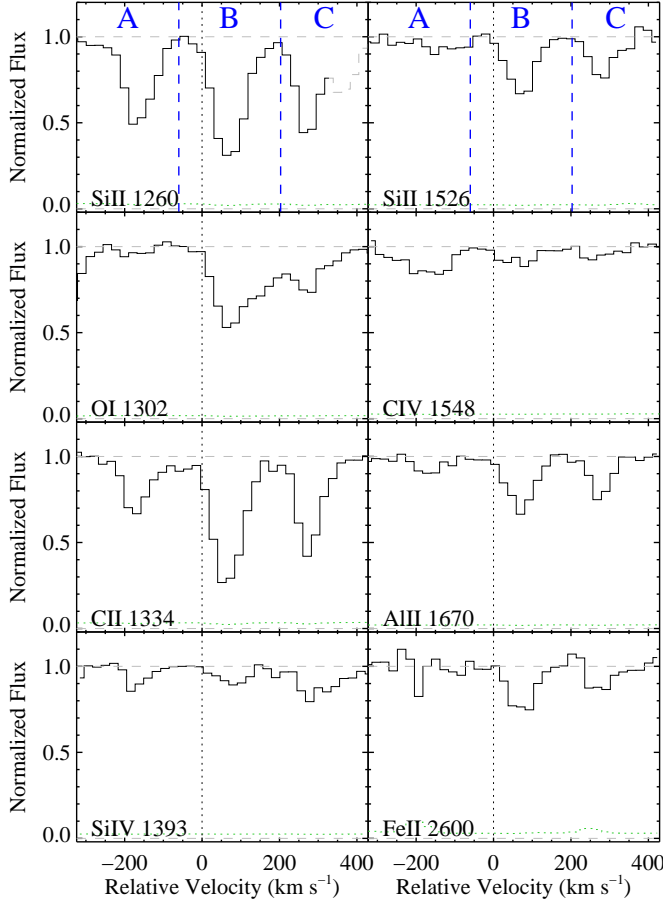


FIG. 3.— A subset of metal line transitions from the absorption associated to J0853-0011FG. The velocities are relative to the measured $z_{\text{fg}} = 2.4014$. Absorption well separated in distinct velocity intervals are designated as subsystems A, B and C as denoted by the vertical dashed lines in the top subpanels. Absorption that is presumed unrelated to the foreground quasar, e.g. $\text{Ly}\alpha$ features from unrelated redshifts, are presented as dashed, gray lines. The gas shows multiple ionization states that roughly trace each other and span $\approx 650 \text{ km s}^{-1}$. The green histogram shows the 1σ noise in the normalized flux.

ries lines are all saturated yet do not exhibit damping wings, i.e. the lines fall on the saturated portion of the curve of growth. A precise measurement of N_{HI} is therefore difficult and is degenerate with assumptions made about the component structure and Doppler b -values one adopts in the modeling. Our general approach is to first set conservative bounds on N_{HI} based on a wide range of allowed Doppler parameters from $b = 15 \text{ km s}^{-1}$ to $b = 60 \text{ km s}^{-1}$. Such estimates are dependent, however, on the number of assumed components and their relative velocities.

We then performed Voigt profile modeling of the data by χ^2 minimization using the Absorption Line Software (ALIS; Cooke et al. 2014). ALIS uses the MPFIT package (Markwardt 2009) which employs a Levenberg–Marquardt least squares minimization algorithm, where the difference between the data and the model is weighted by the error in the data. We reduced the degrees of freedom by fixing the relative velocities of unblended H I components or H I components associated with metal absorption, preferably low ions, that

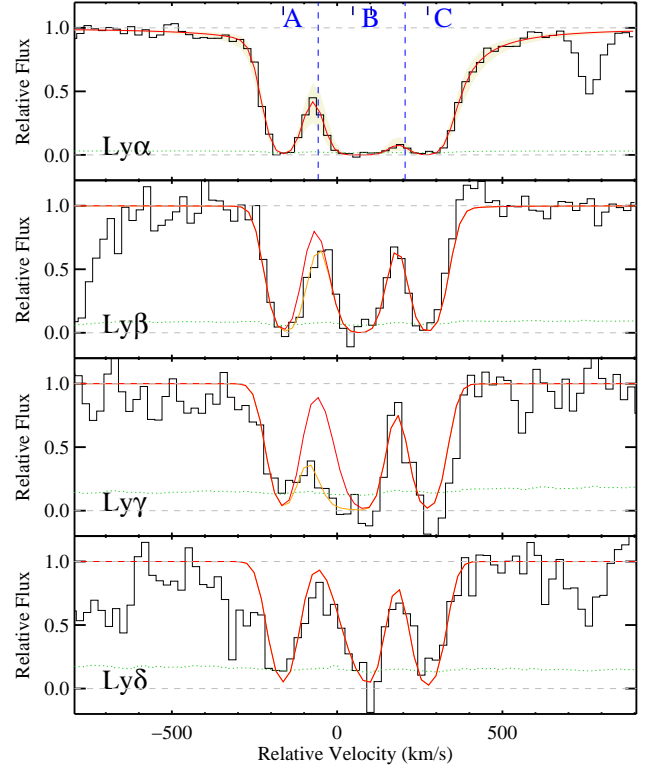


FIG. 4.— Example fit to H I Lyman series absorption profiles for J0853-0011. The black histograms show the Lyman series identified in the J0853-0011BG spectrum at velocities consistent with J0853-0011FG. The green dotted curves show the 1σ noise in the normalized flux. The relative velocity at 0 km s^{-1} corresponds to the redshift of J0853-0011FG. We performed χ^2 minimization Voigt profile modeling to assess the H I column density. Specifically we introduced H I components centered at relative velocities traced by the peak optical depths of the associated set of metal ions. Note in subsystem B there are two components. The navy ticks in the top subpanel mark the centroid redshifts for components traced by low ions. Figures of fits to Lyman series absorption for other QPQ8 systems, presented in the Appendix, will also show ticks that mark the centroids for components traced by high ions and ticks that mark H I components not associated with metal ions. Additional H I components introduced to model $\text{Ly}\alpha$ forest blending are omitted in the tickmarks. The red curve is the summation of all H I components associated with J0853-0011FG, and the beige shades mark the estimated $\pm 1\sigma$ errors in H I column densities. The orange curve is the summation of all H I components associated with J0853-0011FG and $\text{Ly}\alpha$ forest contamination.

show well matching velocity structures. The Doppler b parameter is allowed to vary freely between the values of 15 km s^{-1} to 60 km s^{-1} , which are typical of the high- z $\text{Ly}\alpha$ forest (Kirkman & Tytler 1997). We adopted approximately the central N_{HI} values in the range of solutions allowed by ALIS that have nearly equivalent χ^2 . Since possible damping wings of a Voigt profile may as well be explained by a weak component that is not introduced to the model, ALIS best-fit solutions tend to give biased high values. For this reason, our adopted N_{HI} and the ALIS best-fit N_{HI} values need not agree.

As an example, Figure 4 shows the Lyman series data and our fit for the J0853-0011 absorption system. For each subsystem we identified H I components at the velocities corresponding to the peak optical depths of its associated set of metal lines. The velocity centroids of H I components traced by low ions, e.g. C II and O I,

are marked by navy ticks. In figures of Lyman series fits for other QPQ8 systems, presented in the Appendix, we also mark the centroids of H I components traced by high ions, primarily C IV, and centroids of H I components that have no associated metal ions. The red curve is the summation of all H I components associated with the foreground quasar, while the orange curve is the summation of all H I components associated with the foreground quasar and additional H I components introduced to model Ly α forest contamination.

From trial-and-error of introducing additional components in the modeling, we found the possible presence of unresolved components introduces a systematic error of several tenths dex in the N_{HI} values. We also performed the same Lyman series modeling using a MagE spectrum of J1427-0121 and compared to the modeling results using the MIKE spectrum. We found that the best-fit N_{HI} values can be recovered within 1σ error, and hence echellette resolution spectra does not introduce significantly larger errors compared to echelle spectra. Moreover we estimated a systematic error of ± 0.2 dex in the N_{HI} values due to quasar continuum placement. For H I components that we did not fix the velocities, due to line blending ALIS reported unphysically large uncertainties in N_{HI} values when the uncertainties in the relative velocities of the components are large. The Voigt model parameters as well as the total N_{HI} of each absorption system and subsystems are tabulated in Table 21 in the Appendix. A detailed description of the model for each quasar pair is also presented in the Appendix.

3.3. Ionization Modeling: the Ionization Parameter U

As summarized in the previous subsections and presented in Figures 3 and 4, the CGM of galaxies hosting quasars exhibit multiple ionization states (e.g. O 0 , Si $^+$, S $^{2+}$, Si $^{3+}$), and the total H I column densities are generally less than 10^{19} cm^{-2} . Both of these observations imply a predominantly ionized gas. Even if the quasar's ionizing flux is not directly impinging on the gas (as we have previously argued in the QPQ series), the extragalactic ultraviolet background (EUVB) may photoionize the medium, resulting in neutral fractions $x_{\text{HI}} \ll 1$ (e.g. QPQ3). Therefore, we generated photoionization models for each of the systems exhibiting metal line absorption, to estimate x_{HI} and other physical properties of the gas. In the process, if we can make assumptions about the gas volume density or estimate it through fine structure excitation lines, we may compare the intensity of the ionizing radiation field that produces the observed ionic ratios with the predicted flux of the quasar at the impact parameter of the sightline. This way we may test the hypothesis of whether the nearby foreground quasars are shining on the gas.

There are two primary processes that produce an ionized gas: collisional ionization and photoionization. If we assume the cooling function takes the form in Sutherland & Dopita (1993), the cooling time $t_{\text{cool}} \lesssim 10^4$ yr is short for any reasonable density. A model where collisional ionization is the primary mechanism producing the observed ionic ratios would require a heat source to maintain the gas temperature in equilibrium. We therefore assumed photoionization is the dominant mechanism for setting the ionization structure of the gas, and also

the dominant source of heat. Furthermore we note that the analysis in QPQ3 shows collisional ionization equilibrium solutions with $T \sim 10^4$ K give very similar results to the photoionization models presented here.

We calculated the ionization state of plane parallel slabs with version 10.00 of the Cloudy software package last described by Ferland et al. (2013). The inputs to Cloudy are the N_{HI} of a subsystem, as modeled in the previous subsection, the total volume density (neutral plus ionized) n_{H} which we fix at a constant 0.1 cm^{-3} , and an initial assumed metallicity $[\text{M}/\text{H}] = -0.5$ dex. We then varied the ionization parameter $U \equiv \Phi/n_{\text{H}}c$ where Φ is the flux of ionizing photons having $h\nu \geq 1$ Ryd, and iterated on $[\text{M}/\text{H}]$ and U until the results converge. The results are largely insensitive to the choice of volume density as it is nearly homologous with U , but they do vary with metallicity because this affects the cooling rate of the gas. It is convenient to fix n_{H} and vary Φ , so that there is only one degree of freedom in the output which is the ionization parameter. For these calculations, we assumed the spectral shape of the extragalactic UV background field follows that computed by Haardt & Madau (2012) and varied the amplitude. For radiation fields of $z \sim 2$ quasars at a few Ryd, the EUVB is very similar to a power law spectrum $f_{\nu} \propto \nu^{-1.57}$. As the input U parameter changes, the Cloudy algorithm varies the number of gas slabs to maintain a constant N_{HI} at the input value. For optically thick systems the results are sensitive to the assumed N_{HI} . Larger N_{HI} values imply more self shielding of the inner regions which in turn demand a more intense radiation field to explain the observed ionization states.

For each system, we considered a series of ionic ratios and a wide range of ionization parameters. Our analysis focused on multiple ionization states of individual elements such as C $^+$ /C $^{3+}$ and Si $^+$ /Si $^{3+}$, to avoid uncertainties related to intrinsic abundance variations. We also considered ratios of low to high ion species of different elements for constraining U assuming solar relative abundances. We adopted a correspondingly higher uncertainty for such constraints.

Figure 5 presents the comparison of a series of Cloudy models with constraints from the ionic ratios of the three subsystems in J0853-0011. The observational constraints on the ionic ratios and the corresponding log U values are indicated by solid boxes, or arrows for lower or upper limits. The ionic ratios for these three subsystems can be described by a photoionization model with $\log U \approx -3.3$. Occasionally, the observational constraints are not fully consistent with a single U value, for example subsystem C of J0853-0011 shown in Figure 5. Although this inconsistency may suggest the low and high ions arise in a multiphase or non-equilibrium medium, there are significant systematic uncertainties inherent to photoionization modeling including the assumed spectral shape for the radiation field, cloud geometry and the atomic data. In such cases, we preferred constraints from ionic ratios that are more sensitive to U . For example, for subsystems of J0853-0011, observational constraints from C $^+$ /C $^{3+}$ and Si $^+$ /Si $^{3+}$ are preferred to Fe $^+$ /Fe $^{2+}$, and we adopted a U value that is between that constrained by C $^+$ /C $^{3+}$ and that by Si $^+$ /Si $^{3+}$. We then proceeded conservatively by allowing for a substantial error on U . The uncertainties

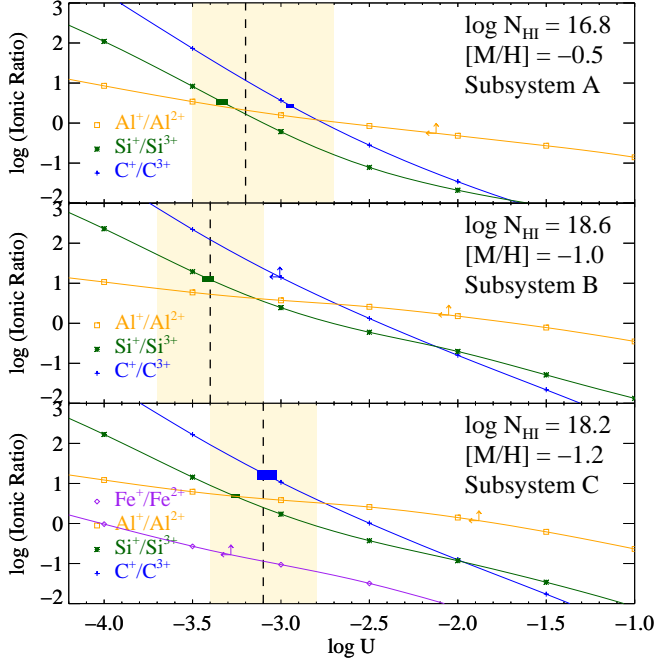


FIG. 5.— Cloudy example of constraining the ionization parameter $U = \Phi/n_{\text{H}}c$ for J0853-0011, where Φ is the ionizing photon flux. This figure presents a comparison of a series of Cloudy models with constraints from the ionic ratios of the three subsystems A, B, and C. The observed ionic ratios and the corresponding $\log U$ are indicated by solid boxes, whose heights and breaths represent the $1\text{-}\sigma$ uncertainties, or indicated by arrows for lower or upper limits.

in the adopted $\log U$ values in this study are set to be at least 0.3 dex. For J0853-0011, the adopted uncertainties in $\log U$ encompass constraints on U from all ionic ratios. The estimated U value will give a corresponding neutral fraction x_{HI} and a total hydrogen column density $N_{\text{H}} \equiv N_{\text{HI}}/x_{\text{HI}}$. The error in the neutral fraction is roughly linear with the uncertainty in U for $\log U > -4$.

A discussion of the constraints and ionization modeling results for the individual absorption systems is presented in the Appendix. Figure 6 presents a scatter plot for all of the U values derived from the dataset against the estimated H I column density. Despite the large uncertainties in the measurements, there is a statistically significant anti-correlation between U and N_{HI} . A Spearman's rank correlation test rules out the null hypothesis at 99.99% confidence. This may be explained by either an increasing volume density n_{H} with increasing column density N_{HI} or a fixed volume density and a varying radiation field. In the latter case, when Φ decreases, U decreases and N_{HI} increases. This would be the scenario if there is gas with similar density at different distances or if there are illuminated and obscured systems.

Granted the focus of this manuscript is on the cool CGM, we estimated a characteristic U value for each pair by weighting the U values of each subsystem by its corresponding N_{HI} value:

$$\langle U \rangle \equiv \frac{\sum(U N_{\text{HI}})}{\sum(N_{\text{HI}})} \quad (1)$$

These values are listed in Table 5 together with the N_{HI} -weighted neutral fractions $\langle x_{\text{HI}} \rangle$, and the individual constraints on U for each subsystem. We also derived

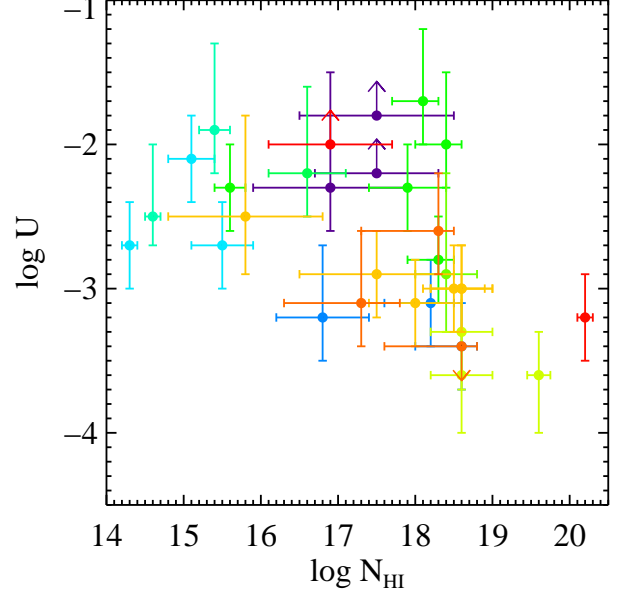


FIG. 6.— A scatter plot for all of the individual subsystems' U values against the estimated N_{HI} . For clarity, subsystems associated with different quasars are coded in different colors. An anti-correlation is significant at $> 99.99\%$ confidence.

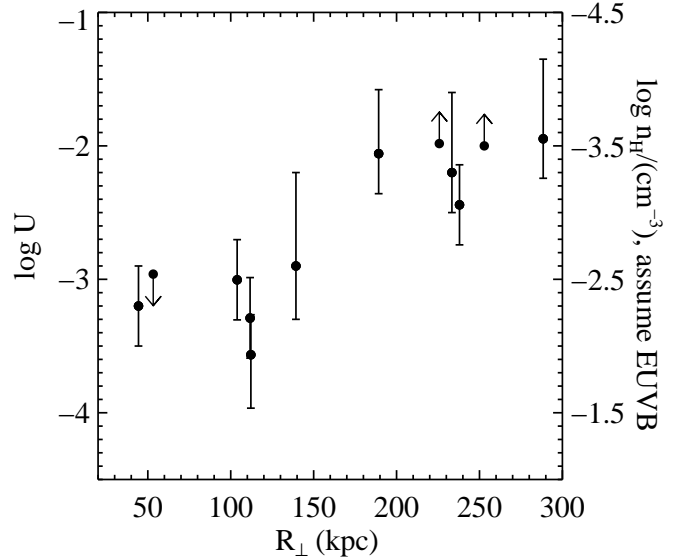


FIG. 7.— $\langle U \rangle$ as a function of R_{\perp} . We estimated a characteristic average $\langle U \rangle$ for each quasar associated absorption system by weighting the U values of the subsystems by their N_{HI} . The correlation between $\langle U \rangle$ and R_{\perp} is significant at 99.8% confidence. We also derived n_{EUVB} , the density required to give $\langle U \rangle$ if the gas is only illuminated by the extragalactic UV background and rescaled to match the mean opacity of the Ly α forest. These may be regarded as lower limits to the gas density.

n_{EUVB} , the density one will require to give the $\langle U \rangle$ value if the gas is only illuminated by a EUVB with normalization rescaled to match the Faucher-Giguère et al. (2008) mean opacity of the Ly α forest. We list the n_{EUVB} results in Table 5. In this scenario, one would require gas densities of 10^{-2} cm^{-3} or lower. These may be regarded as lower limits to the gas density. The results of n_{EUVB} together with $\langle U \rangle$ as a function of the impact parameter R_{\perp} are plotted in Figure 7. There is a statisti-

TABLE 4
TOTAL IONIC COLUMN DENSITIES

QSO Pair	z_{fg}	$\log N(\text{C}^+)$	$\log N(\text{C}^{+3})$	$\log N(\text{O}^0)$	$\log N(\text{Si}^+)$	$\log N(\text{Si}^{+3})$	$\log N(\text{Fe}^+)$
J0225+0048	2.7265	< 13.86	14.12 ± 0.02		< 12.76	13.39 ± 0.05	
J0341+0000	2.1233	< 14.00	< 13.28		< 13.42		< 13.62
J0409-0411	1.7155	< 13.97	< 13.31		< 13.48		14.12 ± 0.08
J0853-0011	2.4014	> 14.11	13.25 ± 0.03	14.48 ± 0.01	13.36 ± 0.01	12.86 ± 0.03	13.01 ± 0.03
J0932+0925	2.4170	13.72 ± 0.11	13.93 ± 0.02		< 13.55	13.14 ± 0.04	< 13.19
J1026+4614	3.3401	< 13.14	13.43 ± 0.02		< 12.12	12.74 ± 0.04	
J1038+5027	3.1323	< 13.38	14.08 ± 0.02		< 13.39	13.00 ± 0.10	
J1144+0959	2.9731	> 13.26	> 13.84	13.16 ± 0.13	12.84 ± 0.03	> 13.06	13.25 ± 0.05
J1145+0322	1.7652	> 14.71	> 14.59	14.08 ± 0.14	13.97 ± 0.05	13.74 ± 0.03	13.53 ± 0.09
J1204+0221	2.4358	> 14.75	13.80 ± 0.01	> 14.46	> 14.27	13.06 ± 0.01	13.59 ± 0.04
J1420+1603	2.0197	> 14.22	> 14.12	> 14.61	13.25 ± 0.03	13.27 ± 0.03	13.59 ± 0.01
J1427-0121	2.2736	14.01 ± 0.02	14.40 ± 0.02	14.12 ± 0.03	12.75 ± 0.01	12.91 ± 0.03	< 12.58
J1553+1921	2.0098	> 14.92	14.57 ± 0.03	> 15.05	15.26 ± 0.14	13.82 ± 0.10	14.02 ± 0.03
J1627+4605	3.8137	< 13.17	13.63 ± 0.04	< 13.53	< 13.25	< 12.66	

NOTE. — Total logarithmic column densities for the absorption associated to each QPQ8 pair. One should adopt a systematic uncertainty of 0.05 dex related to continuum placement.

cally significant positive correlation between $\langle U \rangle$ and R_{\perp} . A Spearman's rank correlation test rules out the null hypothesis at 99.8% confidence. This positive dependence of $\langle U \rangle$ on R_{\perp} runs contrary to expectation should the quasar dominate the ionizing flux received by the absorbers, unless the density profile is much steeper than that of n_{EUVB} . Moreover, we found no statistically significant correlation between U and quasar bolometric luminosity or the UV enhancement factor, again contrary to expectation if the quasar radiation dominates. The dependence of $\langle U \rangle$ on R_{\perp} further implies that n_{H} decreases with increasing R_{\perp} . This may also be explained as an increasing volume density with increasing neutral column density. Table 5 also lists n_{QSO} , the density required to yield $\langle U \rangle$ assuming the gas is located at a distance from the quasar equal to R_{\perp} and that the quasar emits isotropically. We note that in QPQ2 we argued that the anisotropic clustering (i.e. transverse compared to line-of-sight) of optically thick absorbers around quasars suggests that most $N_{\text{HI}} \gtrsim 10^{17} \text{ cm}^{-2}$ absorbers detected in background sightlines are not illuminated by the foreground quasar, and we came to similar conclusions based on the absence of fluorescent recombination emission from these absorbers in QPQ4. The n_{QSO} values may be regarded as a rough upper bound to n_{H} , unless there is an extra local source of radiation, where the n_{H} values would need to be correspondingly higher as the U values are elevated. We discuss these values further in Section 4.4.

4. RESULTS

4.1. Kinematics

Combining the high spectral resolution of the QPQ8 dataset with our near IR estimates for z_{fg} , we may precisely characterize the kinematics of the absorbing gas. Such measurements resolve the dynamics of the cool gas in the massive halos hosting quasars and constrain physical scenarios for the origin of this medium. In particular, one may search for evidence of non-gravitational motions, i.e. galactic scale outflows powered by AGN, that are regularly invoked as a critical process in galaxy formation theory (e.g. Faucher-Giguère & Quataert 2012).

In the following, we examine three statistical measures to characterize the kinematics: (i) the optical depth

weighted velocity offset of the gas relative to z_{fg} :

$$\bar{\delta v} \equiv \frac{\sum_i \tau_i \delta v_i}{\sum_i \tau_i} \quad (2)$$

where f_i the normalized flux and $\tau_i = -\ln(f_i)$ is the optical depth per pixel. In cases where the absorption saturates, we adopt a value equal to one-half of the standard deviation in those pixels $\sigma(f_i)/2$. This tends to limit τ_i to less than 4 per pixel; (ii) the velocity interval that encompasses 90% of the total optical depth Δv_{90} (e.g. Prochaska & Wolfe 1997); (iii) the root-mean-square of the gas σ_v , measured from the optical depth weighted dispersion of the profiles. Figure 8 provides a qualitative picture of the kinematic characteristics. Plotted are the C IV doublets for the QPQ8 sightlines with $v = 0 \text{ km s}^{-1}$ corresponding to z_{fg} for the C IV 1548 transition. In each, we highlight the Δv_{90} interval relative to z_{fg} . For the few absorption systems where Δv_{90} exceeds the velocity separation of the $\lambda\lambda 1548, 1550$ doublet $\approx 500 \text{ km s}^{-1}$, we estimated the kinematic measurements for C IV 1548 as described in the Appendix. A few results are evident. First, the gas exhibits a dynamic range in the Δv_{90} widths ranging from $\approx 50 \text{ km s}^{-1}$ to nearly 1500 km s^{-1} . Second, the centroids of the absorption profiles tend to occur within 500 km s^{-1} of z_{fg} . Third, significant absorption rarely occurs at negative velocities.

These results are further described in Figure 9 which present the Δv_{90} and $\bar{\delta v}$ measurements for C II 1334 and C IV 1548 against impact parameter. These two ions generally exhibit similar kinematic characteristics, consistent with the high ionization fractions estimated for the gas. The Δv_{90} widths for the QPQ8 sample have median values of 555 km s^{-1} for C II and 342 km s^{-1} for C IV, and exhibit no strong correlation with R_{\perp} . These motions greatly exceed the values previously measured for gas tracing galaxies or CGM in absorption. This includes the damped Ly α systems, whose median Δv_{90} for low ion absorption $\approx 80 \text{ km s}^{-1}$ and that for C IV $\approx 170 \text{ km s}^{-1}$ (Prochaska & Wolfe 1997; Neeleman et al. 2013), and also the CGM of L^* galaxies in the low- z universe whose median $\Delta v_{90} \approx 100 \text{ km s}^{-1}$ (Werk et al. 2013). Veloc-

TABLE 5
SUMMARY OF PHYSICAL CONDITIONS

Name	Subsystem	$\log U^a$	$\log < U >^b$	$\log < x_{\text{HI}} >^c$	$\log n_{\text{EUVB}}^d/\text{cm}^{-3}$	$\log n_{\text{QSO}}^e/\text{cm}^{-3}$	$\log n_e^f/\text{cm}^{-3}$	Linear Size ^g (pc)
J0225+0048	A	> -1.8	> -2.0	-3.4	-3.6	-0.8		
	B	$-2.3^{+0.8}_{-0.3}$						
	C	> -2.2						
J0853-0011	A	$-3.2^{+0.5}_{-0.3}$	-3.3	-1.2	-2.2	$+0.6$		
	B	$-3.4^{+0.3}_{-0.3}$						
	C	$-3.1^{+0.3}_{-0.3}$					< 0.9	> 3.8
J0932+0925	A	$-2.7^{+0.3}_{-0.3}$	-2.4	-2.8	-3.1	-0.5	< 1.8	> 0.01
	B	$-2.1^{+0.3}_{-0.3}$						
	C	$-2.7^{+0.3}_{-0.3}$						
J1026+4614	A	$-1.9^{+0.6}_{-0.3}$	-1.9	-3.3	-3.7	-0.6		
	B	$-2.5^{+0.5}_{-0.2}$						
J1038+5027	A	$-2.2^{+0.6}_{-0.3}$	-2.2	-3.3	-3.4	-0.1		
J1144+0959	A	$-1.5^{+0.3}_{-0.3}$	-2.1	-2.4	-3.5	-0.3		
	B	$-1.7^{+0.5}_{-0.3}$						
	C	$-2.8^{+0.3}_{-0.3}$						
	D	$-2.3^{+0.3}_{-0.3}$					< 1.3	> 11.2
	E	$-2.3^{+0.3}_{-0.3}$						
	F	$-2.0^{+0.5}_{-0.3}$					< 0.4	> 239.3
J1145+0322	A	$-2.9^{+0.7}_{-0.4}$	-2.9	-1.8	-2.6	$+0.1$	< 0.6	> 11.8
J1204+0221	A	$-3.3^{+0.3}_{-0.4}$						
	B	$-3.6^{+0.3}_{-0.4}$						
	C	$-3.6^{+0.3}_{-0.4}$					< 0.6	> 2.4
J1420+1603	A	$-2.5^{+0.7}_{-0.4}$	-3.0	-1.6	-2.5	$+1.1$		
	B	$-3.0^{+0.3}_{-0.3}$						
	C	$-3.1^{+0.3}_{-0.3}$						
	D	$-3.0^{+0.3}_{-0.3}$						
	E	$-3.0^{+0.3}_{-0.3}$						
	F	$-2.9^{+0.3}_{-0.3}$					2.2	0.17
J1427-0121	A	$-3.1^{+0.5}_{-0.3}$	< -3.0	-1.3	-2.5	$+1.7$		
	B	$-2.6^{+0.4}_{-0.3}$					< 0.7	> 23.5
	C	< -3.4					1.2	0.97
J1553+1921	A	$-3.2^{+0.3}_{-0.3}$	-3.2	-0.3	-2.3	$+1.2$	$< 2.5^h$	> 7.7
J1627+4605	A	> -2.0	> -2.0	-3.5	-3.7	-0.6		

^a The ionization parameter U for each subsystem comes from Cloudy ionization modeling.

^b The average ionization parameter $< U >$ for the absorption system associated to the foreground quasar is calculated as the U values of its subsystems weighted by their corresponding N_{HI} values.

^c For each subsystem the estimated U will give a corresponding neutral fraction x_{HI} . The average neutral fraction $< x_{\text{HI}} >$ is calculated as the neutral fractions of the subsystems weighted by their N_{HI} .

^d The density required to give the $< U >$ value if the gas is only illuminated by the EUVB and rescaled to match the mean opacity of the Ly α forest.

^e The density required to yield $< U >$ assuming the gas is located at a distance from the quasar equal to the impact parameter and that the quasar emits isotropically.

^f Electron volume density calculated from fine structure excited state to ground state ratios, under the assumption of collisional equilibrium.

^g When the electron volume density is available, we estimated the linear size of the absorbing cloud by $\ell = N_{\text{H}}/n_{\text{H}}$, where $n_{\text{H}} = n_e/(1 - x_{\text{HI}})$, not compensating for ionized helium contribution to electron density.

^h This is a damped Lyman α system and n_{HI} is reported instead of n_e .

ity widths exceeding several hundred km s^{-1} have only been routinely observed ‘down-the-barrel’ to star forming galaxies and AGN themselves, where one probes gas within the galaxy (e.g. Steidel et al. 2010; Hamann 1998). Presently, the QPQ8 sample exhibits the largest velocity widths probed in absorption on CGM scales at any epoch. Existing studies that found large velocity spreads along transverse sightlines around galaxies are limited to single sightlines with most of the gas within a few hundred km s^{-1} (e.g. Tripp et al. 2011), gas tracing a higher ionization state (e.g. Churchill et al. 2012), average velocity spread smaller than that measured in QPQ8 (e.g. Gauthier 2013; Muzahid et al. 2015; Zahedy et al. 2016),

or the velocity spreads are not well quantified (e.g. Johnson et al. 2015). We further emphasize that this result follows from the systematically large equivalent widths observed in the full QPQ sample (e.g. QPQ5, QPQ7). Therefore despite the small sample size of QPQ8 we consider the distribution of large Δv_{90} values to be a statistically strong result.

The lower panel of Figure 9 shows the velocity offsets δv for the sample, restricting to absorption systems with precise Mg II or near IR measurements for z_{fg} . The δv values range from $\approx -500 \text{ km s}^{-1}$ to $\approx +500 \text{ km s}^{-1}$ with an RMS of 261 km s^{-1} and 408 km s^{-1} for C II and C IV respectively. The δv values frequently match

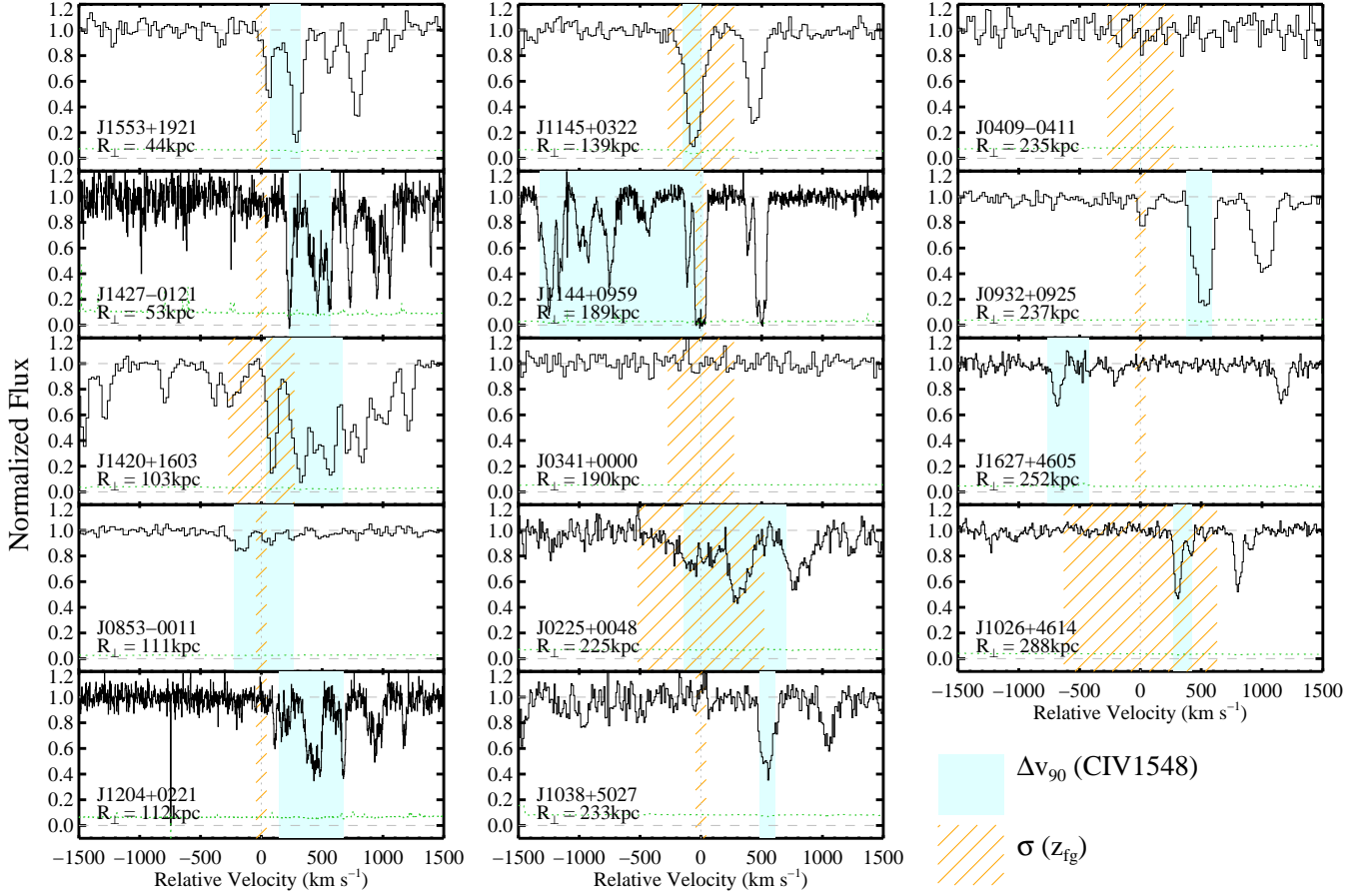


FIG. 8.— C IV 1548 absorption profiles associated with the foreground quasars. The cyan shade encompasses 90% of the optical depth of the C IV 1548 transition. The orange shade marks the 1σ uncertainty in z_{fg} . When detected, the C II 1334 profiles show similar velocity widths. The gas exhibits velocity widths ranging from $\approx 50 \text{ km s}^{-1}$ to nearly 1500 km s^{-1} . The centroids tend to occur within 500 km s^{-1} . Significant absorption rarely occurs at negative velocities. The green histogram shows the 1σ noise in the normalized flux.

or exceed the velocity width, implying that the absorption often occurs to only positive or negative velocities relative to z_{fg} . Furthermore the δv values of our sample appear to preferentially exhibit positive values. For C IV, only 2 of the 10 profiles have $\delta v \ll 0 \text{ km s}^{-1}$ and the median measurement is $+282 \text{ km s}^{-1}$. Of course, the skewness of the δv distribution may be dominated by sample variance and therefore must be confirmed with a larger sample of pairs (see QPQ9). The result does follow, however, a reported asymmetry in H I in an independent quasar pair sample (Kirkman & Tytler 2008).

We further illustrate the kinematic characteristics of the gas by constructing the average optical depth profiles for the QPQ8 sample. We interpolated the apparent optical depth of each transition onto a fixed velocity grid with 25 km s^{-1} pixels and normalized each to have a peak $\tau_i = 1$. We then performed a straight average of all the profiles. For systems where the C IV doublet self blends, we estimated the optical depth of C IV 1548 in the overlap spectral region from the unblended portions of the doublet. The details of the treatment are in the Appendix. Figure 10 shows the average optical depth profiles. These further emphasize the large velocity widths and the tendency toward positive velocities.

Taking the ensemble of QPQ8 data as a statistical rep-

resentation of the CGM surrounding quasars, we may estimate the RMS of the CGM surrounding quasars σ_v from the average profile. Measuring this dispersion relative to the profile centroid, instead of $v = 0 \text{ km s}^{-1}$, we recovered $\sigma_v = 249 \text{ km s}^{-1}$ for C II and $\sigma_v = 495 \text{ km s}^{-1}$ for C IV. A large σ_v value for C IV is representative of the sample. Even if we take out the two sightlines with the largest velocity dispersion, i.e. J0225+0048 and J1144+0959, we still get $\sigma_v = 388 \text{ km s}^{-1}$.

In QPQ3, we argued the extreme kinematics of J1204+0221 ($\Delta v_{90} \approx 650 \text{ km s}^{-1}$) could be consistent with the one dimensional velocity dispersion of a massive dark matter halo. We assumed a dark matter halo mass of $10^{13.3} M_\odot$ and estimated a line-of-sight velocity dispersion of $\sigma_{1D} \approx 431 \text{ km s}^{-1}$ according to Tormen (1997) and assuming an NFW halo with concentration parameter $c = 4$. More recent analysis of quasar clustering prefers a lower typical mass ($10^{12.5} M_\odot$), giving $\sigma_{1D} = 212 \text{ km s}^{-1}$. At this mass scale, we consider it improbable that the velocity widths we have observed are entirely virialized motions, and thus likely require non-gravitational kinematics i.e. outflows. Note that satellite galaxies within the halo should follow the potential and have a similar line-of-sight velocity dispersion. If galaxies clustered to the quasar host on larger

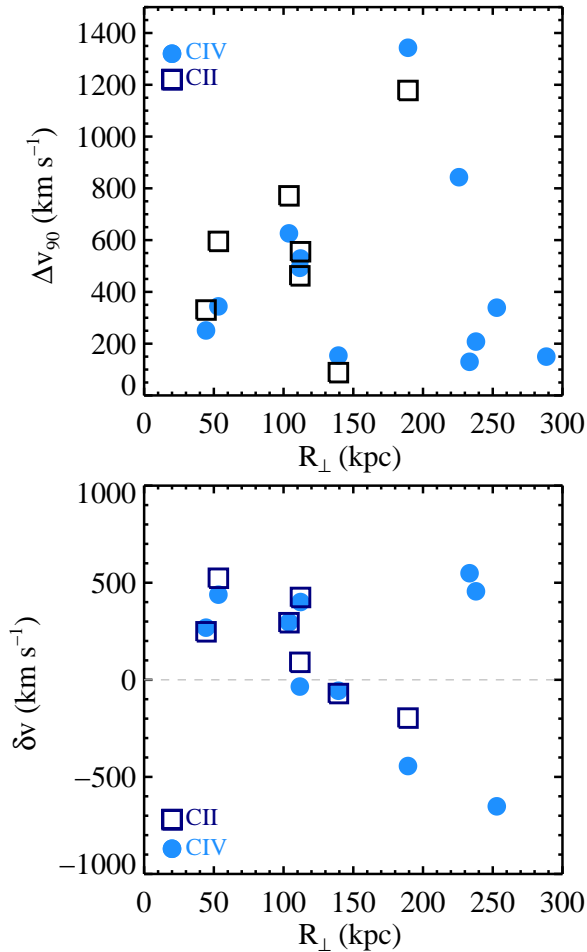


FIG. 9.— (Top) Measurements of the Δv_{90} statistic for low ion absorption in open squares and high ion absorption in filled circles. The absorptions within $R_{\perp} \leq 200$ kpc show very large Δv_{90} values. This distribution exceeds all previous measurements for gas surrounding galaxies (e.g. Prochaska & Wolfe 1997; Neeleman et al. 2013; Werk et al. 2013). (Bottom) Velocity offsets δv between the optical depth weighted centroid of the absorption profiles and the systemic redshift of the foreground quasar. The δv values typically match or exceed the Δv_{90} value, indicating that a majority of gas occurs on one side of systemic. In this small sample, there is an apparent bias to positive velocities.

scales also contribute to the observed velocity widths, the widths will partly represent Hubble flow of non-collapsed material. This scenario is rather unlikely, however, and the probability intercepting a random optically thick absorber is only $\approx 4\%$, and clustering would only increase that to 24% according to QPQ6 (also see the discussion in Johnson et al. (2015)). We eagerly await advances in hydrodynamic simulations of massive $z \sim 2$ galaxies to explore these scenarios. The greatest challenge may for such feedback to manifest itself as cool, optically thick gas on CGM scales (Faucher-Giguère & Quataert 2012). Although Faucher-Giguère et al. (2016) is able to reproduce the high covering fraction of optically thick gas, their velocity fields are not extreme enough.

Recently, Johnson et al. (2015) have studied the CGM surrounding $z \sim 1$ quasars using QPQ techniques, and reported 40% of the Mg II absorption occurs at radial velocities exceeding the expected average virial velocity 300 km s^{-1} , which they interpret as quasar driven outflows. For the QPQ8 sample, we found 4 out of 7

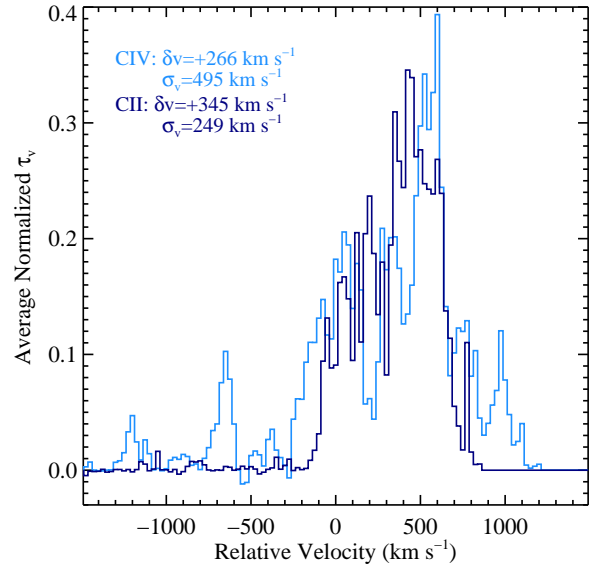


FIG. 10.— Average optical depth profiles of the QPQ8 sample, generated from the ensemble with each normalized to peak optical depth of 1. These profiles stress the large velocity widths of the gas and also a peculiar bias toward positive velocity relative to systemic.

C II systems and 8 out of 10 C IV systems exhibit $\bar{\delta v}$ exceeding the one-dimensional virial velocity (see Figure 9). To allow a one-to-one comparison between our results and Johnson et al. (2015), we quote 2 out of 7 C II systems and 6 out of 10 C IV systems exhibit $\bar{\delta v}$ exceeding 300 km s^{-1} . This is consistent with Johnson et al. (2015), especially considering the higher random probability for C IV absorbers.

However, we caution that the mere presence of a few large kinematic offsets cannot be used to make the case against gravitational motions, unless the shift is of order $\sim 1000 \text{ km s}^{-1}$, such as the J1144+0959 absorption system of QPQ8. Clustering only constrains the average mass of the dark matter halos occupied by quasars, but not the distribution function. The halo mass occupation distribution could be very broad, or have significant tails, which could both give rise to occasional large velocity shifts, which would not require non-gravitational kinematics. (On a side note, despite the large velocity shift of the J1144+0959 absorption system from z_{fg} , in the Appendix we demonstrated that it is likely the gas is physically associated to the quasar. For random incidence, the probability of finding one such strong C IV absorber is only 3%, with an even smaller probability for C II absorber. Clustering would at most quadruple this estimate.)

Moreover, the [O III] emission occasionally exhibits a significant blue-shifted tail relative to the systemic defined by [O II] (see Figure 2). Systematic shifts from redshift errors on the order of 200 km s^{-1} are occasionally expected (Boroson 2005). A second caveat is that we used a mixture of [O III] and Mg II systemic redshifts, the latter being less accurate.

Now consider the putative bias to positive velocities that is apparent in Figure 10. Because the sightlines penetrate the entire halo, there is an inherent symmetry to the experiment. Both random velocity fields (e.g. random sampling of a virialized ensemble of CGM gas) and

coherent velocity fields (e.g. outflow) will therefore yield symmetric absorption about $v = 0 \text{ km s}^{-1}$. If the apparent asymmetry in Figure 10 is confirmed with a larger sample, one may require a non-dynamical process to provide the asymmetry. One possibility is an asymmetric radiation field that preferentially ionizes the gas moving towards the observer, i.e. where the quasar is known to shine. The quasar is obscured in the direction pointing away from us, and the gas observed in absorption lies preferentially behind the quasar and is shadowed. One may either interpret the redshift as an organized velocity field of flow away from the galaxy, or interpret the velocity as a proxy for distance along the line-of-sight, as it would be if the material is in the Hubble flow and hence this asymmetry arises from a transverse proximity effect. There is no known case for a quasar shining only towards us, however. Another explanation is that, given the finite lifetime of quasar episodes, light from the background quasar may arrive at absorbers behind the foreground quasar before the ionizing radiation from the foreground quasar arrives. On the other hand, light from the background quasar will need to travel larger distances to reach the absorbers in front of the foreground quasar and hence allow more time for the foreground quasar's radiation to reach and ionize them (see Figure 8 of Kirkman & Tytler 2008). We note, however, Shen & Ho (2014) and Shen et al. (2016) found a correlation between the fraction of total [O III] flux that is in the blueshifted wing and quasar luminosity. The putative redshift of absorbing components relative to the systemic is subject to redshift determination errors. We defer a more elaborated discussion to future papers which focus on the kinematics. We are assembling a much larger sample of pairs with precise redshift measurements to better resolve this kinematic signature, using metal absorption lines to study on gas on CGM scales (Prochaska et al. in prep.; QPQ9) and H I to probe gas on larger scales in the Ly α forest (Hennawi et al. in prep.).

4.2. Chemical Abundances

The frequent detection of metal line absorption in the CGM surrounding quasars, even at low spectral resolution (QPQ5, QPQ7), implies a significant enrichment of the gas in heavy elements. Quantitative estimates for the metallicity, however, require an assessment of the ionization state because the observed atoms in a given ionization state may only comprise a small fraction of the total hydrogen and metal column densities. Furthermore, high spectral resolution is necessary to precisely estimate the column densities and to assess line saturation. With the majority of the QPQ8 sample, we satisfy both of these requirements and may constrain the chemical abundances for a set of elements.

Consider first an estimate for the metallicity [M/H] of each pair in the QPQ8 sample, i.e. an assessment of the heavy element enrichment for the gas comprising the CGM. In what follows, we focus on the cool gas by emphasizing the subsystems that dominate the H I absorption in each pair. While the more highly ionized subsystems may have a large total column N_{H} (e.g. Crighton et al. 2013), these components are subject to greater uncertainties in the ionization modeling and may better track a more highly ionized phase that is physically distinct from the cool CGM. Therefore, we report average

abundances by weighting the results of each subsystem by our N_{HI} estimate instead of N_{H} . We have calculated [M/H] values weighted by N_{H} instead of N_{NHI} , and found very similar values for each absorption system.

Although we have constrained ionization models for the majority of our sample, we emphasize that the data exhibit positive detections of the O I 1302 transition for 7 of the 14 pairs. In these cases, we may estimate [M/H] directly from the measured O^0/H^0 ratio, i.e. $[\text{O}/\text{H}] = \log N(\text{O}^0) - \log N_{\text{HI}} - \epsilon_{\text{O}} + 12$, where ϵ_{O} is the solar abundance of oxygen on logarithmic scale, with the expectation that ionization corrections are small. This assertion follows from the very similar ionization potentials of these atoms and the charge exchange reactions that couple their ionization for a range of physical conditions. When $N_{\text{HI}} < 10^{19} \text{ cm}^{-2}$ or $\log U > -2$, however, the O^0/H^0 ratio may underestimate [O/H], especially in the presence of a hard radiation field (e.g. QPQ3). In this respect, [O/H] estimated without any ionization correction provides a conservative lower bound to [M/H]. We are further motivated to focus first on oxygen because this element frequently dominates by mass and number among the heavy elements.

Roughly half of the systems showing O I detections have saturated profiles yielding only lower limits to [O/H]. For these cases we set an additional upper bound to [M/H] from our analysis of [Si/H]. We set the upper bound to [M/H] from the Si^+/H^0 measurements incremented by the 2σ uncertainty in the estimated ionization corrections. For systems where Si II absorption occurs in multiple subsystems, we adopt the N_{HI} weighted [Si/H] value to emphasize the cool gas expected to dominate the H I absorption. We found [O/H] is often larger than [Si/H], and for cases where the [Si/H] value exceeds the lower limit from [O/H] we adopted the former. In one other case where the [O/H] estimate requires a large ionization correction, J1144+0959 (see below and the Appendix), [Si/H] is adopted for the metallicity estimate.

The resulting distribution of [M/H] for these 7 systems, all of which have $N_{\text{HI}} > 10^{18} \text{ cm}^{-2}$, is presented in Figure 11. All of the measurements exceed 1/10 solar and the median metallicity is -0.60 dex . This is a conservative value because three of the measurements are formally lower limits and because ionization corrections to O^0/H^0 would only increase [M/H]. Furthermore, the N_{HI} values estimated for these systems are more tightly bounded on the upper end by the absence of damping wings, and lower N_{HI} values would yield even higher [M/H]. We conclude that the cool CGM surrounding massive $z \sim 2$ galaxies hosting quasars has a median [M/H] of at least 1/3 solar.

There are four highly ionized systems at $R_{\perp} > 160 \text{ kpc}$ that offer estimates on the enrichment of the extended CGM from analysis of Si^{2+} (J0932+0925) or Si^{3+} (J0225+0048, J1026+4614, J1038+5027). In two of these cases, the estimates have uncertainties exceeding 1.0 dex because of poor constraints on the ionization state and/or N_{HI} . These are not considered further. One other highly ionized system at $R_{\perp} > 160 \text{ kpc}$ (J1627+4605) exhibits only C^{3+} and is also not considered further. Lastly, two systems exhibit no positive detection of heavy elements (J0341+0000, J0409-0411). While this could reflect a very metal poor gas,

TABLE 6
CHEMICAL ABUNDANCES

Quasar Pair	$\log N_{\text{HI}}/\text{cm}^{-2}$	[M/H]	[O/H] ^a	[Si/H] ^a	[Fe/H] ^a	[C/H] ^a	Comment
J0225+0048	18.9	$-1.5^{+1.0}_{-1.0}$ ^g		$-1.5^{+1.0}_{-1.0}$ ^k		$-2.8^{+9.8}_{-1.1}$ ^k	N_{HI} very uncertain.
J0341+0000	16.6						No metals detected.
J0409-0411	14.2						No metals detected.
J0853-0011	18.8	$-0.6^{+0.2}_{-0.2}$ ^b	$-0.6^{+0.2}_{-0.2}$ ^h	$-1.0^{+0.3}_{-0.6}$ ⁱ	$-1.4^{+0.2}_{-0.6}$ ⁱ	> -1.4 ⁱ	
J0932+0925	15.7	$0.1^{+0.4}_{-0.4}$ ^f		$0.1^{+0.4}_{-0.4}$ ^j		$-0.0^{+0.7}_{-0.8}$ ⁱ	
J1026+4614	15.4	$-0.2^{+0.8}_{-0.2}$ ^g		$-0.2^{+0.8}_{-0.2}$ ^k		$-0.5^{+0.5}_{-0.4}$ ^k	
J1038+5027	16.9	$-1.5^{+0.8}_{-0.5}$ ^g		$-1.5^{+0.8}_{-0.5}$ ^k		$-1.6^{+0.9}_{-0.7}$ ^k	U value very uncertain.
J1144+0959	18.7	$-1.5^{+0.2}_{-0.4}$ ^e	$-1.9^{+0.2}_{-0.2}$ ^h	$-1.5^{+0.2}_{-0.4}$ ⁱ	$-0.3^{+0.9}_{-0.6}$ ⁱ	> -2.1 ⁱ	
J1145+0322	18.4	$-1.0^{+0.2}_{-0.2}$ ^b	$-1.0^{+0.2}_{-0.2}$ ^h	$-1.1^{+0.4}_{-0.4}$ ⁱ	$-0.8^{+0.6}_{-0.4}$ ⁱ	> -1.2 ⁱ	
J1204+0221	19.7	$-0.6^{+0.3}_{-0.3}$ ^c	> -0.6 ^h	> -0.7 ⁱ	$-1.3^{+0.2}_{-0.2}$ ⁱ	> -1.0 ⁱ	
J1420+1603	19.2	$-0.3^{+0.2}_{-0.2}$ ^c	> -0.3 ^h	$-1.0^{+0.4}_{-0.4}$ ⁱ	$-0.9^{+0.4}_{-0.4}$ ⁱ	> -0.7 ⁱ	
J1427-0121	18.4	$-1.1^{+0.2}_{-0.2}$ ^b	$-1.1^{+0.2}_{-0.2}$ ^h	$-2.1^{+0.2}_{-1.3}$ ⁱ		$-1.7^{+0.2}_{-1.4}$ ⁱ	
J1553+1921	20.2	$-0.6^{+0.2}_{-0.2}$ ^e	> -1.8 ^h	$-0.6^{+0.2}_{-0.2}$ ⁱ	$-1.7^{+0.1}_{-0.1}$ ⁱ	> 0.2 ⁱ	
J1627+4605	16.9						Only C IV detected.

^a Errors in abundances are propagated from errors in HI and metal ion column densities and errors in ionization parameter values.

^b Adopted [O/H] from OI/II values.

^c Adopted [O/H] from OI/II as lower limit, capped by [Si/H] measurement. See the main text for details.

^d Adopted [O/H] lower limit. No QPQ8 systems match this case.

^e Adopted [Si/H] from SiII/III values with ionization corrections, including cases where [Si/H] > [O/H] lower limit. See the text.

^f Adopted [Si/H] from SiIII/III values with ionization corrections.

^g Adopted [Si/H] from SiIV/III values with ionization corrections.

^h Using OI/II as a proxy.

ⁱ Measured from the first ionization state of the element, with ionization corrections applied.

^j Measured from the second ionization state of the element, with ionization corrections applied.

^k Measured from the third ionization state of the element, with ionization corrections applied.

the observed H I absorption is also very weak ($N_{\text{HI}} < 10^{15} \text{ cm}^{-2}$) and the absence of heavy elements may simply reflect the absence of a substantial cool CGM along those sightlines.

Figure 11 shows all of these [M/H] estimates for the cool gas of the full QPQ8 sample, and Table 6 lists their values. The measurements exhibit no strong correlation with H I column density or impact parameter. Indeed, there is evidence for significant enrichment of the gas even beyond the estimated virial radius of the halos hosting quasars. In QPQ7, we conservatively estimated a gas minimum metallicity of 1/10 solar for the CGM and inferred metal masses $> 10^7 M_{\odot}$. In QPQ5, we estimated a maximum metallicity of 1/2 solar and inferred an upper bound on metal masses $< 10^9 M_{\odot}$. The results presented here indicate metallicities that are several times higher. With the Si measurements scaled to O assuming solar relative abundance, we derive a median metal column density of $10^{16.7} \text{ cm}^{-2}$ for the 7 sightlines within 200 kpc. This corresponds to a total oxygen mass in the cool CGM of $M_{\text{O}}^{\text{CGM}} \approx 4.9 \times 10^8 M_{\odot} (R_{\perp}/160 \text{ kpc})^2$. Furthermore, assuming that oxygen accounts for 44% of the metal mass (Asplund et al. 2009), we refined our mass estimate to be $M_{\text{metal}}^{\text{CGM}} = 1.1 \times 10^9 M_{\odot} (R_{\perp}/160 \text{ kpc})^2$. Theoretical calculations of core-collapse supernovae nucleosynthesis yields (Sukhbold et al. 2016; Nomoto et al. 2006) predict an oxygen yield mass fraction of 0.008, scaled to a Kroupa initial mass function. Thus, the total stellar mass that must have formed to synthesize all the oxygen in the cool CGM, not accounting for oxygen locked up in stellar content, in the ISM or in the warm-hot/hot phase CGM, has to be $M_{*} > 6.1 \times 10^{10} M_{\odot} (R_{\perp}/160 \text{ kpc})^2$.

To form this stellar mass by $z = 2.4$, the median z_{fg} of the QPQ8 sample, the average star formation rate required is $> 34 M_{\odot} \text{ yr}^{-1}$ if the galaxies first formed at $z \sim 6$. From halo abundance matching techniques (Behroozi et al. 2013), the typical host galaxy stellar mass of the QPQ8 sample is $M_{\text{gal}} = (6 \pm 3) \times 10^{10} M_{\odot}$. Whitaker et al. (2014) gives the star formation rate of the star forming sequence at $z \sim 2-3$ at this galaxy mass to be $100 M_{\odot} \text{ yr}^{-1}$. Our estimate of the minimum average star formation rate required, and hence the total oxygen mass in the cool CGM, is consistent with the instantaneous total star formation rate inferred from these scaling relations.

We have also examined the abundance ratios of a subset of the elements, restricting this analysis to low ions to minimize the effects of ionization. We focus on O/Fe which is a chemical signature of the supernovae that have enriched the gas. High values are indicative of massive stellar nucleosynthesis, i.e. core-collapse supernovae, whereas low values imply substantial enrichment by Type Ia supernovae (e.g. Tinsley 1979).

Figure 12 presents [O/Fe] estimates after adopting the ionization corrections from our favored models against the N_{HI} measurements. Nearly all of the measurements indicate a supersolar O/Fe ratio, implying a significant fraction of the CGM surrounding quasars must have an enhanced α/Fe abundance. The obvious exception is subsystem F from the J1144+0959 pair. Perhaps not coincidentally, this subsystem has the highest estimated U parameter of those that exhibit O or Fe, and therefore has the largest ionization correction for $\{\text{O}^0/\text{Fe}^+\}$. The corrected [O/Fe] value is still subsolar, although we

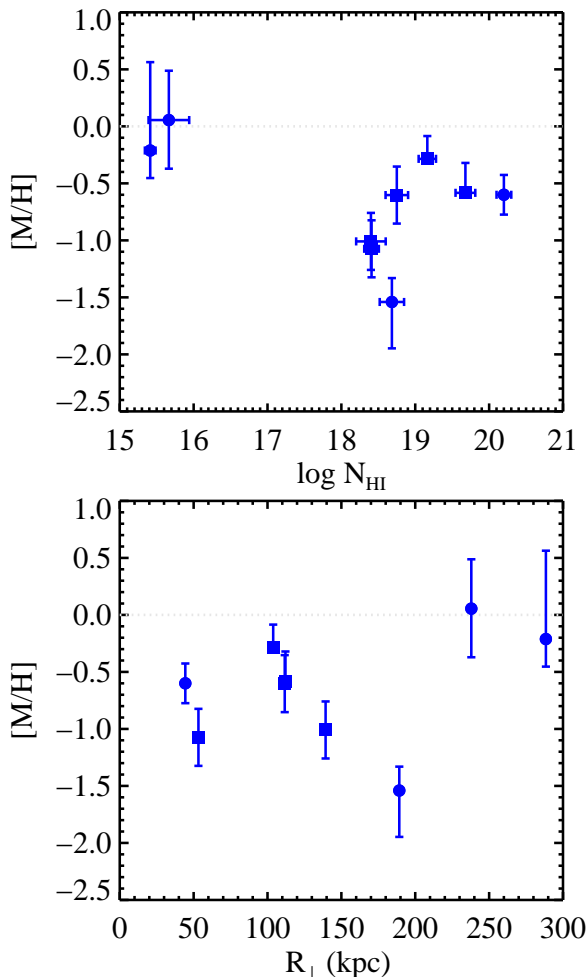


FIG. 11.— All metallicity estimates for the cool gas of the full sample, estimated from the O I, Si II, Si III or Si IV columns with ionization corrections from Cloudy. Estimations from O I are plotted with squares and estimations from Si ions are plotted with circles. All measurements exceed 1/10 solar and the median $[M/H] = -0.60$ dex. The measurements exhibit no correlation with N_{HI} or R_{\perp} . Significant enrichment exists even beyond the estimated virial radius of the host halos at ≈ 160 kpc. Note in the $[M/H]$ versus R_{\perp} subplot, there are two almost overlapping points at $R_{\perp} = 112$ kpc.

caution that the uncertainty is many tenths dex given the high U value. Furthermore, the $[O/Fe]$ values from QPQ8 show a large dispersion spanning two orders of magnitude.

In summary, the cool gas surrounding $z \sim 2$ massive galaxies hosting quasars to ≈ 200 kpc is highly enriched and α -enhanced. This implies that the gas expelled from these galaxies (and their progenitors) was enriched primarily by core-collapse supernovae. Furthermore, if supernovae explosions are the principal factor in transporting metals to the CGM, we may speculate that core-collapse supernovae dominate in high- z massive galaxies hosting quasars.

The high $[\alpha/Fe]$ enhancement suggest a star formation history similar to elliptical galaxies (e.g. Matteucci 1994; Conroy et al. 2014), which these quasar host galaxies are expected to evolve into. Currently there are three competing models that explain $[\alpha/Fe]$ enhancement in the *stellar* content of elliptical galaxies (1) selective loss of Fe via galactic winds (Trager et al. 2000); (2) a short

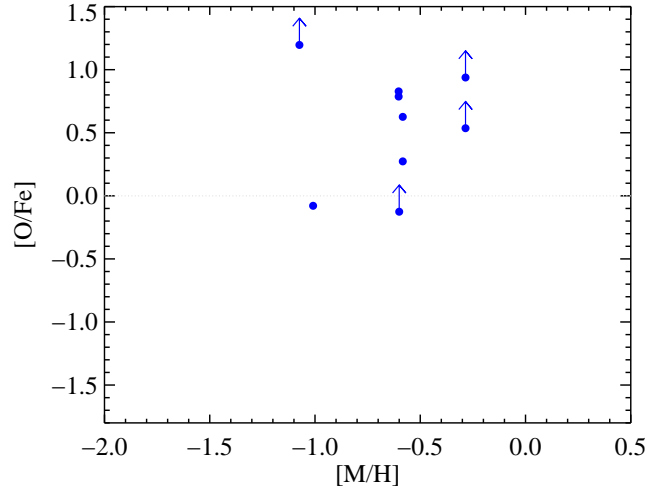


FIG. 12.— $[O/Fe]$ estimates after adopting the ionization corrections to O^0/Fe^+ . Nearly all measurements indicate supersolar O/Fe ratio, implying a significant fraction of the CGM surrounding quasars must have enhanced α/Fe abundance. Our findings suggest a star formation history similar to elliptical galaxies and a starburst that lasted less than 1 Gyr.

starburst that ceased before Fe produced from Type Ia supernovae became available for incorporation into new stars; and (3) a variable initial mass function flattened at the high mass end (Thomas 1999). Our finding that the CGM shows a high $[\alpha/Fe]$ enhancement strongly disfavors the scenario where more Fe than α elements is selectively ejected through outflows. It is more likely that the supersolar α/Fe ratios reflect an intrinsic nucleosynthetic enhancement. This conclusion is further strengthened by X-ray observations of the hot interstellar medium of early type galaxies (Loewenstein & Davis 2010, 2012; Konami et al. 2014) and the hot intracluster medium (Sato et al. 2007; Mushotzky et al. 1996) where enhanced α/Fe ratios are similarly found (but see Simionescu et al. 2015). Furthermore, if without a flatter initial mass function, the starburst driven galactic scale winds must occur before the Fe production from Type Ia supernovae starts to become important, hence we expect the duration of starburst lasts less than 1 Gyr. In turn this implies a minimum star formation rate $> 55 M_{\odot} \text{ yr}^{-1}$ based on the inferred total stellar mass formed for synthesizing all oxygen in the cool CGM.

4.3. Surface Density Profiles

Figure 13 presents scatter plots of the H I column density measurements against projected quasar pair separation R_{\perp} calculated at z_{fg} . Figure 14 presents scatter plots of the C II column density measurements against projected quasar pair separations R_{\perp} calculated at z_{fg} . Both ions exhibit a decline in surface density with increasing R_{\perp} . Statistically a Kendall's tau test gives a 99.8% probability that the null hypothesis of no correlation between N_{HI} and R_{\perp} is ruled out. A generalized Kendall's tau test gives a 98.7% probability that the null hypothesis of no correlation between N_{CII} and R_{\perp} is ruled out, and we expect the correlation to be stronger because the N_{CII} absorptions detected at small R_{\perp} are saturated and N_{CII} is not detected at 3- σ confidence at large R_{\perp} . The observed low ion absorption is thus trac-

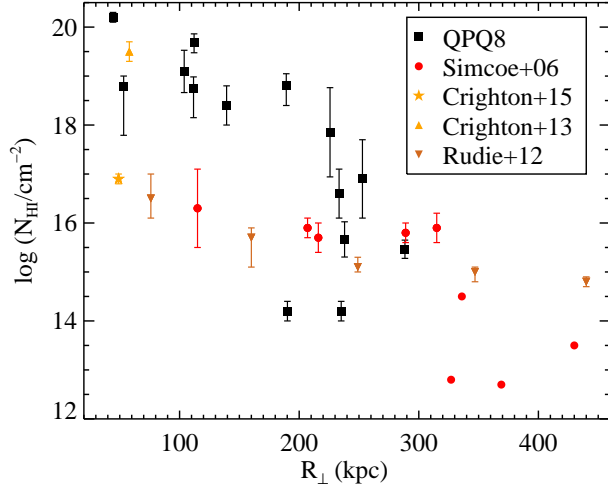


FIG. 13.— Scatter plots of N_{HI} measurements against projected quasar pair separation calculated at z_{fg} . The H I exhibits a statistically significant decline in surface density with R_{\perp} . Strong H I absorption exists even beyond the estimated virial radius ≈ 160 kpc. For comparison we also plot CGM N_{HI} measurements of $z \sim 2-3$ galaxies from the literature as a function of projected distance from the galaxies. At $R_{\perp} \leq 200$ kpc, the N_{HI} values of QPQ8 predominate those of coeval galaxies.

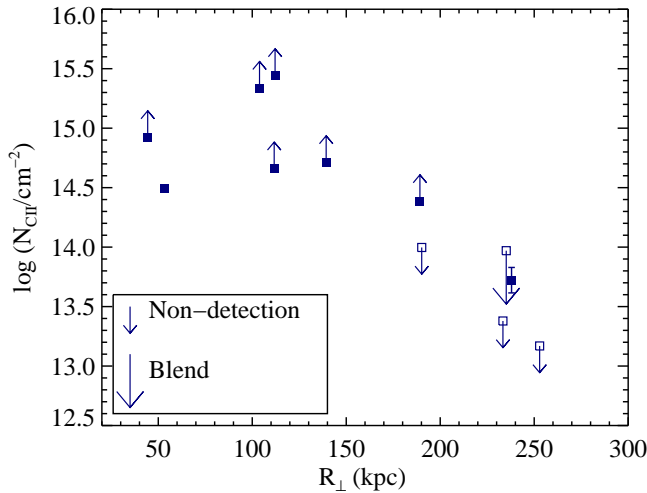


FIG. 14.— Scatter plots of N_{CII} measurements against R_{\perp} . Similar to H I, the C II ion exhibits a statistically significant decline in surface density with R_{\perp} . The observed low ion absorption thus traces the CGM gas of the foreground quasar.

ing the CGM gas of the foreground quasar. We further note that strong H I absorption exists even beyond the estimated virial radius ≈ 160 kpc.

For comparison, in Figure 13 we also plot the work of Simcoe et al. (2006); Rudie et al. (2012); Crighton et al. (2013, 2015) of N_{HI} as a function of R_{\perp} in the CGM of $z \sim 2-3$ galaxies, in which R_{\perp} refers to the transverse, physical distance. Their work uses background quasars as sightlines to probe the CGM of foreground galaxies. Their galaxies typically have $M_{*} \sim 1 \times 10^{10} M_{\odot}$, which characterize the typical stellar mass in star forming galaxies at $z \sim 2-3$, while the typical host galaxy of the QPQ8 sample inferred from halo abundance matching has $M_{*} \sim 6 \times 10^{10} M_{\odot}$, i.e. much more massive. At $R_{\perp} \approx 200-300$ kpc, the QPQ8 N_{HI} values smoothly

join those measured for the more typical $z \sim 2-3$ star forming galaxy population, which are still significantly enhanced compared to the IGM absorption at $\gtrsim 300$ kpc. At $R_{\perp} \lesssim 200$ kpc, we find the N_{HI} values of the QPQ8 sample are significantly larger than that of the coeval galaxies, as inferred previously from equivalent width measurements (QPQ5, QPQ6).

We calculated the H I mass in the cool CGM by considering the R_{\perp} values as annular bins. We calculated the mass in the i -th annulus by $M_i = N_{\text{HI}}(R_i) m_{\text{H}} \pi (R_i^2 - R_{i-1}^2)$ and summed up the mass in all annuli. The total H I within 160 kpc is then found to be $M_{\text{HI}}^{\text{CGM}} = 1.3 \times 10^{10} M_{\odot}$. Even without any ionization correction, we infer the baryonic mass of the cool CGM approaches the stellar mass. In a highly clustered environment, the observed gas could be contributed by CGM of neighboring galaxies. In this regard, the H I mass estimate can be considered an upper limit.

Concerning the C II ion, the absorption within $R_{\perp} < 200$ kpc is strong and saturated, with a median $N_{\text{CII}} > 14.7 \text{ cm}^{-2}$, indicating a substantial metal mass. At $R_{\perp} > 200$ kpc, we have one solid detection of C II in the J0932+0925 system, two non-detections in the J1038+5027 system and the J1627+4605 system shown as 3σ upper limits in Figure 14, and one system J0409-0411 whose C II is blended with unrelated intergalactic absorption, depicted by a large downward arrow. Our results quantitatively assert the conclusion of QPQ7 that the gas surrounding massive, $z \sim 2$ galaxies hosting quasars represents the pinnacle of the cool CGM, in terms of the neutral hydrogen mass and the enrichment.

We detect cool enriched gas transverse to the sightline to the foreground quasars to at least ≈ 200 kpc. Our results indicate the quasar plays a minor role in producing the cool CGM, and our argument is as follows. Observations of spatial clustering of quasars (Haiman & Hui 2001; Martini & Weinberg 2001; Martini 2004), observations of the transverse proximity effect in He II (Jakobsen et al. 2003), as well as galaxy merger simulations that include supermassive black holes (Hopkins et al. 2005), all constrain the quasar lifetime to be 10^6-10^8 years, with a preference for 10^7 years. Should the velocities represent outflows, given that the line-of-sight velocity dispersion is 249 km s^{-1} in C II and 495 km s^{-1} in C IV, as discussed in Section 4.1, even if the observed quasar episode has been active for 10^8 years and accelerate material to 500 km s^{-1} , this gas would only reach 50 kpc. It is unlikely the observed quasar episode alone could transport all of this cool material from the interstellar medium of the galaxies. Furthermore, we found no statistically significant trend between C II column density and quasar luminosity L_{bol} or the UV enhancement factor g_{UV} , contrary to the claims in Johnson et al. (2015) where they investigated Mg II in $z \sim 1$ quasar CGM. We caution the readers, however, that the mean L_{bol} of QPQ8 is $10^{46.4} \text{ erg s}^{-1}$, which is nearly an order of magnitude higher than the mean L_{bol} of the Johnson et al. (2015) sample at $10^{45.5} \text{ erg s}^{-1}$.

As described in Section 3.3, we modeled the ionization state and calculated N_{H} for each absorption system. In Figure 15 we plot N_{H} as a function of R_{\perp} . Consistent with expectation, we do not observe any significant variation of N_{H} with R_{\perp} up to ≈ 200 kpc, as both N_{HI} and

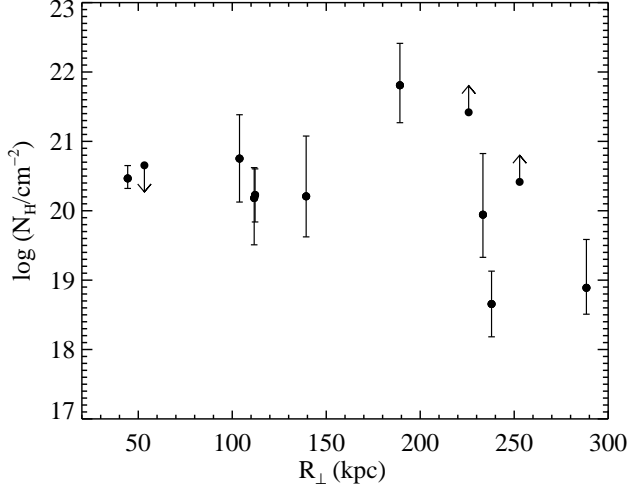


FIG. 15.— The total H column from ionization state modeling as a function of R_{\perp} . We see little evolution in N_{H} up to ≈ 200 kpc, as both N_{HI} and the neutral fraction x_{HI} anticorrelate with R_{\perp} . The median $N_{\text{H}} = 10^{20.5} \text{ cm}^{-2}$.

the neutral fraction x_{HI} anticorrelate with R_{\perp} .

Using the median $N_{\text{H}} = 10^{20.5} \text{ cm}^{-2}$ and the median $[\text{M}/\text{H}] = -0.6$ (Figure 11) within 200 kpc, we constructed cumulative mass profiles of total H and metals in the cool CGM, and the results are plotted in Figure 16. For reference, we also included the expected baryonic mass projected profile of an NFW halo with concentration parameter $c = 4$ (Navarro et al. 1997) and dark matter mass $M_{\text{DM}} = 10^{12.5} M_{\odot} (R_{\perp}/160 \text{ kpc})^2$. We assumed the cosmic baryon fraction 0.17. We also plotted the typical host galaxy mass of the QPQ8 sample using halo abundance matching techniques (Behroozi et al. 2013) and assuming a 50% gas fraction, as well as the range of supermassive black hole mass of the QPQ8 sample, calculated from the bolometric luminosity of the quasars and assuming an eddington ratio $f_{\text{Edd}} = 0.1$. We estimated the total mass of the cool CGM as $M_{\text{cool}}^{\text{CGM}}(R_{\perp}) \approx 1.9 \times 10^{11} M_{\odot} (R_{\perp}/160 \text{ kpc})^2$. Since the median N_{H} of the sample is not sensitive to one system with the highest N_{H} , namely J1144+0959, our estimate of the cool CGM mass is representative of the sample. In QPQ7 we estimated an infall time $\tau_{\text{infall}} \lesssim 1$ Gyr. The corresponding cool gas inflow rate $M_{\text{cool}}^{\text{CGM}}/\tau_{\text{infall}}$ exceeds $100 M_{\odot} \text{ yr}^{-1}$. This is comparable to the star formation rate of massive star forming galaxies at $z \sim 2$, and is enough to fuel star formation for at least 1 Gyr. The QPQ8 results further strengthen the conclusion of QPQ3 and QPQ7 that quasars are unlikely to quench star formation at $z \sim 2$.

It can be seen in Figure 16 that at the virial radius the cool gas fraction accounts for only $\approx 1/3$ of the total expected baryonic mass. Together with the galaxy's stellar and gas mass, they account for $\approx 56\%$ of the total baryonic budget. Modern X-ray observations of the hot intracluster medium at $z \gtrsim 1$ (Baldi et al. 2012; Andreon 2012) report metallicities $\approx 1/3$ solar, which is consistent with the median $[\text{M}/\text{H}] = -0.6$ dex found for the cool CGM in this work. If we assume $[\text{M}/\text{H}] = -0.6$ is a good representation of the metallicity of the cool and the hot phase CGM, then likewise to the total H, at the virial radius the cool CGM only accounts for $1/3$ of the total expected metal mass. A massive reservoir of warm/hot,

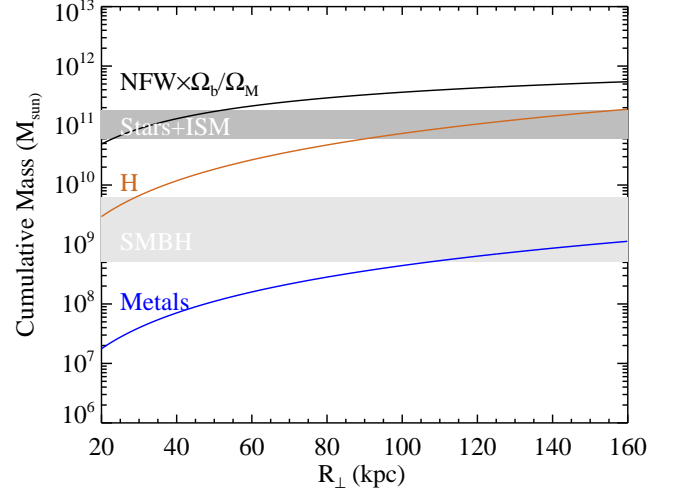


FIG. 16.— Using the median N_{H} and the median $[\text{M}/\text{H}]$ within 200 kpc, we constructed cumulative mass profiles of total H and metals in the cool CGM. For reference we also included the expected baryonic mass projected profile of an NFW halo with $c = 4$ and dark matter mass $M_{\text{DM}} = 10^{12.5} M_{\odot} (R_{\perp}/160 \text{ kpc})^2$. We also plotted the typical host galaxy mass, as well as the range of supermassive black hole mass of the QPQ8 sample. We estimated the total mass of the cool CGM as $M_{\text{cool}}^{\text{CGM}} \approx 1.9 \times 10^{11} M_{\odot} (R_{\perp}/160 \text{ kpc})^2$. This accounts for $1/3$ of the total expected baryonic mass.

enriched gas within the QPQ halos is thus required to complete the baryonic mass budget. Such warm/hot intracluster medium is predicted to be already fully in place at $z \sim 2$ in massive halos (e.g. Fumagalli et al. 2014).

4.4. Volume Density and Linear Size of The Absorbers

From our analysis, there are two standard methods for assessing the volume density n_{H} of the gas and, in turn, offering an assessment of the linear scale ℓ of the absorption system. One approach is to assume an intensity for the incident radiation field intensity J_{ν} and then convert the estimated ionization parameter U into an estimate of n_{H} . The uncertainties in this analysis are large: we have no direct constraint on J_{ν} , the error in U is substantial, and systematic uncertainties in the photoionization modeling influence this treatment. Therefore, we proceed in a conservative fashion.

For J_{ν} , we consider two limits: (1) the gas is illuminated by only the EUVB, where we adopt the spectral energy distribution of the cosmic ultraviolet background normalized to the Faucher-Giguère et al. (2008) estimate for the effective IGM Ly α opacity; (2) the gas is fully illuminated by the foreground quasar which shines isotropically and the gas is at a distance r equal to the impact parameter R_{\perp} . The first limit sets a lower bound to J_{ν} and therefore the density while the latter sets an upper limit to n_{H} . For the EUVB case, we would require $n_{\text{H}} \approx 10^{-3} \text{ cm}^{-3}$. This is a somewhat low value for over-dense and optically thick gas, but is comparable to predictions from simulations (Rosdahl & Blaizot 2012). A Ly α fluorescence analysis (Arrighi Battaia et al. 2016) suggests $n_{\text{H}} \approx 0.6 \times 10^{-2} \text{ cm}^{-3}$, which is not that far from our result given the uncertainties. Furthermore, the resultant length scale $\ell \equiv N_{\text{H}}/n_{\text{H}}$ would exceed 100 kpc per cloud for the typical $N_{\text{H}}^{\text{QPQ8}} \approx 10^{20.5} \text{ cm}^{-2}$. Although not strictly ruled out for the majority of our sample (see

below), we suspect the densities are significantly higher and that ℓ is correspondingly smaller. If the quasar emits isotropically and $r \approx R_\perp$, then the implied densities are $n_{\text{H}} \approx 1 - 10 \text{ cm}^{-3}$. Such values are characteristic of the diffuse interstellar medium of galaxies. In this extreme, we recover $\ell \approx 1 - 10 \text{ pc}$, which has been previously reported for some absorption systems (Sargent et al. 1979; Simcoe et al. 2006) and yet may be considered extreme. In another study, metal enriched gas clumps in the circumgalactic medium at $z \sim 2.5$ are found to have sizes 100–500 pc (Crighton et al. 2015).

An independent assessment of the density may be obtained from analysis of the fine structure absorption of C^+ and Si^+ (e.g. Prochaska 1999; Silva & Viegas 2002, QPQ3). Under the assumption that electron collisions dominate the excitation of these ions in our photoionized gas, the ratio of the excited state to the ground state yields a precise estimate for n_e . We have previously assessed in QPQ3 whether the gas could be excited indirectly by UV pumping (e.g. Prochaska et al. 2006), and find the quasars are too faint. From the QPQ8 dataset, we report two positive detections and several upper limits of $\text{C II}^* 1335$ absorption. Following the methodology in QPQ3, we assumed an electron gas temperature of 20000 K and obtained $n_e = \frac{106}{2(N(\text{C}_{J=1/2}^+)/N(\text{C}_{J=3/2}^+)) - 1}$,

where $J = 1/2$ represents the ground state and $J = 3/2$ is the first excited level. In Table 5 we present the resultant n_e estimates and the corresponding linear size per cloud $\ell = N_{\text{H}}/n_{\text{H}}$, where $n_{\text{H}} = n_e/(1 - x_{\text{HI}})$, not compensating for ionized helium contribution to electron density. For the positive detections, we find $n_e > 10 \text{ cm}^{-3}$. For subsystem F of J1420+1603FG, n_e even exceeds the electron density expected for isotropic quasar illumination n_{QSO} (Section 3.3), suggestive of local sources of radiation.

4.5. Peculiarities of the Quasar Circumgalactic Medium

The environments of $z \sim 2$ quasars must be considered extreme compared with co-eval Lyman break galaxies, at least in terms of overdensity and possibly an elevated, local radiation field. In this respect, the high metallicities, large CGM gas masses, and complex kinematics may follow naturally. As such, we are further motivated to search for peculiar features in the absorption line data that occur rarely, if at all, along random sightlines. We now summarize a series of examples which on their own are remarkable and together paint a highly unusual picture of the $z \sim 2$ universe.

4.5.1. Evidence for Elevated Radiation Field

The most extreme case, in our opinion, is the putative $\text{Ly}\alpha$ emission in subsystem A of J1427-0121FG. As shown in the Appendix, the positive flux at $\text{Ly}\alpha$ suggests $N_{\text{HI}} < 10^{14} \text{ cm}^{-2}$ whereas the positive detections of low ions and the high opacities at $\text{Ly}\beta$ and $\text{Ly}\gamma$ indicate $N_{\text{HI}} \gg 10^{14} \text{ cm}^{-2}$. Although metal bearing systems with $N_{\text{HI}} \sim 10^{14} \text{ cm}^{-2}$ have been reported previously (e.g. Boksenberg & Sargent 2014), these are very rare and generally dominated by C IV and O VI absorption (Simcoe et al. 2004). We strongly suspect that the flux at $\text{Ly}\alpha$ is unresolved $\text{Ly}\alpha$ emission as predicted for gas illuminated by the ionizing flux of a nearby quasar (e.g. Cantalupo et al. 2014; Hennawi & Prochaska 2013; Hen-

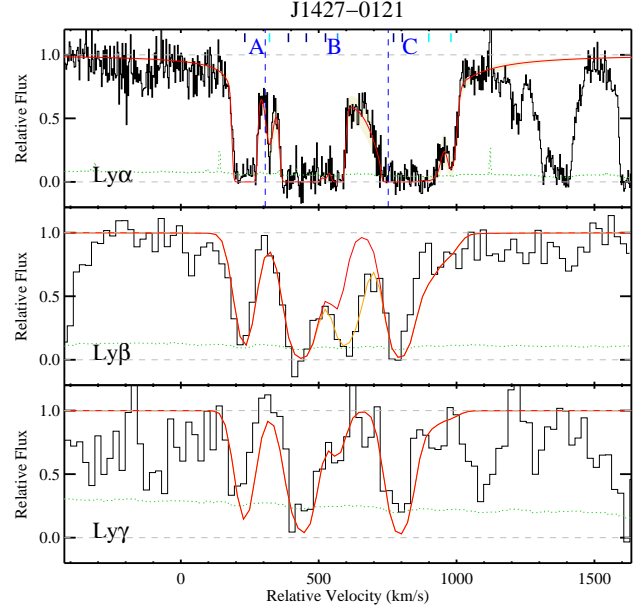


FIG. 17.— H I Lyman series absorption profiles for J1427-0121. The black histograms show the Lyman series identified in the J1427-0121BG spectrum at velocities consistent with J1427-0121FG. The navy ticks mark the centroid redshifts for H I components traced by low metal ions. The cyan ticks mark H I components not associated with metal ions. The red curve is the Voigt profile modeling fit of summing up all H I components associated with J1427-0121FG. The orange curve is the modeling fit including $\text{Ly}\alpha$ forest contamination. The positive flux at $\text{Ly}\alpha$ suggests $N_{\text{HI}} < 10^{14} \text{ cm}^{-2}$ whereas the positive detections of low ions and the high opacities at $\text{Ly}\beta$ and $\text{Ly}\gamma$ indicate $N_{\text{HI}} \gg 10^{14} \text{ cm}^{-2}$. We suspect the flux at $\text{Ly}\alpha$ is unresolved $\text{Ly}\alpha$ emission as predicted for gas illuminated by the ionizing flux of a nearby quasar. The green histogram presents the 1σ noise in the normalized flux.

nawi et al. 2015). In Figure 5 of QPQ4, we showed the PSF subtracted Gemini spectrum of the J1427-0121 pair and there is no revealing residual $\text{Ly}\alpha$ emission to sensitivity limit $\text{SB}_{1\sigma} = 0.14 \times 10^{-17} \text{ erg s}^{-1} \text{ cm}^{-2} \text{ arcsec}^{-2}$. Thus this emission is spatially unresolved, i.e. it is consistent with the point spread function of the foreground quasar. This phenomenon, however, is rare in our quasar pair sample (QPQ4) and we identify no other example in the 8 cases from QPQ8 where we have coverage of $\text{Ly}\beta$ or higher order Lyman series lines.

To estimate the $\text{Ly}\alpha$ flux more accurately we prefer a lower dispersion spectrum than our echelle/echellette resolution follow-up spectra. Based on the SDSS spectrum continuum, we estimated the $\text{Ly}\alpha$ flux $F_{\text{Ly}\alpha} = 1.5 \times 10^{-17} \text{ erg s}^{-1} \text{ cm}^{-2}$. Since the size of the emitting cloud has to be smaller than typical seeing disk of $1''$, the $\text{Ly}\alpha$ surface brightness $\text{SB}_{\text{Ly}\alpha} > 1.5 \times 10^{-17} \text{ erg s}^{-1} \text{ cm}^{-2} \text{ arcsec}^{-2}$. If the absorber is optically thin, we may estimate the surface brightness of subsystem A following the formalism of QPQ4. Specifically, we assumed a volume density that is the same as that of subsystem C, which is calculated to be $n_{\text{H}} = 16 \text{ cm}^{-3}$ from the $N_{\text{CII}}/N_{\text{CII}^*}$ ratio. We adopted the N_{H} value from photoionization modeling. The expected $\text{SB}_{\text{Ly}\alpha} \approx 3.3 \times 10^{-17} \text{ erg s}^{-1} \text{ cm}^{-2} \text{ arcsec}^{-2}$. If the absorber is optically thick, the formalism of QPQ4 then gives $\text{SB}_{\text{Ly}\alpha} \approx 9.5 \times 10^{-17} \text{ erg s}^{-1} \text{ cm}^{-2} \text{ arcsec}^{-2}$. Since the measured $\text{Ly}\alpha$ flux corresponds to lower $\text{Ly}\alpha$ surface brightness, the characteristic angular size of the ab-

sorber should be smaller than the typical seeing disk $1''$, corresponding to < 8 kpc. Furthermore, again following the formalism of QPQ4, should this absorber be optically thin, this level of Ly α fluorescence would imply $N_{\text{HI}} = 1.1 \times 10^{17} \text{ cm}^{-2}$, and hence the optically thin assumption breaks down. The absorber probably lies in the transition from the optically thin to the optically thick limit. Alternatively, Ly α emission can result from collisional excitation. In the absence of significant metal enrichment, collisionally excited Ly α emission is the primary coolant for $T \sim 10^4$ K gas. Collisional excitation of neutral hydrogen requires a non-negligible neutral fraction, and the resulted surface brightness is exponentially sensitive to gas temperature via the collisional excitation rate coefficient $q_{1s \rightarrow 2p}(T)$. Thus the electron density estimated will be uncertain by orders of magnitude. However, we expect recombination dominates cooling radiation. Hennawi et al. (2015) reports the Ly α emission from collisional excitation is at most 20% of the Ly α emission from recombination, for the nebula illuminated by a quasar quartet discovered by them.

In previous works (QPQ2, QPQ4, QPQ6), we have argued that quasars emit anisotropically owing to the high incidence of optically thick, cool gas in the transverse direction relative to that observed along the direct sightline. With the high fidelity of our QPQ8 sample, we may search for more subtle signatures that at least a portion of the transverse sightline is illuminated by a luminous and hard radiation field. One such signature would be the N V doublet $\lambda\lambda$ 1238, 1242, which may also trace a distinct warm-hot phase. With an ionization potential of 5.5 Ryd, production of the N^{4+} ion requires a gas with $T \gtrsim 10^5$ K for collisional ionization or a high intensity of extreme UV photons. Indeed, N V is very rarely detected in random, intervening systems along quasar sightlines (Fox et al. 2009) or even in the CGM of Lyman break galaxies (Turner et al. 2014), but is more frequently detected in gas associated to the quasar itself. For each pair in the QPQ8 sample, we have coverage of the N V doublet but these lines are free of the Ly α forest in only 3 cases. Of these, we report one positive detection (J1026+4614). Our photoionization model for this gas yields $\log U \approx -1.9$ dex (see the Appendix). To achieve this U value with the EUVB, one would require a very low gas density $n_{\text{H}} \approx 10^{-4} \text{ cm}^{-3}$ and an absorber size $\ell = N_{\text{H}}/n_{\text{H}} \approx 13$ kpc. Given the rarity of N V detections along random quasar sightlines, we contend this gas is illuminated by the foreground quasar, although the flux need not be as bright as the observed along our sightline, or the flux may also exhibit temporal variability. The absence of N V in the other 2 pairs with coverage outside the Ly α forest and the 4 cases with minimal IGM blending suggests that only small portions of the transverse sightlines are illuminated. This conclusion is tempered by the possible underabundance of N but large deviations from solar relative abundances tend to occur in gas with metallicities much lower than those estimated for this CGM (e.g. Henry et al. 2000). Taking the median values of $[\text{M}/\text{H}] = -0.6$ and $N_{\text{H}} = 10^{20.5} \text{ cm}^{-2}$, using Cloudy we estimated for the QPQ8 systems $N_{\text{NV}} = 10^{9.3} - 10^{14.7} \text{ cm}^{-2}$, varying $\log U$ from -4 to -2 . Hence only for high values of U parameter will N V become strong enough to detect in most

of our echellette resolution data, whose detection limit is on average $N_{\text{HV}} < 10^{13.6} \text{ cm}^{-2}$. Another doublet that may trace a quasar illuminated gas or a distinct warm-hot phase is the O VI doublet $\lambda\lambda$ 1031, 1037. However, in the QPQ8 data we are unable to resolve this doublet from coincident absorption in the Ly α forest.

The subsystem F of J1144+0959FG exhibits significant low ion absorption, e.g. O I and Fe II, and has an estimated $N_{\text{HI}} \approx 10^{18} \text{ cm}^{-2}$. These properties characterize optically thick, partially ionized Lyman limit system. The very strong medium and high ions, however, yield an ionization parameter $\log U \approx -2$, giving a neutral fraction of $x_{\text{HI}} \approx 10^{-3}$ and a total $N_{\text{H}} \approx 10^{21} \text{ cm}^{-2}$. If the volume density is close to the rough upper bound $n_{\text{QSO}} = 10^{-0.3} \text{ cm}^{-3}$, together these suggest an elevated radiation field.

Given the rarity of such phenomena along random quasar sightlines, we may hypothesize that where one observes similar cases an AGN may be present or recently was shining (Oppenheimer & Schaye 2013). In this study, evidence for an elevated radiation field is found for only 2 out of 14 quasar environments studied. We do not believe that the quasar CGM is qualitatively peculiar relative to other massive galaxies, however to date QPQ is the only statistical sample to characterize the physical properties of the CGM of massive galaxies at $z \sim 2$. For the typical bolometric luminosities of these quasars, observations imply star formation rates comparable to inactive star forming galaxies of similar masses (e.g. Rosario et al. 2013).

Farina et al. (2013) studied a mass-controlled sample and found that, if the mass of the galaxies is taken into account as an additional parameter that influences the extent of the gaseous halos, the distribution of Mg II absorbers around quasars is consistent with that for normal galaxies.

4.5.2. Evidence for Elevated Volume Density

In Section 4.4, we assessed the density of the gas through analysis of C II* 1335 absorption and reported two positive detections. Among these, subsystem F of J1420+1603FG has a C II* 1335 optical depth exceeding 0.8 at its peak and an excited to ground state ratio of ≈ 1.1 . To our knowledge, this exceeds any such measurement along an extragalactic sightline including GRBs (Prochaska et al. 2006), whose gas is radiatively excited. In turn, this requires an electron density $n_{\text{e}} = 10^{2.2} \text{ cm}^{-3}$ which defies conventional wisdom for diffuse CGM gas (Werk et al. 2014). Similar inferences, however, have been drawn from the Ly α nebulae surrounding $z \sim 2$ quasars (Cantalupo et al. 2014; Hennawi et al. 2015; Arrigoni Battaia et al. 2015a,b) and the extended narrow emission line regions and nebulae of other AGNs and radio galaxies (Humphrey et al. 2007; Dey et al. 2005; Stockton et al. 2002; Fu & Stockton 2007). Given that the inferred absorption pathlength is $\ell \lesssim 1$ pc, one must invoke a large population of such clouds to explain our intersecting even one given $(\ell/R_{\perp})^2 < 10^{-10}$. Furthermore, small and dense clumps will be disrupted by hydrodynamic instabilities as they move through a hotter CGM phase, unless the hot plasma pressure is able to confine the compact clumps (Arrigoni Battaia et al. 2015a; Crighton et al. 2015). Furthermore, such a small cloud is representative of the dense knots inside

giant molecular clouds. However, the absence of Lyman-Werner bands implies $N_{\text{H}_2} < 10^{18} \text{ cm}^{-2}$.

5. SUMMARY AND FUTURE OUTLOOK

In the “Quasars Probing Quasars” series of papers, we have introduced a novel technique to study the CGM surrounding quasar host galaxies, which provides clues to the physics of massive galaxy formation and the nature of quasar feedback. We mined the existing quasar catalogs for closely projected, physically unassociated quasar pairs and confirmed them with follow up spectroscopy. From a total of ≈ 700 confirmed pairs, we selected 14 pairs with projected separations < 300 kpc and high dispersion, high S/N data, to study the CGM surrounding quasars at $z \sim 2-3$. We analyzed the velocity fields of the absorbing gas, the H I and metal ion column densities and the ionization state characterized by the ionization parameter U . These analyses constrain the physical state of the cool gas near the foreground quasars, including its kinematics, chemical abundance patterns, surface density profiles, volume density, size of the absorbers and the intensity of the impinging radiation field, as well as to test for the presence of a hotter phase of CGM. Our key findings are as follows.

Model-Independent Constraints:

- The low (e.g. C II) and high (e.g. C IV) ions roughly trace each other in velocity structure. The velocity widths exceed all previous measurements of gas surrounding any galaxy populations, with a RMS $\sigma_v = 495 \text{ km s}^{-1}$ for C IV and $\sigma_v = 249 \text{ km s}^{-1}$ for C II. The velocity centroids of the absorption profiles are frequently biased to positive (redshifted) velocities from the systemic redshift of the foreground quasars.
- The H I and low metal ion (traced by C II) surface density declines with R_\perp . H I absorption is strong even beyond the estimated virial radius. The H I column densities are significantly larger than those of co-eval galaxies.
- In one case, subsystem A of J1427-0121FG, we suspect the presence of unresolved Ly α emission, a prediction for gas illuminated by the foreground quasar. In another case, J1026+4614, we detected N V absorption and we contend the gas is at least partially illuminated by the foreground quasar. The non-detection of N V in all other absorption systems, however, suggests that only small portions of the transverse sightlines are illuminated and the flux needs not be as high as along the line of sight.

Model-Dependent Constraints:

- The ionization parameter U positively correlates with projected distance from the foreground quasar. This runs contrary to expectation should the foreground quasar dominate the ionizing radiation field.
- The CGM is significantly enriched even beyond the estimated virial radius of the host dark matter halos (≈ 160 kpc). Within $R_\perp \approx 200$ kpc, the median metallicity is $[\text{M}/\text{H}] = -0.6$ dex.

- The O/Fe ratio is supersolar in nearly all measurements. A significant fraction of the CGM must have an enhanced α/Fe abundance, suggestive of a star formation history similar to massive ellipticals with a short starburst duration.
- We did not find any evolution in the total H column up to $R_\perp \approx 200$ kpc, consistent with the finding that both the H I column and the neutral gas fraction decline with R_\perp . The median total H column is $N_{\text{H}} \approx 10^{20.5} \text{ cm}^{-2}$.
- Within the estimated virial radius, we found the total mass of the cool phase CGM is substantial: $M_{\text{cool}}^{\text{CGM}} \approx 1.5 \times 10^{11} M_\odot (R_\perp/160 \text{ kpc})^2$. This accounts for 1/3 of the dark halo baryonic budget.
- For 2 absorption subsystems with positive detection of the C II* fine structure line, we estimated the electron volume density and the corresponding linear size per cloud, and found $n_e > 10 \text{ cm}^{-3}$. In one case, subsystem F of J1420+1603FG, the C II* to C II column ratio exceeds any previous measurement along extragalactic sightlines. The implied $n_e = 10^{2.2} \text{ cm}^{-3}$ even defies conventional wisdom that the CGM is primarily diffuse.

Below we list several directions of future inquiry.

- Assemble a larger sample of quasar pairs with precise redshift measurements to better quantify any anisotropy in the velocity fields of metal ions on CGM scale (QPQ9), and H I on larger scales (Henawi et al. in prep.).
- Model the transverse proximity effect out to large scales to determine the average opening angle or variability timescale of the quasar radiation, which would help in the interpretation of the CGM measurements, in particular how often these CGM absorbers are expected to be illuminated.
- Cosmological galaxy formation simulations that include feedback from AGN and/or star-formation powered winds to determine whether they can reproduce the observed cool and often optically thick quasar CGM.
- Use projected submillimeter galaxy-quasar pairs to study the CGM surrounding submillimeter galaxies, whose clustering strength is comparable to quasars. This will help isolate the impact of quasar feedback on the CGM.
- Narrow band (Cantalupo et al. 2014) and integral field (Martin et al. 2014) imaging of the CGM.

We thank the anonymous referee for a careful review and help in consolidating the findings. JXP and MWL acknowledge support from the National Science Foundation (NSF) grant AST-1010004, AST-1109452, AST-1109447 and AST-1412981. We acknowledge the contributions of Sara Ellison, Crystal Martin, and George Djorgovski in obtaining the ESI spectra. We thank Ryan

Cooke for his software ALIS and technical support. We thank Guillermo Barro for technical support for MOS-FIRE data reduction. We thank George Becker for helpful advices on XSHOOTER data reduction. We thank Camille Leibler for comments on chemical enrichment patterns. We thank Justin Brown for comments on supernova nucleosynthesis yields. We thank John O'Meara for sharing his metal enriched IGM absorption data. We thank Emanuele P. Farina for examining the manuscript. MWL thanks Sprite Chu for professional computing support.

Much of the data presented herein were obtained at the W. M. Keck Observatory, which is operated as a scientific partnership among the California Institute of Technology, the University of California, and the National Aeronautics and Space Administration. The Observatory was made possible by the generous financial support of the W. M. Keck Foundation.

Some of the data herein were obtained at the Gemini Observatory, which is operated by the Association of Uni-

versities for Research in Astronomy, Inc., under a cooperative agreement with the NSF on behalf of the Gemini partnership: the NSF (United States), the Science and Technology Facilities Council (United Kingdom), the National Research Council (Canada), CONICYT (Chile), the Australian Research Council (Australia), Ministério da Ciência, Tecnologia e Inovação (Brazil) and Ministerio de Ciencia, Tecnología e Innovación Productiva (Argentina).

The authors wish to recognize and acknowledge the very significant cultural role and reverence that the summit of Mauna Kea has always had within the indigenous Hawaiian community. We are most fortunate to have the opportunity to conduct observations from this mountain.

Some of the data were obtained with the 6.5 meter Magellan Telescopes located at Las Campanas Observatory, Chile.

Some of the data were obtained with the European Southern Observatory Very Large Telescope under program ID 087.A-0610(A).

APPENDIX

TREATMENT OF C IV IN KINEMATIC ANALYSIS

For C IV 1548, we required a special treatment for the absorption systems where the velocity width exceeds the doublet separation $c\Delta\lambda/\lambda \approx 500 \text{ km s}^{-1}$. In these cases the optical depth profiles overlap and we made the following modifications to estimate Δv_{90} and $\bar{\delta}v$. Specifically we examined the optical depth profile of the entire doublet and boosted the opacity by 1.5 in the region of overlap and by 2 at velocities where only absorption by C IV 1550 is present. These factors account for the 2:1 ratio in the oscillator strengths of the two transitions. We then calculated Δv_{90} and $\bar{\delta}v$ from the optical depth profile of the full doublet and offset the derived quantities by the doublet separation.

ROBUSTNESS OF COLUMN DENSITY MEASUREMENTS

We examined the effect of saturated narrow features appearing unsaturated in low-resolution spectra, which would result in underestimated ion column densities. The paper conservatively reports lower limits for cases where the normalized flux goes below 0.4. In this paper we use echelle spectra to analyze the metal absorption subsystems of J1144+0959, J1204+0221, and J1427-0121. We have obtained echellette spectra of them using MagE. Figure 18 plots the column densities of the metal absorption subsystems measured from echellette spectra versus echelle spectra, where the normalized flux is greater than 0.4 in the echellette spectra. The data points include all metal ions such as C⁺, C³⁺, O⁰, etc and do not differentiate them. For an ion species where multiple transitions are available for measurement, the column density reported is the mean of the measurements weighted by inverse variance. The data points in Figure 18 are color coded to indicate those with more than one transition analyzed. We do not see any systematic bias in measurement using strong versus weak lines.

The data points show an increased scatter with decreasing column density. This is what we would expect intuitively, as the relative error in weaker absorption is larger. The linear best fit is very close to the $y = x$ line, and there is only one data point that deviates more than $3\text{-}\sigma$ from the $y = x$ line. If we force the linear best fit to pass through the origin, which would be the case were S/N infinite, then the slope equals 1.00. Figure 18 shows both data points that lie above and below the $y = x$ line. The overall mean agreement demonstrates our criterion on the minimum normalized flux for reporting lower limits well captures saturated components. Moreover, there is also no evidence of systematic bias to higher column density measurements from echellette spectra that may originate from contamination from neighboring absorption features that is unresolved.

We also fitted Voigt profiles to unsaturated metal absorption components to the echelle spectrum of J1427-0121, and summed the total column densities in each subsystem. Our aim was only to verify that Voigt profile fitting and AODM give the same column densities. For the χ^2 minimization process, we set the Doppler b values to be 5 km s^{-1} minimum as set by resolution limit, although the model preferred lower values for a few components. Conventionally, due to turbulence the minimum b value is 8 km s^{-1} , and contributions from turbulence dominates over thermal broadening. This is just as expected for an instrumental resolution high enough to resolve the lines.

We have defined absorption subsystems as those separated in distinct velocity intervals, with no obvious ionization gradient within. The three echelle sightlines also allow us to examine any remaining ionization gradient within a subsystem. We considered the J1427-0121 sightline. We performed a component-by-component photoionization modeling for its subsystem C, and omitted its subsystems A and B for that analysis. There is residual Ly α emission at the absorption trough of subsystem A, which makes it difficult to deblend the two absorption components in H I at velocities defined by the metal ions. The three components of subsystem B which contain low ions are all weak absorption, which makes it difficult to analyze them separately. Subsystem C contains two components and we found $\log U < -3.6$ and $\log U < -3.4$ respectively. In the ionization modeling treatment in this study, we adopted

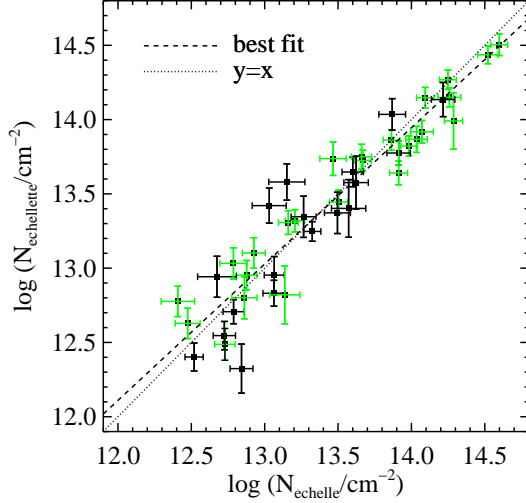


FIG. 18.— Column densities of ions of the subsystems of J1144+0959, J1204+0221, and J1427-0121, measured from echellette spectra versus echelle spectra, where the normalized flux is greater than 0.4 in the echellette spectra. Error bars colored in green indicate multiple transitions of the same species is available for measurement. The plot shows that our criterion of normalized flux going below 0.4 for reporting lower limits well captures saturated components.

log $U < -3.4^{+0.3}$ for subsystem C. We conclude that measuring column densities using AODM is robust to within the uncertainties allowed for ionization modeling-dependent analysis.

NOTES ON INDIVIDUAL PAIRS

We present a detailed description, including figures and tables, for the absorption associated to each of the foreground quasars in the QPQ8 sample. See Section 3 for a description of the techniques employed in the analysis. In Table 21, we present the H I column density measurements of each absorption subsystem.

J0225+0048— Figure 19 reveals absorption for this pair in roughly three distinct velocity intervals spanning a total of $\Delta v \approx 1000 \text{ km s}^{-1}$. We define three subsystems based on the strong features in the H I Lyman series absorption. We present the ionic column densities measured with the apparent optical depth method in Table 7. Absorption from high ions Si^{3+} and C^{3+} is strong in subsystems A and B and moderate in subsystem C. No low ion transitions are detected for any of the subsystems, indicating a highly ionized gas. Regarding the N_{HI} analysis, we have limited constraints given that the echellette resolution data only covers the $\text{Ly}\alpha$ transition. There is no indication of damping wings and the lines are saturated, i.e. on the flat portion of the curve of growth. We also present the lower dispersion GMOS spectrum that covers $\text{Ly}\beta$. The gas shows absorption separated in roughly three distinct velocity intervals. If we assume minimum Doppler $b_{\text{A,B,C}}$ values of 15 km s^{-1} , the lack of strong damping wings in all three subsystems yields strict upper limits of $N_{\text{HI}}^{\text{A}} < 10^{18.6} \text{ cm}^{-2}$, $N_{\text{HI}}^{\text{B}} < 10^{18.7} \text{ cm}^{-2}$ and $N_{\text{HI}}^{\text{C}} < 10^{18.5} \text{ cm}^{-2}$. If we assume maximum Doppler $b_{\text{A,B,C}}$ values of 60 km s^{-1} and single components, the equivalent widths demand $N_{\text{HI}}^{\text{A}} > 10^{15.6} \text{ cm}^{-2}$, $N_{\text{HI}}^{\text{B}} > 10^{16.1} \text{ cm}^{-2}$ and $N_{\text{HI}}^{\text{C}} > 10^{16.0} \text{ cm}^{-2}$. We fitted these data with the ALIS software package assuming 7 components (see Table 21), with redshifts set by the metal line absorption. We find solutions with nearly equivalent χ^2 that range from $N_{\text{HI}} = 10^{16.4} \text{ cm}^{-2}$ to $10^{18.9} \text{ cm}^{-2}$. We adopted approximately the central N_{HI} values in this range and a correspondingly large uncertainty for each subsystem. Because no low ion states are detected, the ionic ratios $\text{Si}^+/\text{Si}^{3+}$ and C^+/C^{3+} impose lower limits on U . Our ionization modeling yields $\log U_{\text{A}} > -2.4$, $\log U_{\text{B}} > -2.3$, and $\log U_{\text{C}} > -2.6$. To further constrain U we also considered the $\text{Si}^{3+}/\text{C}^{3+}$ ratios. They imply yet higher U values, provided the relative abundances are roughly solar. These U values suggest either the radiation field is much stronger than the EUVB and the foreground quasar is shining on the gas, or that $n_{\text{H}} \ll 0.1 \text{ cm}^{-3}$.

J0341+0000— Within $\pm 1000 \text{ km s}^{-1}$ of z_{fg} we identify no system with a rest equivalent width for $\text{Ly}\alpha$ exceeding 0.3 \AA . We present AODM measurements of the upper limits to any associated metal ion columns in Table 8. Associating the strongest absorption line to the quasar at $z = 2.1286$ (Figure 20), we measured $N_{\text{HI}} = 10^{14.2 \pm 0.2} \text{ cm}^{-2}$ from a fit to the data. Although there is uncertainty dominated by possible line saturation, we strictly constrain $N_{\text{HI}} < 10^{14.4} \text{ cm}^{-2}$ assuming $b > 15 \text{ km s}^{-1}$.

With the absence of metal line detections, we have no constraints on the ionization state of the gas. The low N_{HI} column, however, implies a highly ionized medium. Together the data suggests either an extreme ionization state, low metallicity, or little gas along the sightline.

J0409-0411— Similar to J0341+0000, this system shows no $\text{Ly}\alpha$ line with a peak optical depth greater than 2 within 1000 km s^{-1} of z_{fg} (Figure 21). We present AODM measurements of the upper limits to any associated metal ion columns in Table 9. The strongest $\text{Ly}\alpha$ line at $z = 1.7027$ has an equivalent width $W_{\text{Ly}\alpha} = 0.45 \pm 0.04 \text{ \AA}$. A line profile analysis gives $N_{\text{HI}} = 10^{14.2 \pm 0.2} \text{ cm}^{-2}$ for the complex with the uncertainty dominated by possible line saturation.

With the absence of metal line detections, we have no constraints on the ionization state of the gas. The low

N_{HI} column, however, implies a highly ionized medium.

J0853-0011— The ions show absorption in roughly three distinct velocity intervals spanning a total of $\Delta v \approx 650 \text{ km s}^{-1}$ (Figure 22). We define three subsystems across the complex. We present the ionic column densities measured with AODM in Table 10. One notes moderate absorption in subsystem A and strong absorption in subsystems B and C from a series of low ions, including O^0 , Si^+ , C^+ , Fe^+ and Al^+ . Subsystems B and C are characteristic of Lyman limit systems where the large H I opacity self shields gas from local or background UV sources (e.g. Prochaska et al. 2015). Elements therefore occupy the first ionization state with an ionization potential greater than 1 Ryd. Furthermore, there is only weak Si IV and C IV absorption. Altogether the data suggests an optically thick gas.

The $\text{Ly}\beta$, $\text{Ly}\gamma$ and $\text{Ly}\delta$ profiles show absorptions in three distinct velocity intervals corresponding to the three subsystems. The absence of strong damping wings in the the $\text{Ly}\alpha$ absorption profiles demand $N_{\text{HI}}^{\text{A}} < 10^{18.0} \text{ cm}^{-2}$, $N_{\text{HI}}^{\text{B}} < 10^{18.8} \text{ cm}^{-2}$ and $N_{\text{HI}}^{\text{C}} < 10^{18.4} \text{ cm}^{-2}$. Assuming maximum $b_{\text{A,B,C}}$ -values of 60 km s^{-1} and absorption dominated by single components, as implied by the H I and metal line profiles, the measured equivalent widths imply $N_{\text{HI}}^{\text{A}} > 10^{14.8} \text{ cm}^{-2}$, $N_{\text{HI}}^{\text{B}} > 10^{16.0} \text{ cm}^{-2}$ and $N_{\text{HI}}^{\text{C}} > 10^{15.2} \text{ cm}^{-2}$. The asymmetric $\text{Ly}\alpha$ absorption profile of subsystem B implies modest blending with a weak H I component. The $\text{Ly}\gamma$ profile is blended with an unrelated H I component of $N_{\text{HI}} \approx 10^{14.8} \text{ cm}^{-2}$ at $z \approx 1.7211$. We adopt $N_{\text{HI}}^{\text{A}} = 10^{16.8 \pm 0.6} \text{ cm}^{-2}$, $N_{\text{HI}}^{\text{B}} = 10^{18.6^{+0.2}_{-0.6}} \text{ cm}^{-2}$ and $N_{\text{HI}}^{\text{C}} = 10^{18.2^{+0.3}_{-0.6}} \text{ cm}^{-2}$, where the error in N_{HI} is dominated by $\text{Ly}\alpha$ forest contamination and line saturation.

Multiple ionization states of the same element $\text{Fe}^+/\text{Fe}^{2+}$, $\text{Si}^+/\text{Si}^{3+}$, $\text{Al}^+/\text{Al}^{2+}$ and C^+/C^{3+} provide observational constraints on U . The gas shows systematically stronger low ion absorption and correspondingly lower U values, $\log U < -3$, than the majority of the QPQ8 sample. We adopt $\log U_{\text{A}} = -3.2$, $\log U_{\text{B}} = -3.4$ and $\log U_{\text{C}} = -3.1$ giving $x_{\text{HI,A}} = 0.01$, $x_{\text{HI,B}} = 0.08$ and $x_{\text{HI,C}} = 0.02$ and $N_{\text{H}}^{\text{A}} = 10^{18.9} \text{ cm}^{-2}$, $N_{\text{H}}^{\text{B}} = 10^{19.7} \text{ cm}^{-2}$ and $N_{\text{H}}^{\text{C}} = 10^{20.0} \text{ cm}^{-2}$.

J0932+0925— The ions show absorption in roughly three distinct velocity intervals spanning a total of $\Delta v \approx 1200 \text{ km s}^{-1}$ (Figure 23) that demarcate three subsystems. We present the ionic column densities measured with AODM in Table 11. One notes strong C IV absorption in subsystem B and moderate C IV absorption in subsystems A and C. C II absorption is weak in subsystem A and absent in subsystems B and C. The intermediate ion Si III 1206 transition locates in a relatively clean region of the $\text{Ly}\alpha$ forest. Qualitatively the data indicates a highly ionized gas.

Only the $\text{Ly}\alpha$ and the $\text{Ly}\beta$ absorption profiles have sufficient S/N for analysis. The stronger absorption features of subsystems A and B are well constrained by both the $\text{Ly}\alpha$ and the $\text{Ly}\beta$ profiles. Subsystem C and the weaker components of subsystems A and B which have their $\text{Ly}\beta$ profiles blended with $\text{Ly}\alpha$ forest lines, all have N_{HI} values on the linear part of the curve of growth. For the strongest component in subsystem A, the measured equivalent width constrains $10^{14.5} \text{ cm}^{-2} < N_{\text{HI}}^{\text{A}} < 10^{17.5} \text{ cm}^{-2}$ assuming b_{A} ranges between $15\text{--}60 \text{ km s}^{-1}$. The strongest absorption feature of subsystem B is asymmetric in $\text{Ly}\alpha$ and $\text{Ly}\beta$, suggesting that it contains two H I components, as modeled. Our best fit solution gives a total $N_{\text{HI}}^{\text{B}} = 10^{15.1^{+0.3}_{-0.3}} \text{ cm}^{-2}$, where the errors are dominated by uncertainty in continuum placement and $\text{Ly}\alpha$ forest line blending. The N_{HI} values for subsystem C are well constrained by the unsaturated $\text{Ly}\alpha$ profile.

This system has Si^{2+} and Si^{3+} detections which constrain the U value for the three subsystems. These are also consistent with the constraints derived from C^+/C^{3+} .

J1026+4614— The ions show absorption in two velocity intervals spanning a total of $\Delta v \approx 240 \text{ km s}^{-1}$ (Figure 24). We present the ionic column densities in Table 12. This is the only member of the QPQ8 sample with strong absorption from the N V doublet, although we also note that it is also one of the few where those transitions lie outside the $\text{Ly}\alpha$ forest. Together with the lack of low ions, the data suggests the ionization state of the gas is extreme. It is peculiar that in subsystem A the seemingly unsaturated C IV doublet $\lambda\lambda 1548, 1550$ have similar optical depth, i.e. inconsistent with the oscillator strength ratio of 2 to 1. We suspect hidden saturation as there is no evidence for partial covering in the other observed doublets, and treat the C IV 1548 measurement as a lower limit. Figure 24 presents the the $\text{Ly}\alpha$, $\text{Ly}\beta$, $\text{Ly}\gamma$ and $\text{Ly}\delta$ profiles of this absorption system.

All of the components become unsaturated by $\text{Ly}\gamma$ and therefore yield precise measurements for the column densities. The $\text{Ly}\beta$ absorption profile is blended with two $\text{Ly}\alpha$ forest lines of respectively $N_{\text{HI}} \approx 10^{14.7} \text{ cm}^{-2}$ and $N_{\text{HI}} \approx 10^{15.3} \text{ cm}^{-2}$ located at respectively $z \approx 2.6658$ and $z \approx 2.6669$. The $\text{Ly}\gamma$ absorption profile is blended with a $\text{Ly}\alpha$ forest line of $N_{\text{HI}} \approx 10^{14.2} \text{ cm}^{-2}$ at $z \approx 2.4773$. The $\text{Ly}\delta$ absorption profile is blended with a $\text{Ly}\alpha$ forest line of $N_{\text{HI}} \approx 10^{15.8} \text{ cm}^{-2}$ at $z \approx 2.3951$. Modeling these blends together with the Lyman series absorption, we recovered a best-fit solution with $N_{\text{HI}}^{\text{A}} = 10^{15.4 \pm 0.2} \text{ cm}^{-2}$ and $N_{\text{HI}}^{\text{B}} = 10^{14.6 \pm 0.1} \text{ cm}^{-2}$. The errors are dominated by continuum placement at the higher Lyman series lines.

The non-detection of lower ionization states in subsystem A constrain $\log U > -2.3$. If we assume relative solar abundances, the measured $\text{Si}^{3+}/\text{N}^{4+}$ ratio implies $\log U \approx -1.9$. We adopt a larger uncertainty towards higher U values to account for non-solar abundances. Our model for subsystem B, which does not show N V absorption, has a lower U value consistent with the various constraints. We adopt a larger uncertainty to higher U values to allow for an enhanced intrinsic Si/C abundance ratio.

J1038+5027— The ions show absorption spanning a total of $\Delta v \approx 260 \text{ km s}^{-1}$ (Figure 25). We present the ionic column densities in Table 13. There is strong C IV absorption and moderate Si IV absorption, together with weak low ions suggesting a highly ionized gas.

We present the $\text{Ly}\alpha$ profile of this absorption system. The $\text{Ly}\beta$ profile is blended with a strong absorption system is not useful for N_{HI} modeling. The asymmetric $\text{Ly}\alpha$ profile is well modeled by least two H I components, with the weaker one unsaturated at $\text{Ly}\beta$. The lack of obvious damping wings restricts $N_{\text{HI}} < 10^{18.4} \text{ cm}^{-2}$. Assuming a maximum b -

value of 60 km s^{-1} , the $\text{Ly}\alpha$ equivalent width requires $N_{\text{HI}} > 10^{15.3} \text{ cm}^{-2}$. We adopt a total $N_{\text{HI}} = 10^{16.6 \pm 0.5} \text{ cm}^{-2}$, where the large errors are due to line saturation.

The $\text{Si}^+/\text{Si}^{3+}$ and C^+/C^{3+} ratios place lower limits on U . To better constrain the U value, we also consider the $\text{Si}^+/\text{C}^{3+}$ ratio under the assumption of solar relative abundances. Adopting $\log U = -2.2$, we recovered $x_{\text{HI}} = 0.0005$, corresponding to $N_{\text{H}} = 19.9 \text{ cm}^{-2}$.

J1144+0959— This very complex absorption system exhibits a velocity spread of nearly 2000 km s^{-1} (Figure 26), which we divide into six subsystems. We present the ionic column densities in Table 14. Given the large velocity separation of the subsystems, we examined the possibility that some of the gas is unassociated to the foreground quasar. The total equivalent width of C IV 1548 of subsystems A, B, C, and D, $W_{1548} = 0.86 \text{ \AA}$, is large. The C IV survey conducted by Cooksey et al. (2013) reported the incidence of strong C IV absorbers of equivalent width $> 0.6 \text{ \AA}$

at $z \approx 2.97$ to be $\frac{dN_{\text{CIV}}^{>0.6\text{\AA}}}{dz} = 0.83$. Thus in a $\pm 1500 \text{ km s}^{-1}$ window around $z \approx 2.97$, the probability of finding at least one strong C IV absorber is 3%. According to the QSO-C IV clustering analysis in QPQ7 and Vikas et al. (2013), clustering would at most quadruple this probability. We consider it unlikely that subsystems A, B, C, and D are not physically associated to the foreground quasar. We note further that the positive detections of C II 1334 and Al II 1670, which have an even a smaller random incidence, strongly imply the physical association of all the gas to the environment of J1144+0959FG.

Subsystem A shows strong C IV, strong C III absorption in an apparently clean region of the $\text{Ly}\alpha$ forest, and the absence of low ion absorption. Subsystem B shows moderate absorption from C^+ and strong absorption from C^{3+} and Si^{3+} . Subsystem C shows moderate absorption from C^+ and weak absorption from C^{3+} and Si^{3+} . Subsystem D shows moderate absorption from C^+ and moderate absorption from C^{3+} and Si^{3+} . As a group subsystems A, B, C, and D trace a highly ionized gas. Subsystem E shows moderate absorption from high ions C^{3+} and Si^{3+} and no corresponding low ion absorption. Lastly, subsystem F shows strong absorption from high ions C^{3+} and Si^{3+} and strong absorption from low ions O^0 , C^+ , Si^+ , Al^+ and Fe^+ .

We present the $\text{Ly}\alpha$, $\text{Ly}\beta$, and $\text{Ly}\gamma$ velocity profiles of this complex absorption system. The data also cover $\text{Ly}\delta$, but the majority of the complex is blended strongly with a damped $\text{Ly}\alpha$ system with $N_{\text{HI}} \approx 10^{20.3} \text{ cm}^{-2}$ at $z \approx 2.0933$. Two groups of absorbers with associated metal lines separated by $\sim 1000 \text{ km s}^{-1}$ are found in a $\pm 1500 \text{ km s}^{-1}$ window around z_{fg} . Subsystem A has four weak components, among which two are associated with high ion absorption, e.g. C IV, and possibly O VI. Its total $N_{\text{HI}}^{\text{A}} = 10^{13.5 \pm 0.2} \text{ cm}^{-2}$ is well constrained. In the Lyman series, subsystems B and C are blended together, however their centroid velocities can be precisely constrained by the unblended absorption profiles of low ions. the absence of strong $\text{Ly}\alpha$ damping wings demand a total $N_{\text{HI}}^{\text{B+C}} < 10^{18.7} \text{ cm}^{-2}$. Assuming a maximum $b_{\text{B,C}}$ value of 60 km s^{-1} , the large $\text{Ly}\alpha$ equivalent width demands a total $N_{\text{HI}}^{\text{B+C}} > 10^{16.1} \text{ cm}^{-2}$. Our best fit solution gives $N_{\text{HI}}^{\text{B}} = 10^{18.1^{+0.2}_{-0.4}} \text{ cm}^{-2}$ and $N_{\text{HI}}^{\text{C}} = 10^{18.3^{+0.2}_{-0.4}} \text{ cm}^{-2}$, where the errors are dominated by line blending and line saturation. Subsystem D shows multiple components, one associated with ions and three weaker components that lack any metal ion detection. For the stronger component, the lack of strong $\text{Ly}\alpha$ damping wings demand a total $N_{\text{HI}}^{\text{D}} < 10^{19.2} \text{ cm}^{-2}$, while the large $\text{Ly}\alpha$ equivalent width requires $N_{\text{HI}}^{\text{D}} > 10^{15.6} \text{ cm}^{-2}$, assuming $b_{\text{D}} < 60 \text{ km s}^{-1}$. The three weaker components at $v \approx -700 \text{ km s}^{-1}$ have $\text{Ly}\alpha$ and $\text{Ly}\beta$ equivalent widths that lie on the linear part of the curve of growth and hence are tightly constrained. Summing up the four components, our best fit solution gives a total $N_{\text{HI}}^{\text{D}} = 10^{17.9 \pm 0.5} \text{ cm}^{-2}$, where the errors are dominated by line blending and saturation. For subsystem E, the unsaturated Lyman lines yield precise constraint of $N_{\text{HI}}^{\text{E}} = 10^{15.6 \pm 0.2} \text{ cm}^{-2}$. Subsystem F contains two components associated with metal absorption and one component that is not associated with metals. The lack of strong $\text{Ly}\alpha$ damping wings restricts $N_{\text{HI}}^{\text{F}} < 10^{18.5} \text{ cm}^{-2}$, while the large $\text{Ly}\alpha$ equivalent width demands a total $N_{\text{HI}}^{\text{F}} > 10^{16.1} \text{ cm}^{-2}$. Our best fit solution gives a total $N_{\text{HI}}^{\text{F}} = 10^{18.4^{+0.2}_{-0.4}} \text{ cm}^{-2}$, where the errors are dominated by blending in the $\text{Ly}\alpha$, $\text{Ly}\beta$ and $\text{Ly}\gamma$ profiles and line saturation. Altogether, we adopt $N_{\text{HI}}^{\text{total}} = 10^{18.8^{+0.2}_{-0.4}} \text{ cm}^{-2}$ with the upper bound a strict limit given the absence of $\text{Ly}\alpha$ damping wings.

For subsystem A, the C^+/C^{3+} and $\text{C}^{2+}/\text{C}^{3+}$ ratios constrain $-2.2 < \log U_{\text{A}} < -1.5$. We expect the U value to lie closer to the upper value because C III is only mildly saturated and the $\text{Si}^{3+}/\text{C}^{3+}$ ratio is consistent with this estimate. For subsystems B and C, the observed $\text{Si}^+/\text{Si}^{3+}$ ratios put $U_{\text{B,C}}$ at a different values than C^+/C^{3+} does, indicating a multiphase absorber. We give stronger weight to the constraint from $\text{Si}^+/\text{Si}^{3+}$ regarding the lower ionization gas phase. For subsystem D, the observed $\text{Si}^+/\text{Si}^{3+}$ and C^+/C^{3+} ratios well constrain U_{D} . For subsystem E, the observed C^+/C^{3+} ratio gives a precise value for U_{E} that is fully consistent with the observed $\text{Si}^+/\text{Si}^{3+}$ and $\text{Al}^+/\text{Al}^{2+}$ ratios. Subsystem F exhibits positive detections from a wide range of ions. Despite the significant low ion absorption, the measurements imply a highly ionized system. This is argued from the $\text{Si}^+/\text{Si}^{3+}$, $\text{Al}^+/\text{Al}^{2+}$, and C^+/C^{3+} ratios. It is further implied by the very low O^0/Fe^+ ratio, as discussed in Section 4.2. Unfortunately none of these is highly constraining because a number of the measurements are formally lower limits. Adopting the C^+ , C^{3+} , and Si^{3+} values as measurements instead of limits, their measured ratios suggest $\log U_{\text{F}} \approx -2$. We adopt this value and a large uncertainty.

J1145+0322— The ions show absorption spanning a total of $\Delta v \approx 300 \text{ km s}^{-1}$ (Figure 27). We present the ionic column densities in Table 15. Absorption from low ions is strong for C^+ , Si^+ , Al^+ and Mg^+ and moderate for Fe^+ and Mg^0 . There is also strong absorption from high ions Si^{3+} and C^{3+} . Together the data suggests a partially ionized

gas characteristic of Lyman limit systems.

Figure 27 presents the Magellan/MagE spectrum at Ly α . Given the relatively low S/N of these data, we also included a lower resolution Keck/LRIS spectrum in the profile fits. The dominant absorber is asymmetric, suggesting blending with a weaker, unresolved component. The absorption at $v \approx +500$ km s $^{-1}$ is not associated with any metal ion detection. Assuming a single component with a b value ranging from 15–60 km s $^{-1}$, the large Ly α equivalent width and the lack of strong damping wings together restrict the range of N_{HI} to be $10^{18.0}$ – $10^{18.6}$ cm $^{-2}$. Our best fit solution gives a total $N_{\text{HI}} = 10^{18.4 \pm 0.4}$ cm $^{-2}$, where the errors are dominated by the lack of higher Lyman series lines.

The high Si $^{+}$ /Si $^{3+}$ ratio suggests a lower ionization state with $\log U \approx -3$. On the other hand the Al $^{+}$ /Al $^{3+}$ and highly saturated C IV doublet implies higher U values. These conflicting constraints suggest the profile is a blend of material with varying ionization state, although there is no obvious evidence for such a blend in the line profiles. We proceeded by adopting $\log U = -2.9$ with a larger uncertainty towards higher values.

J1204+0221— As reported previously in QPQ3, the ions show absorption spanning a total of $\Delta v \approx 760$ km s $^{-1}$ (Figure 28, or see Figure 3 of QPQ3) that we separate into three subsystems. We present ionic column densities in Table 16. We refer the reader to QPQ3 for details on the H I and photoionization modeling. Summarizing the previous findings, there is absorption from a series of low ions O 0 , C $^{+}$, Si $^{+}$, N 0 , N $^{+}$, Al $^{+}$ and Fe $^{+}$, characteristic of optically thick absorbers. Weak Si IV and C IV absorption indicate the ionization state of the gas is not extreme. The absence of strong N V and O VI limits the flux of photons with energies $h\nu \gtrsim 4$ Ryd and rules out a collisionally ionized gas with $T \approx 10^5$ K. The strong N II absorption traces the N I profile for subsystems A and C, but the ionic ratio N $^{+}$ /N 0 varies significantly across subsystem B. In QPQ3, the N II column density of subsystem A is obtained by Voigt profile modeling, while in this study it is obtained by AODM. In our AODM treatment, if a line is resolved, as in the case for this echelle sightline, we consider a component saturated if the absorption trough minimum is below 0.5 times the 1- σ error. Hence, while a good measurement for the N II column density is reported in QPQ3, a lower limit is reported in QPQ8 for consistency across the whole sample.

We present the Ly α and Ly β profiles of this absorption system and reproduced the results shown in Figure 2 of QPQ3. For subsystems A and C, the absence of strong Ly α damping wings restricts $N_{\text{HI}}^{\text{A,C}} < 10^{19}$ cm $^{-2}$, while the Ly β profile demands $b_{\text{A,C}} < 25$ km s $^{-1}$. Our best estimates give $N_{\text{HI}}^{\text{A,C}} = 10^{18.6 \pm 0.4}$ cm $^{-2}$. With the constraints on subsystems A and C, we estimated $N_{\text{HI}}^{\text{B}} = 10^{19.6 \pm 0.2}$ cm $^{-2}$ that is insensitive to the b_{B} value.

In QPQ3, we adopted $\log U \lesssim -3$ for all three subsystems. We have revised our estimate in this study. This absorption system shows a varying U parameter. For subsystems A and C, the observed Fe $^{+}$ /Fe $^{2+}$ ratio requires a lower U parameter than other ionic ratios. Nonetheless the Si $^{+}$ /Si $^{3+}$, Al $^{+}$ /Al $^{2+}$, N 0 /N $^{+}$ and C $^{+}$ /C $^{3+}$ ratios are roughly consistent with a single U value for each of subsystems A and C. For subsystem B, due to the high N_{HI} column the Cloudy predicted ionic ratios are rather insensitive to U . Other than the Si $^{+}$ /Si $^{3+}$ ratio, other ionic ratios are roughly consistent with a single U . There is compelling evidence that the foreground quasar is not shining on the gas for any reasonable gas density. The observed ionic ratios are also consistent with the EUVB being dominant if $n_{\text{H}} \lesssim 10^{-3}$ cm $^{-3}$. Detailed component-by-component fitting of the echelle spectrum reveals that the low and high ions do not have the same velocity structure. The low-to-high ion ratios, in particular C $^{+}$ /C $^{3+}$, should therefore be considered lower limits for the low ionization phase. We adopted $\log U_{\text{A}} = -3.3$, $\log U_{\text{B}} = -3.6$ and $\log U_{\text{C}} = -3.6$.

J1420+1603— The ions show complex absorption in a series of components spanning $\Delta v \approx 1350$ km s $^{-1}$ (Figure 29) that we separate into six subsystems. We present ionic column densities in Table 17. There is strong absorption throughout the interval from low-ions, e.g. O 0 , Si $^{+}$, C $^{+}$, Al $^{+}$, Fe $^{+}$, Mg $^{+}$ and Mg 0 . The absorption consistent with C II* 1335 from subsystem F cannot be associated to the C II 1334 transition at another velocity. Together with modest absorption from high ions Si $^{3+}$ and C $^{3+}$, the data suggests a partially ionized gas. The spectral resolution of FWHM ≈ 51 km s $^{-1}$ implies C II 1334 and C IV 1548 are heavily saturated in subsystems D and E. This system is one of the few cases where the N V doublet lies redward of the background quasar’s Ly α forest. We report no positive detections in any of the subsystems.

Our data covers only the Ly α transition of this complex absorption system. The high S/N spectrum exhibits no evidence for strong damping wings which constrains the total $N_{\text{HI}} < 10^{19}$ cm $^{-2}$ assuming the majority of H I gas traces the low ion metal absorption. Tighter limits may be placed on the subsystems at the ends of the interval, i.e. for subsystems A and F, $N_{\text{HI}}^{\text{A,F}} < 10^{18.5}$ cm $^{-2}$. The large Ly α equivalent widths for subsystems D and E imply $N_{\text{HI}} > 10^{18}$ cm $^{-2}$ for $b_{\text{D,E}} < 60$ km s $^{-1}$ provided line blending is not severe. We took the best estimates from ALIS and adopted a 0.4 dex uncertainty.

With the exception of the weakly absorbing subsystem A, we found the gas throughout the system is consistent with a single ionization parameter of $\log U \approx -3$. Subsystems B, C, D, E and F have a series of observed ionic ratios that together impose tight and consistent constraints on U . The relatively low U value reflects the strong low ion absorption observed throughout the complex. The U parameter for subsystem A is not as well constrained, but a higher value is preferred.

J1427-0121— The ions show absorption in roughly three distinct velocity intervals spanning a total of $\Delta v \approx 670$ km s $^{-1}$ (Figure 30) that we divide into three subsystems. We present the ionic column densities in Table 18. Low ions are detected throughout the complex, including moderate absorption from O I 1302 in subsystem C. In addition, weak C II* 1335 absorption is detected in one of the components, implying a relatively dense gas. High ion absorption from C $^{3+}$ and Si $^{3+}$ is detected in subsystems A and B and remarkably absent in subsystem C. The

C II, Si II and Si IV profiles are similar throughout the complex, whereas the C IV profile differs from the low ions in subsystem B. This suggests a contribution to C IV absorption from a different phase along the sightline.

We present the Ly α , Ly β , and Ly γ transitions of this absorption system measured using Magellan/MIKE and Magellan/MagE. These data offer a terrific puzzle: the Ly α profile of subsystem A, and to a lesser extent subsystem B, is unsaturated despite the presence of strong low ion absorption and strong Ly β and Ly γ absorption in the lower resolution MagE data. In turn, the Ly α profile would require $N_{\text{HI}} < 10^{14.5} \text{ cm}^{-2}$ while the higher order lines demand much larger N_{HI} values. We identify three scenarios that could resolve this apparent conundrum: (i) the gas is optically thin at Ly α , represents the first such case reported with corresponding C II and Si II absorption, and the absorption at Ly β and Ly γ is unrelated IGM absorption; (ii) we have performed poor sky subtraction at these wavelengths; (iii) there is unresolved Ly α emission that is ‘filling in’ the Ly α absorption (e.g. from fluorescence of the quasar ionizing flux; Hennawi & Prochaska 2013; Cantalupo et al. 2012; Hennawi et al. 2009; Finley et al. 2013; Cai et al. 2014). Of these three, the second is the least extraordinary. We have carefully inspected the data reduction process for this spectrum and cannot identify any error and further note that other lines close by in wavelength, e.g. subsystem C, exhibits complete absorption. We consider the first option to be the most improbable and therefore proceeded by fitting the Lyman series lines with a revised zero level that gives complete absorption at Ly α . Presently, we interpret the non-zero flux as unresolved Ly α emission along the sightline. We estimated a total $N_{\text{HI}}^{\text{A}} = 10^{17.3^{+0.5}_{-1.0}} \text{ cm}^{-2}$, a total $N_{\text{HI}}^{\text{B}} = 10^{18.3^{+0.2}_{-1.0}} \text{ cm}^{-2}$ and a total $N_{\text{HI}}^{\text{C}} = 10^{18.6^{+0.2}_{-1.0}} \text{ cm}^{-2}$, where the errors are dominated by blending of the absorption profiles and degeneracy between N_{HI} and b values.

Because the C IV profile does not closely track other ions, including Si IV, we give stronger weight to the Si $^{+}$ /Si $^{3+}$ ratio for constraining the U parameter. This approach is further supported by the observed C $^{+}$ /Si $^{3+}$ ratio. The only significant ionization gradient within a subsystem is in C IV, hence we consider the C IV column densities measured as upper limits when we perform ionization modeling. The gas in subsystems A and B, which exhibit high ions, is well modeled by $\log U = -3.1$ and -2.6 respectively. The absence of high ion absorption in subsystem C together with stronger low ion absorption requires a much lower U value. We adopted $\log U < -3.4$. Subsystem C shows C II* which allows us to constrain its electron density $n_e = 16 \text{ cm}^{-3}$, as discussed in Section 4.4. This n_e implies the gas receives an ionizing flux that is ≈ 0.25 of that expected should the quasar shine isotropically. Should the gas be illuminated only by the EUVB, the n_e would imply $\log U = -7.1$.

J1553+1921— The ions show absorption spanning a total of $\Delta v \approx 500 \text{ km s}^{-1}$, with the majority of low ion absorption confined to $\approx 100 \text{ km s}^{-1}$ (Figure 31). We present the ionic column densities in Table 19. This is a damped Ly α system and we observe strong absorption from low ion transitions of O 0 , Si $^{+}$, C $^{+}$, Fe $^{+}$, Al $^{+}$, Mg $^{+}$ and Mg 0 . Interestingly, we find corresponding high ion absorption at the same velocities.

The Ly α profile shows strong damping wings that constrain N_{HI} to be $10^{20.2 \pm 0.1} \text{ cm}^{-2}$, insensitive to the Doppler b . The line centroid of Ly α is consistent with the peak optical depth of the low ion transitions.

The observed Si $^{+}$ /Si $^{3+}$ ratio suggests $\log U \approx -3.2$, if these ions trace the same phase of gas. In damped Lyman alpha systems this is rarely the case (e.g. Wolfe & Prochaska 2000), but we do find close kinematic alignment between the Si II and Si IV transitions, and the absorption profiles are all narrow. This $\log U$ value is also consistent with the upper limits placed by the observed C $^{+}$ /C $^{3+}$ and Al $^{+}$ /Al $^{2+}$ ratios. Since the absorption at C II 1334 is strongly saturated, the upper limit given by C $^{+}$ /C $^{3+}$ is a generous limit even if some of the C $^{3+}$ comes from another phase of gas. We adopted $\log U = -3.2$ and allow for much lower values. At this U value, the neutral fraction is approximately 50%.

J1627+4605— Only moderate absorption from C $^{3+}$ is detected in the system we associated to J1627+4605FG. This gas spans a velocity interval of $\Delta v \approx 150 \text{ km s}^{-1}$ (Figure 32). We present the ionic column densities in Table 20. Together with an absence of any low ions, the data suggests a highly ionized gas.

We present the Ly α and Ly β velocity profiles of this system. Higher order lines are compromised by a Lyman limit system at lower redshift. Restricting to b -values ranging from $15\text{--}60 \text{ km s}^{-1}$, the Ly α equivalent width and the lack of Ly α damping wings of the dominant absorber requires $10^{15.1} \text{ cm}^{-2} < N_{\text{HI}} < 10^{18.0} \text{ cm}^{-2}$. There are three additional weak absorbers included in our model. We recovered $N_{\text{HI}} = 10^{16.9} \text{ cm}^{-2}$ as the best fitted value and adopted a large uncertainty of 0.8 dex owing to line saturation.

C $^{3+}$ is the only ion detected and our ionization constraints include limits to C $^{+}$ /C $^{3+}$ and Si $^{3+}$ /C $^{3+}$. These require $\log U$ greater than -2.5 and -2.2 respectively. We adopted $\log U = -2.0$ with a large uncertainty to higher values.

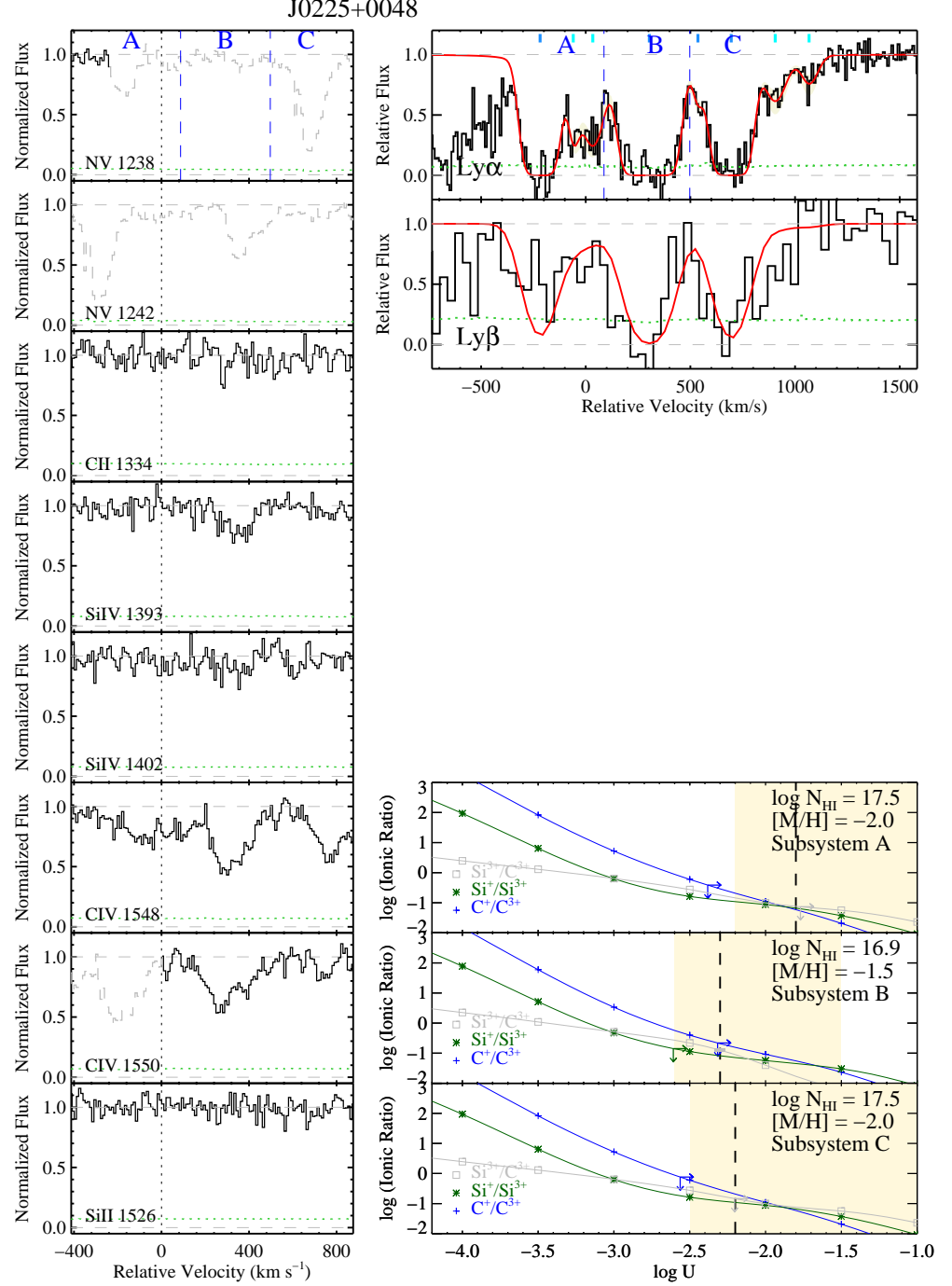


FIG. 19.— Combined figure for the J0225+0048 pair showing: (Left) Metal line transitions from the absorbers identified at velocities consistent with $z_{\text{fg}} = 2.7265$. Absorption well separated in distinct velocity intervals are designated as subsystems A, B, C, etc. and marked by the vertical dashed lines in the upper panels. Absorptions that are unrelated to the foreground quasar, e.g. blends in the Ly α forest, are presented as dashed, gray lines. The green histograms show the 1σ noise in the normalized flux. (Top right) Lyman series absorption profiles identified in the background quasar spectrum at velocities consistent with the foreground quasar of each projected pair. The green histograms show the 1σ noise in the normalized flux. The relative velocity $v = 0 \text{ km s}^{-1}$ corresponds to the redshift of the foreground quasar. For each system we performed χ^2 minimization Voigt profile modeling. We introduced H I components centered at relative velocities traced by the peak optical depths of the associated metal ion absorptions. The navy ticks mark the centroid redshifts for components traced by low ions, while the blue ticks mark the centroids for components traced by high ions. H I components not associated with any metal ions are marked with cyan ticks. Additional H I components introduced to model Ly α forest blending are omitted in the tick marks. The red curve is the convolved fit of all H I components associated with the foreground quasar, and the beige shades mark the estimated $\pm 1\sigma$ errors in H I column densities. The orange curve is the convolved fit of all H I components associated with the foreground quasar and the Ly α forest contaminations, if any. (Bottom right) Cloudy modeling of the ionization parameter U for each of the 12 quasar associated absorption systems where metal ion column measurements are available. Solid curves show predicted ionic ratios as a function of U for a series of ion pairs. Overplotted on the curves are observational constraints of the subsystems, indicated by solid boxes, whose edges are the $1-\sigma$ uncertainties, or indicated by arrows for lower and upper limits. The observations indicate a varying U .

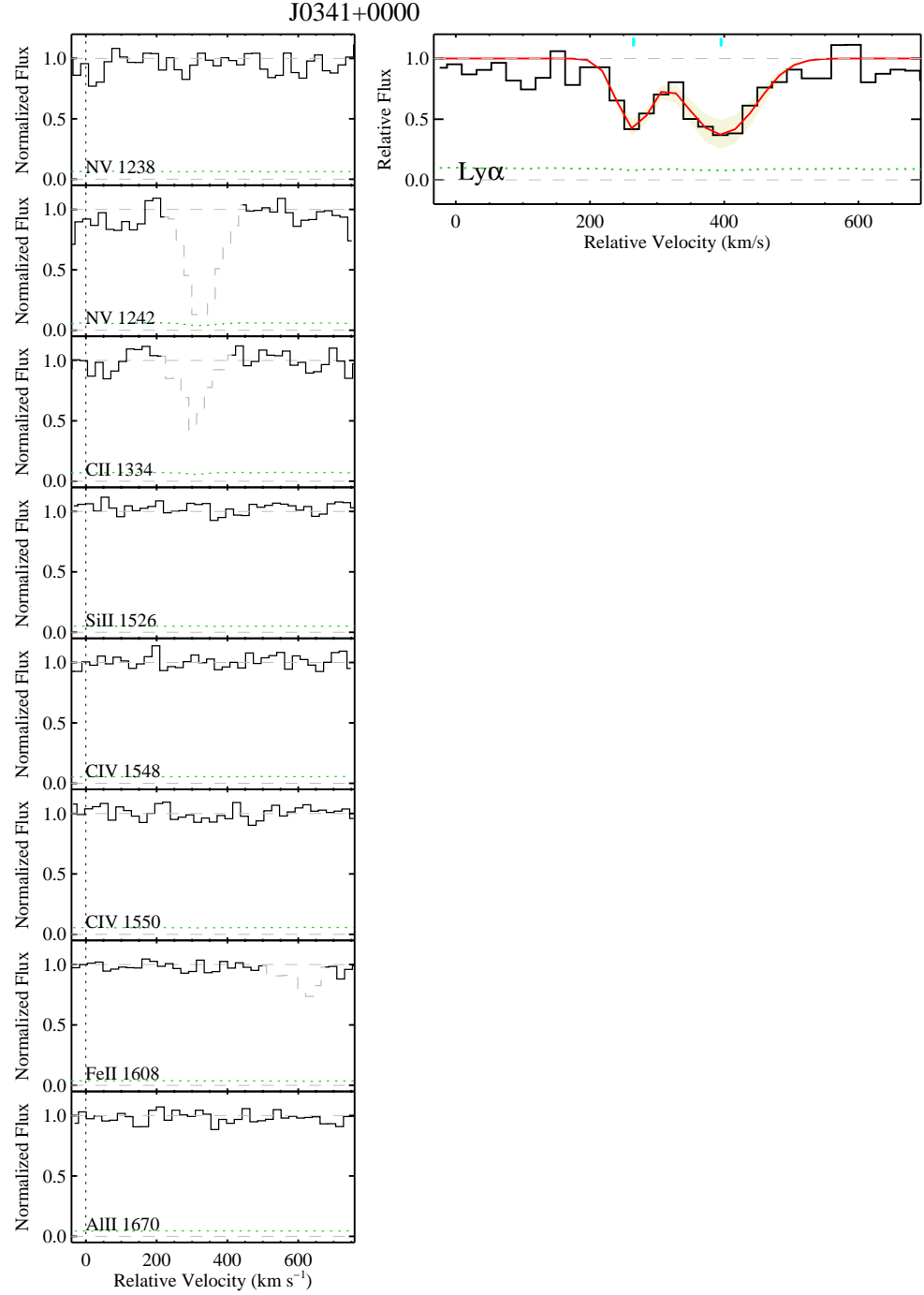


FIG. 20.— Similar to Figure 19 but for J0341+0000 at $z_{\text{fg}} = 2.1233$.

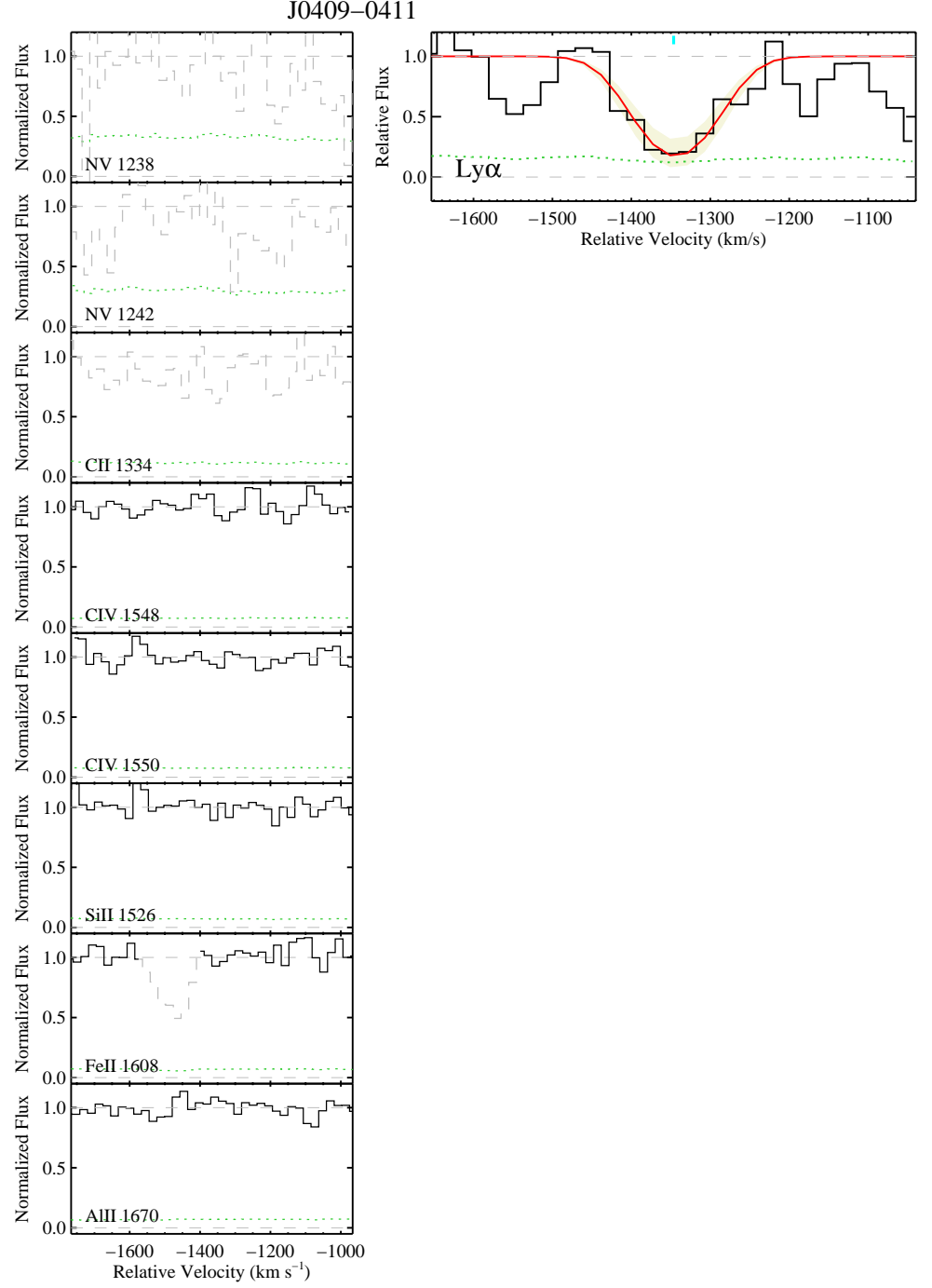
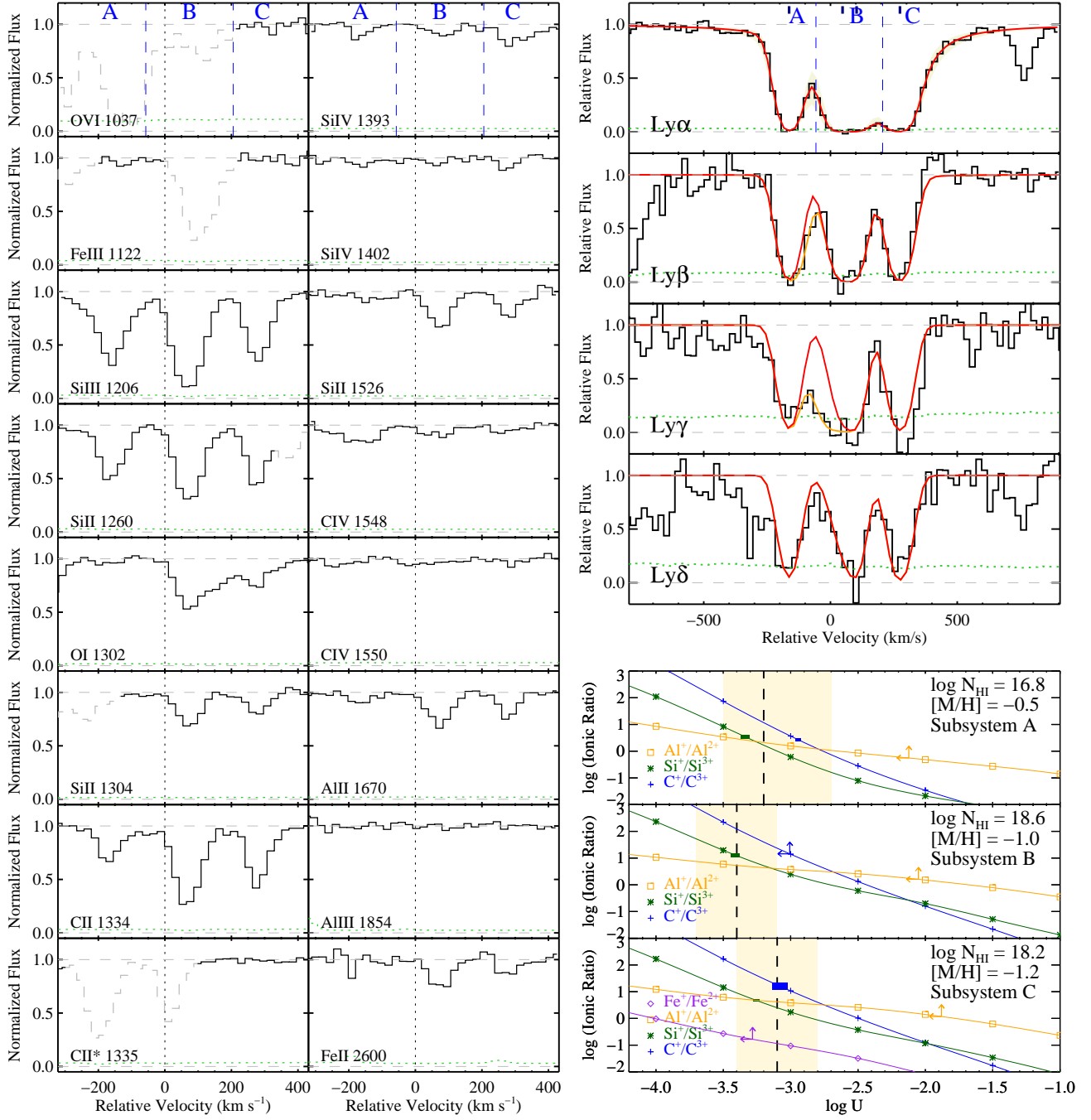
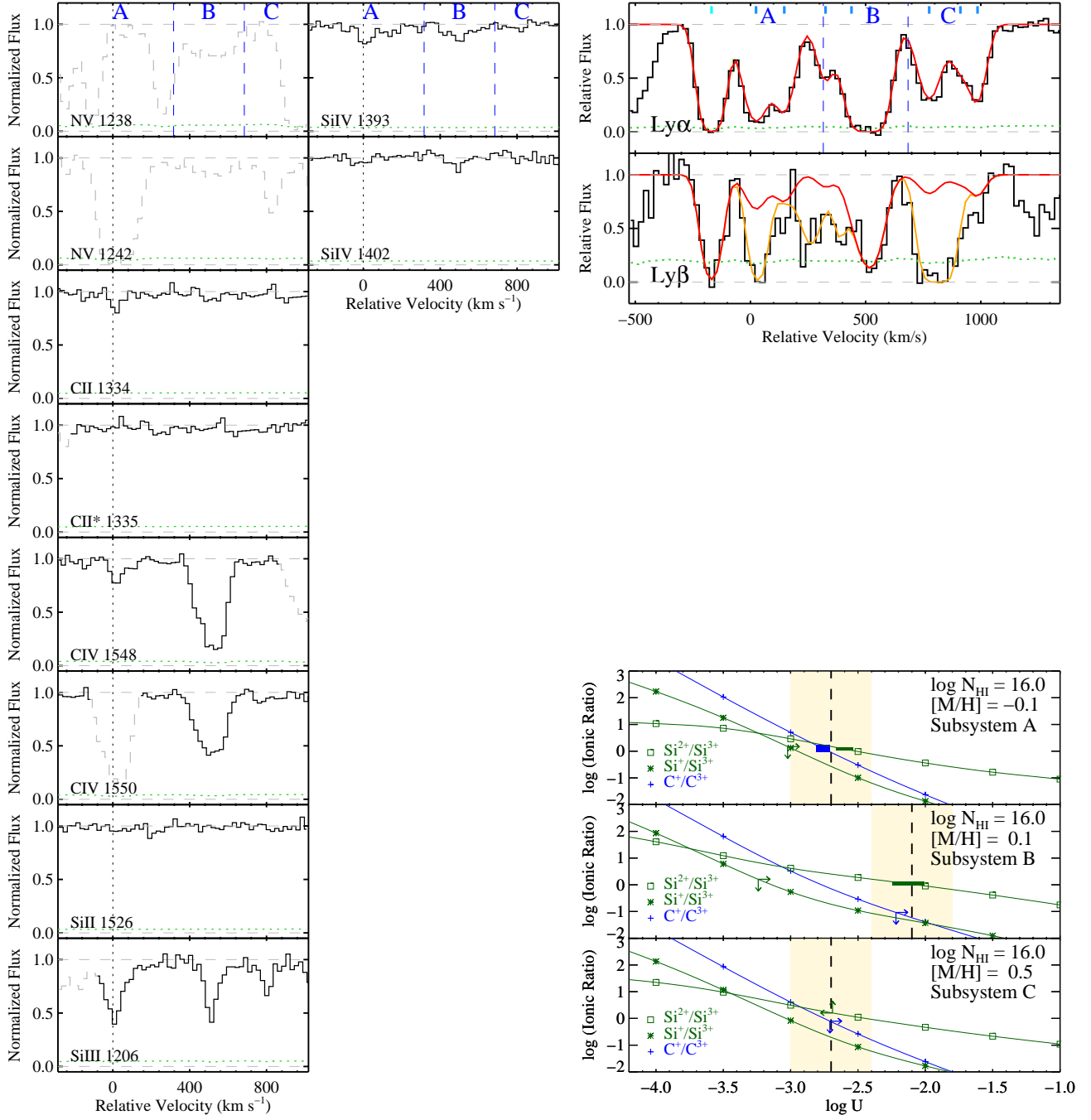


FIG. 21.— Similar to Figure 19 but for J0409-0411 at $z_{\text{fg}} = 1.7155$.

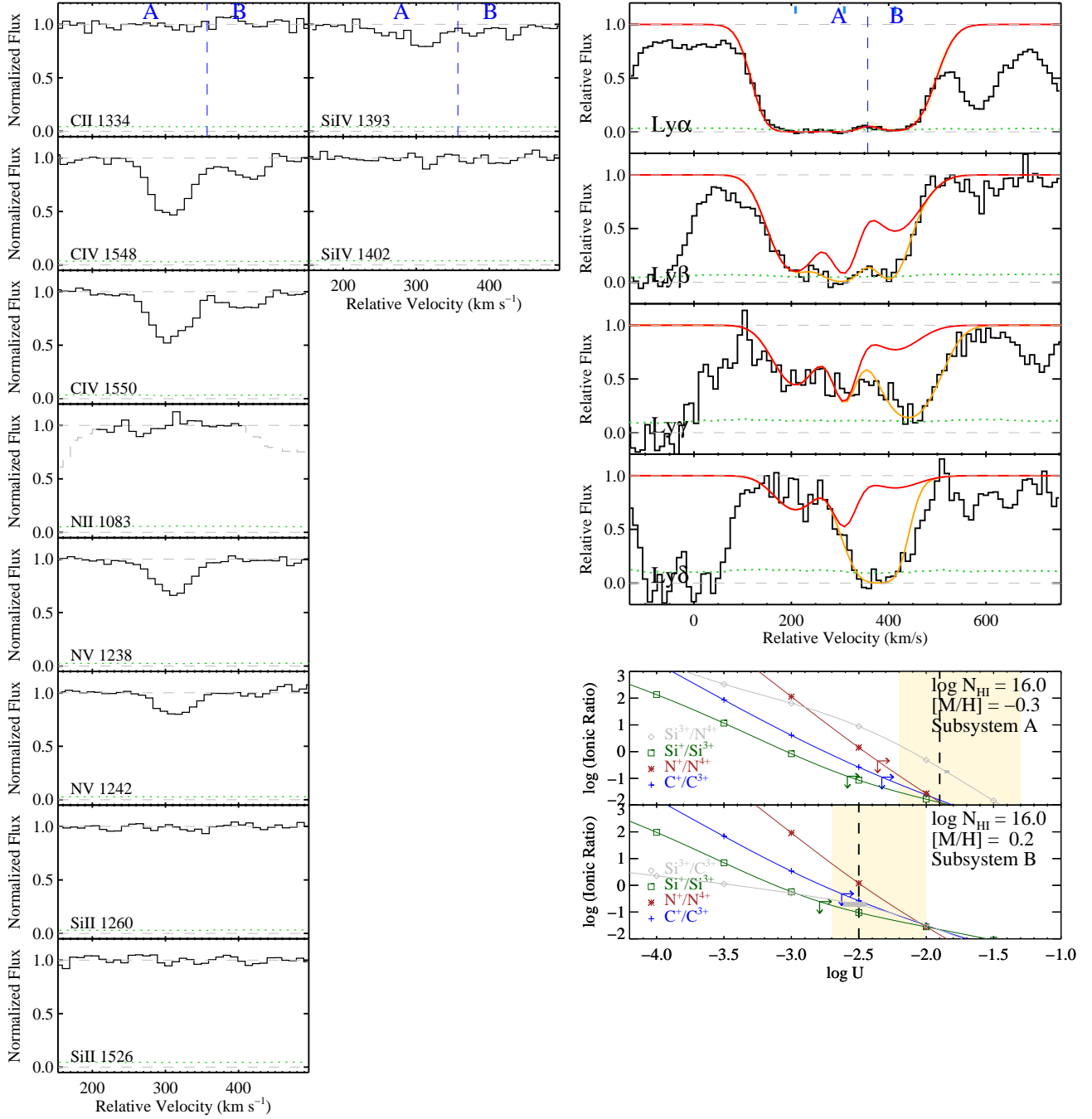
J0853-0011

FIG. 22.— Similar to Figure 19 but for J0853-0011 at $z_{\text{fg}} = 2.4014$.

J0932+0925

FIG. 23.— Similar to Figure 19 but for J0932+0925 at $z_{\text{fg}} = 2.4170$.

J1026+4614

FIG. 24.— Similar to Figure 19 but for J1026+4614 at $z_{\text{fg}} = 3.3401$.

J1038+5027

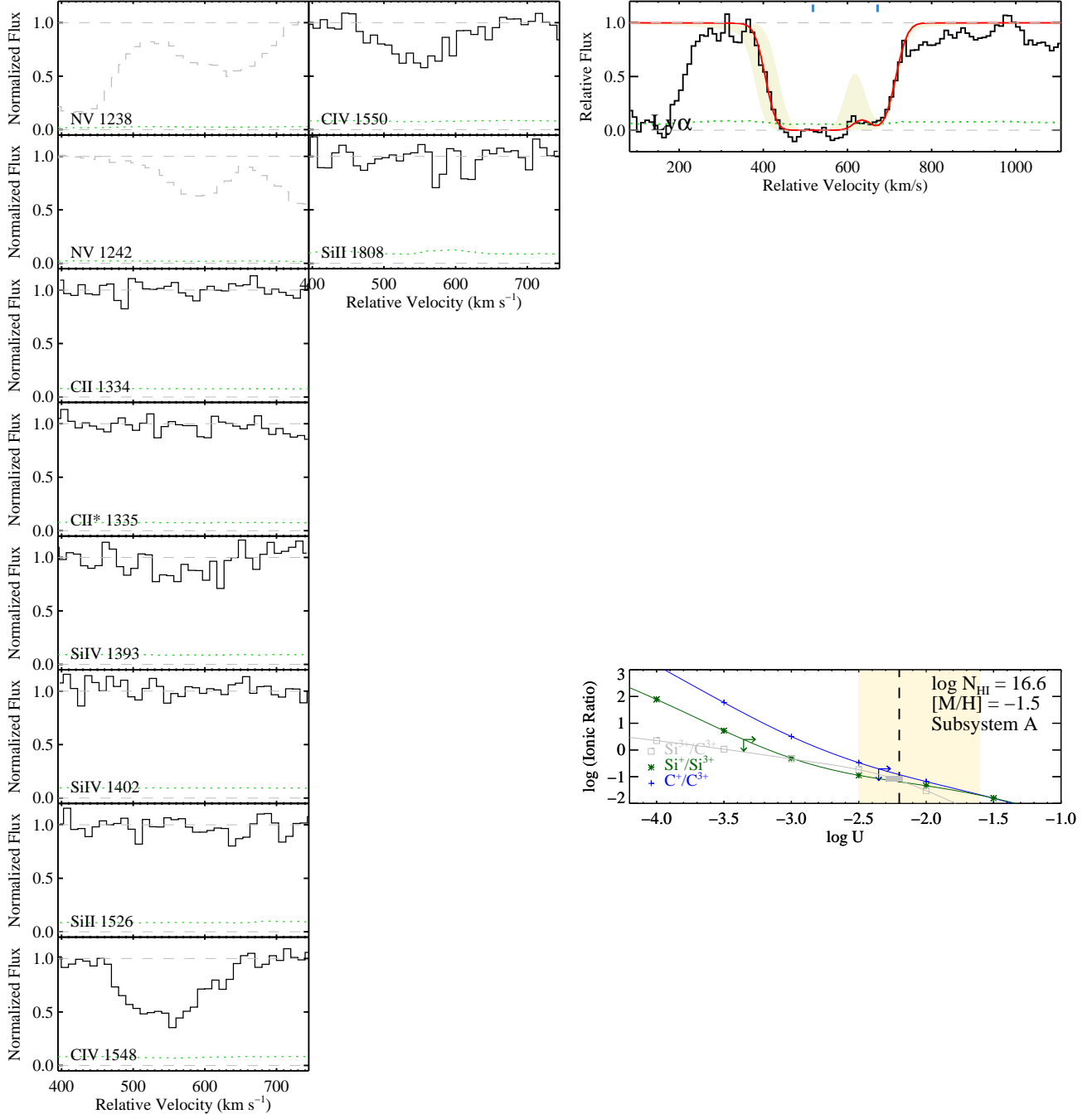
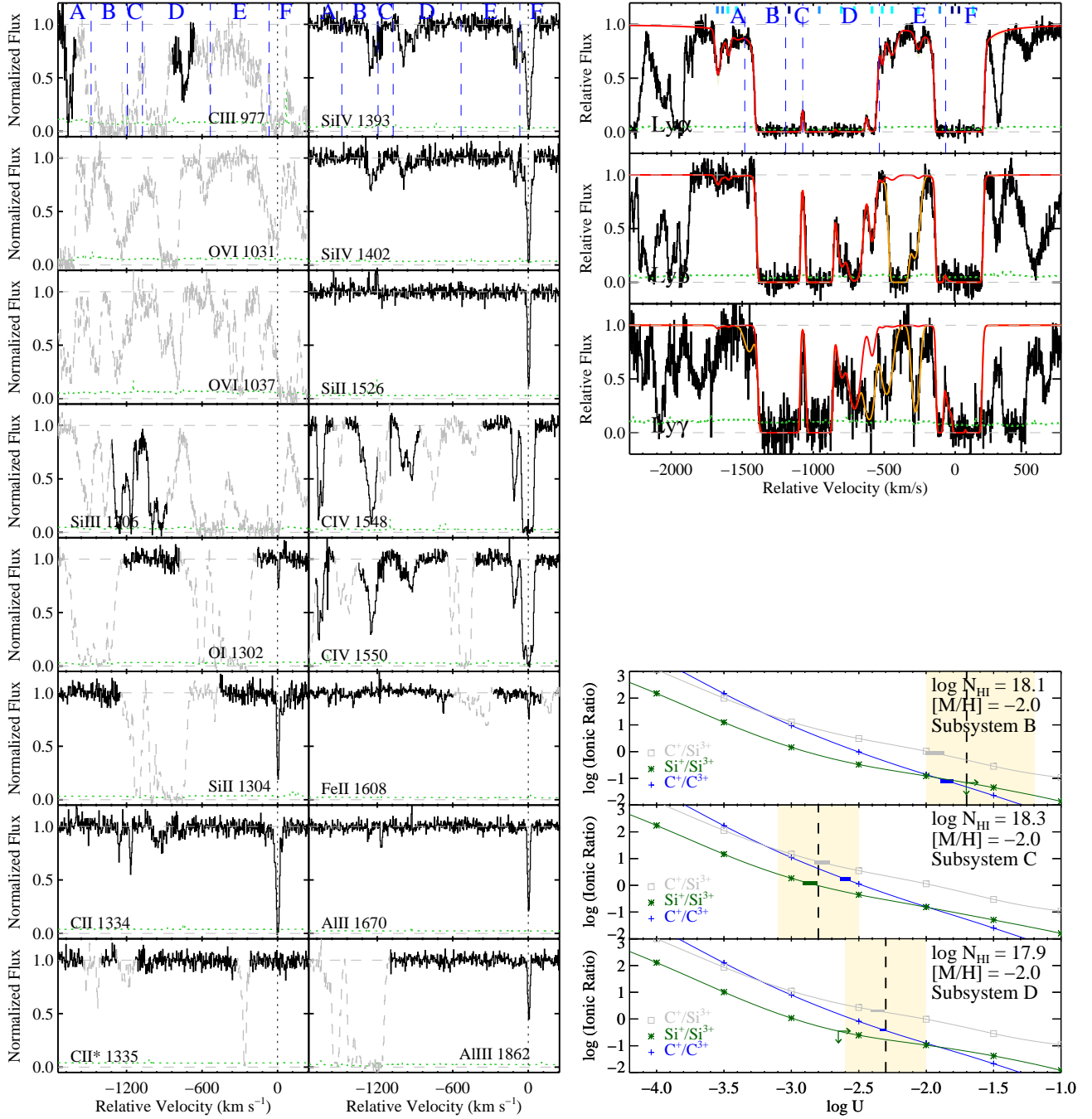
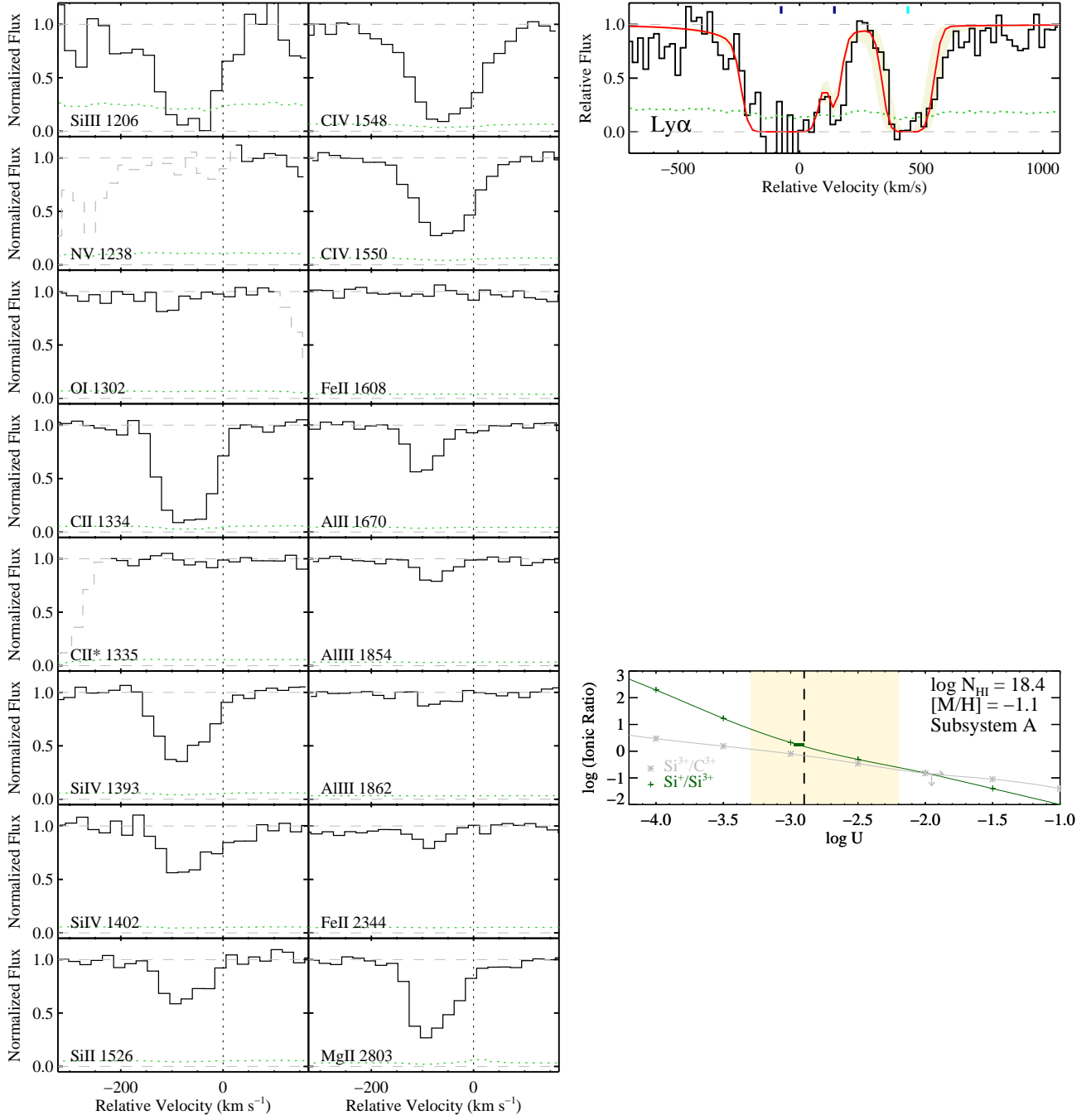


FIG. 25.— Similar to Figure 19 but for J1038+5027 at $z_{\text{fg}} = 3.1322$.

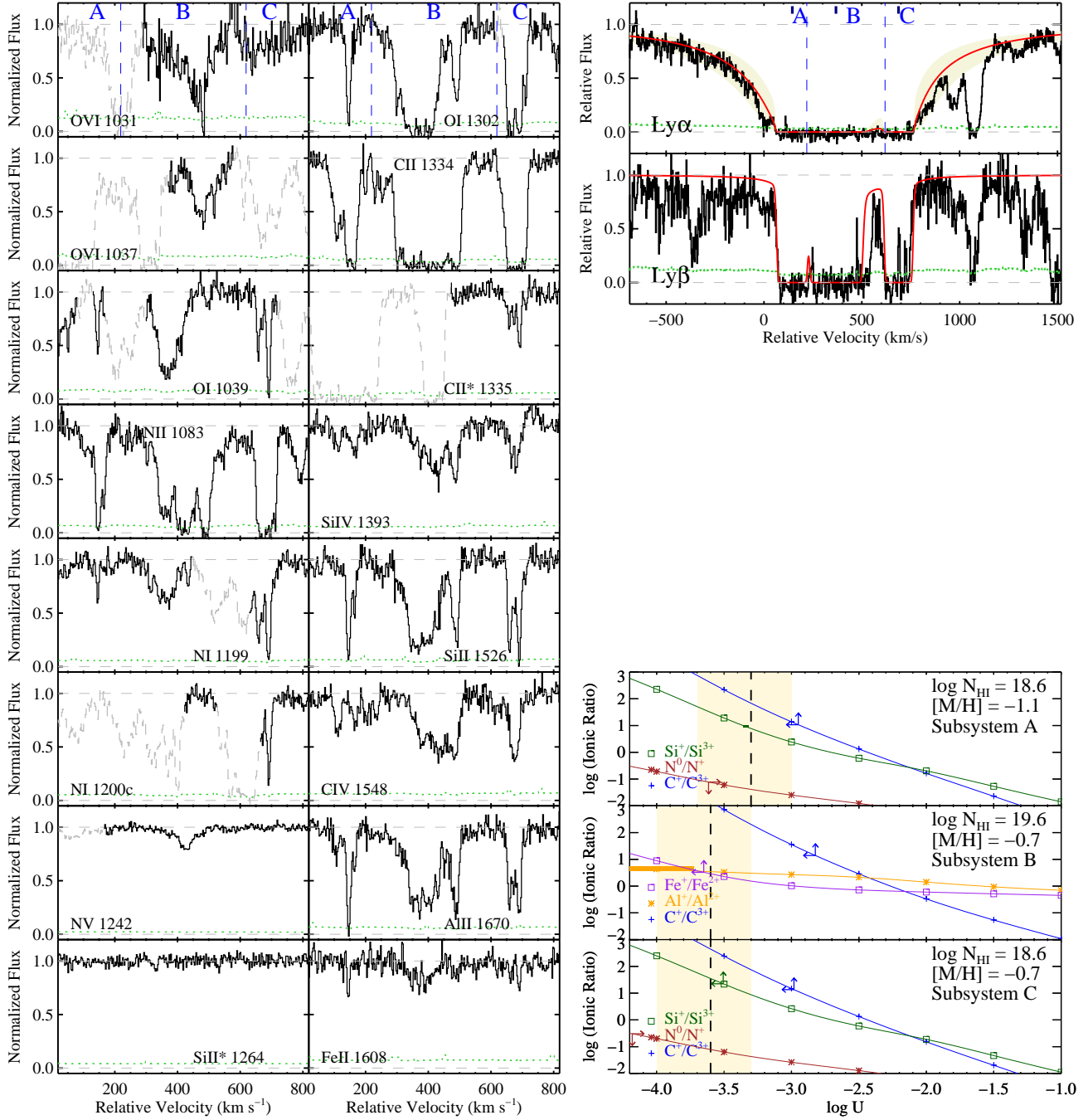
J1144+0959

FIG. 26.— Similar to Figure 19 but for J1144+0959 at $z_{\text{fg}} = 2.9731$.

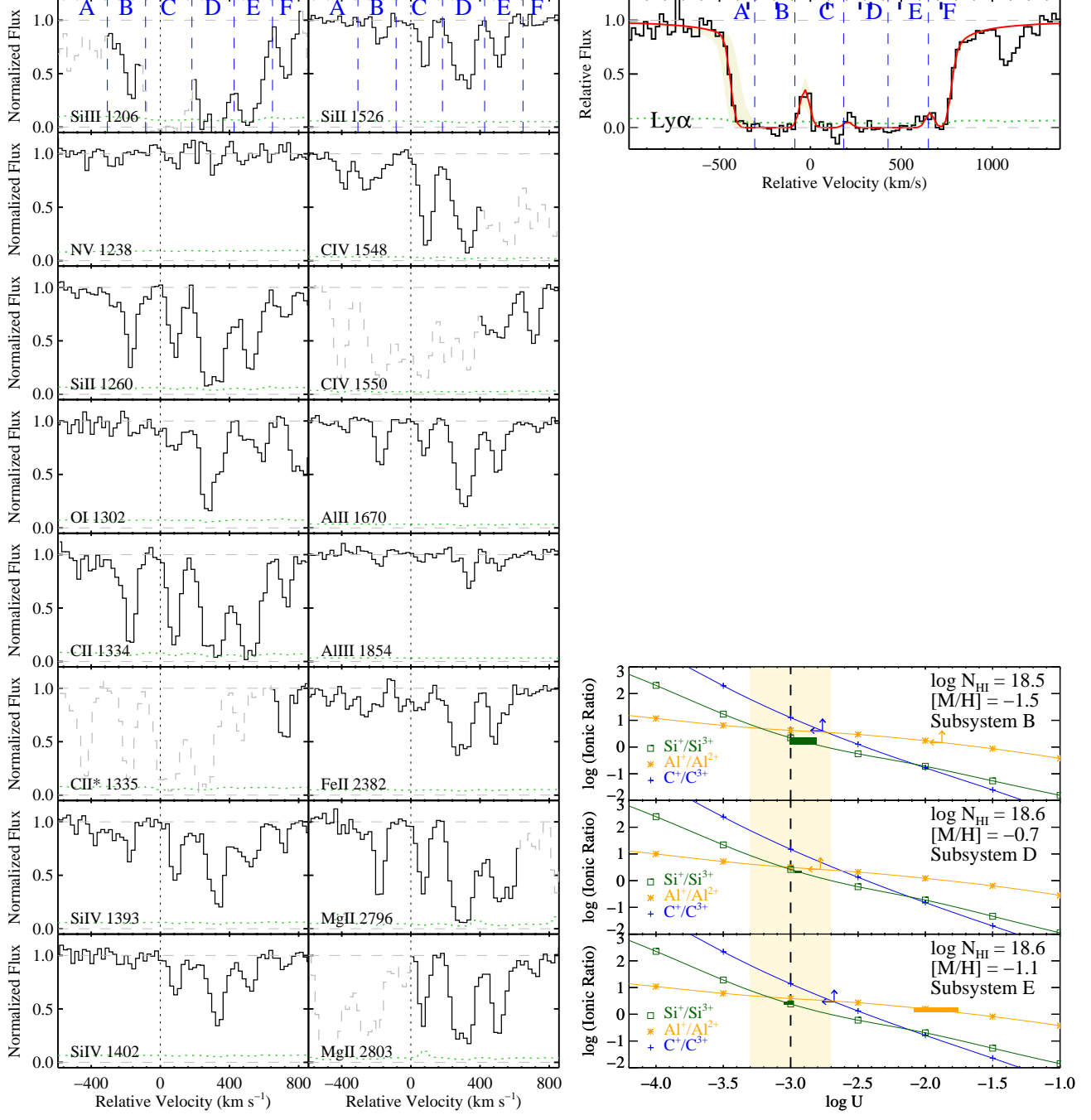
J1145+0322

FIG. 27.— Similar to Figure 19 but for J1145+0322 at $z_{\text{fg}} = 1.7652$.

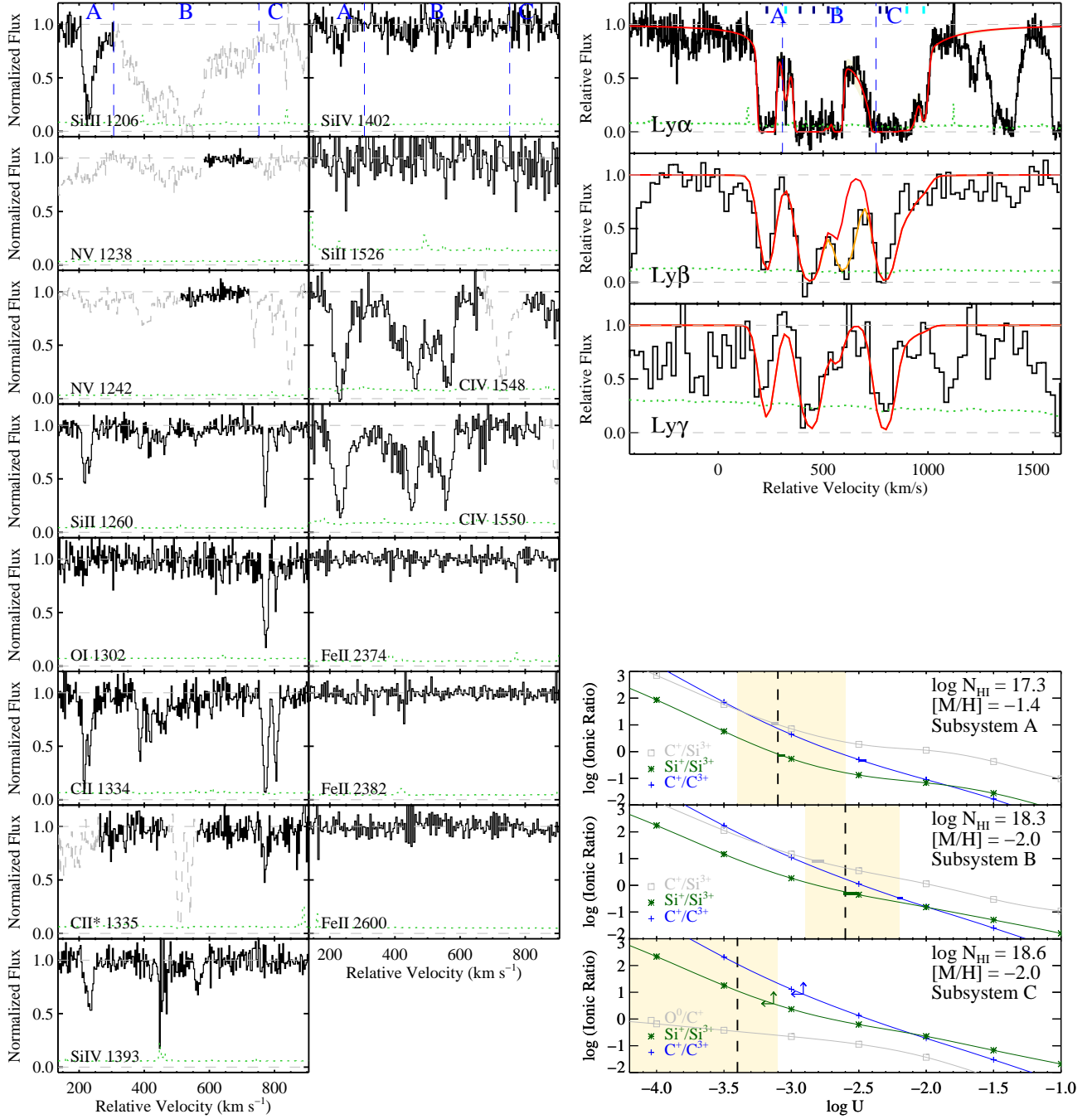
J1204+0221

FIG. 28.— Similar to Figure 19 but for J1204+0221 at $z_{\text{fg}} = 2.4358$.

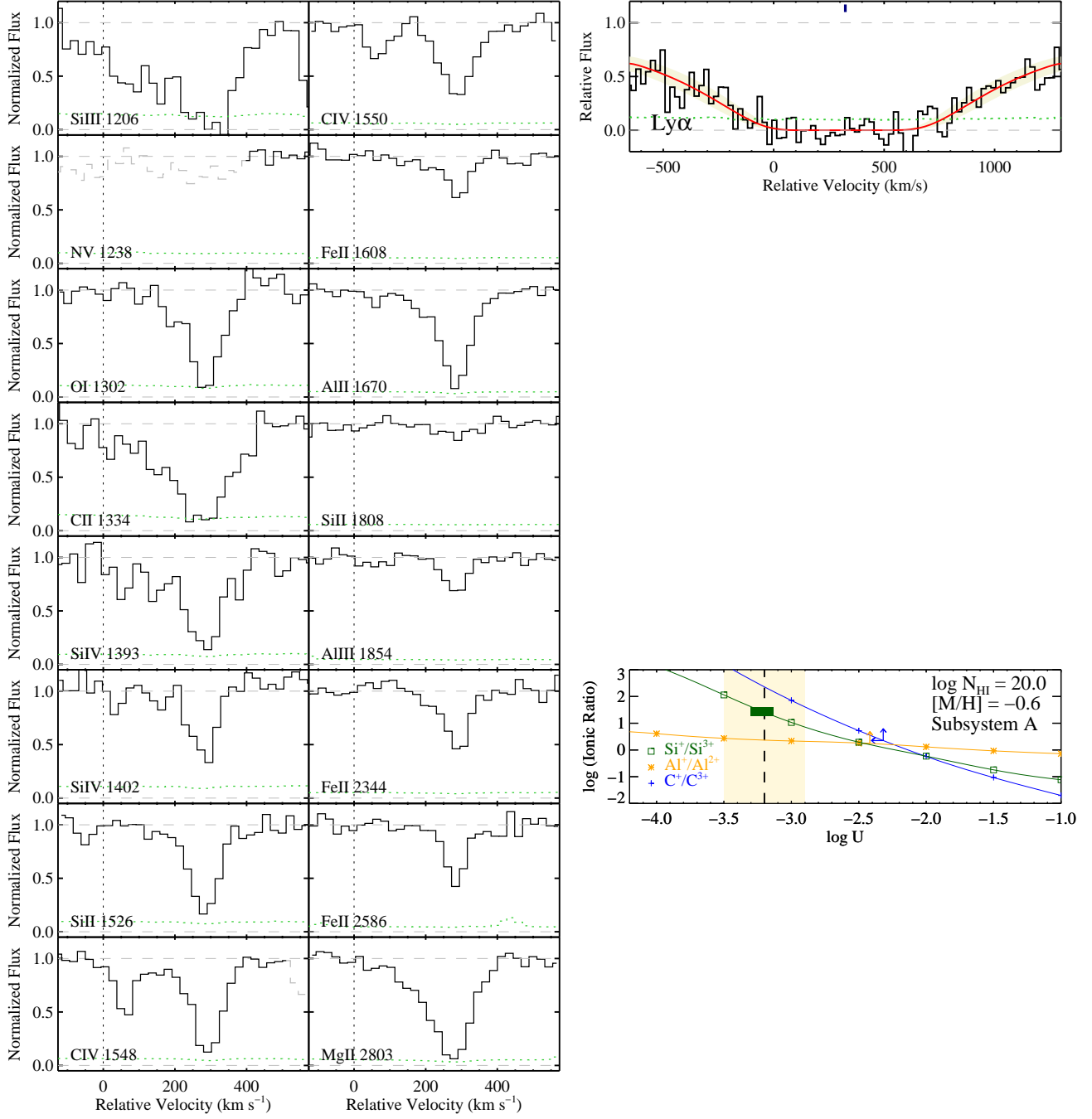
J1420+1603

FIG. 29.— Similar to Figure 19 but for J1420+1603 at $z_{\text{fg}} = 2.0197$.

J1427-0121

FIG. 30.— Similar to Figure 19 but for J1427-0121 at $z_{\text{fg}} = 2.2736$.

J1553+1921

FIG. 31.— Similar to Figure 19 but for J1553+1921 at $z_{\text{fg}} = 2.0098$.

J1627+4605

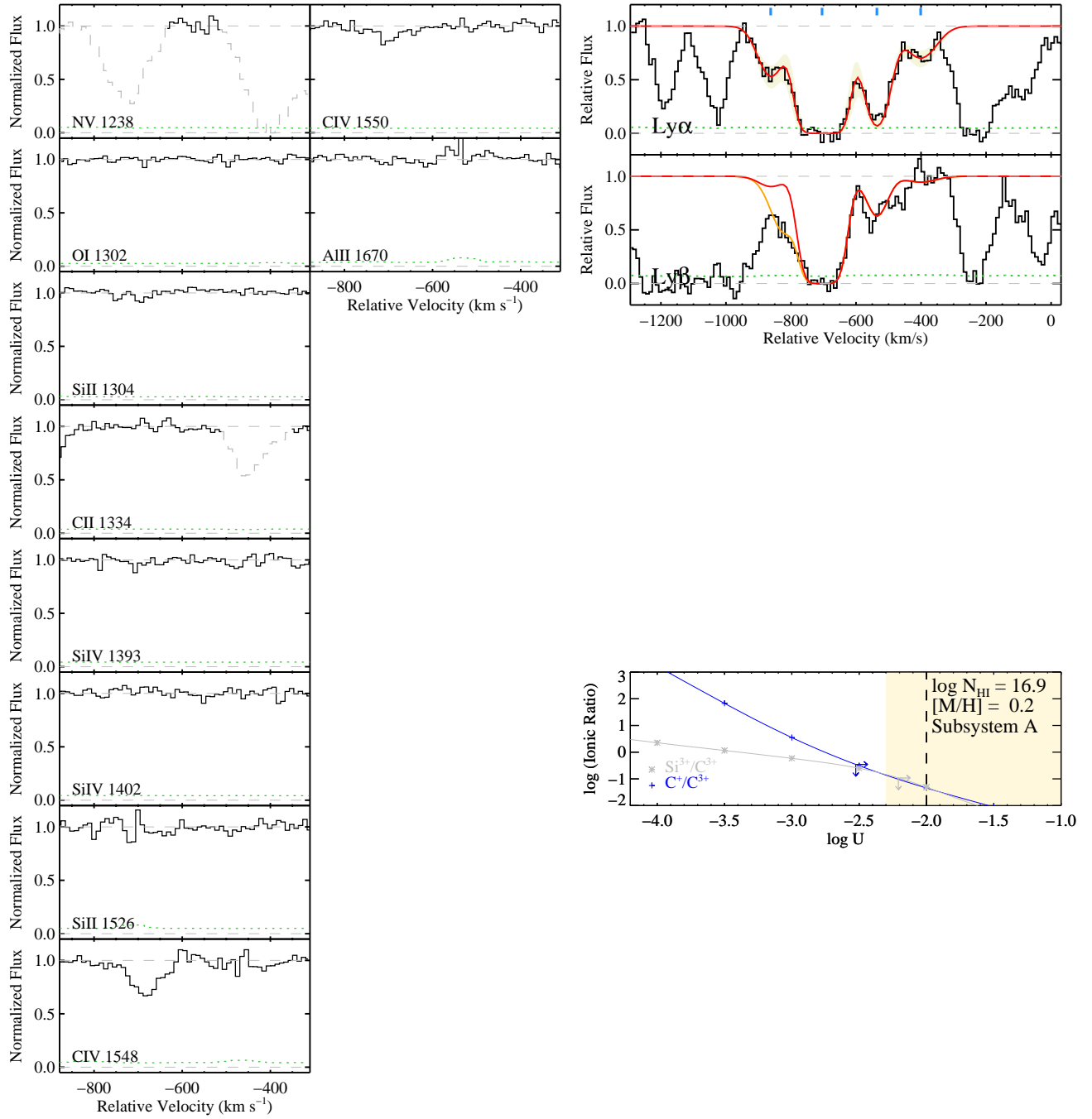
FIG. 32.— Similar to Figure 19 but for J1627+4605 at $z_{\text{fg}} = 3.8137$.

TABLE 7
IONIC COLUMN DENSITIES FOR J0225+0048FG

Ion	λ_{rest} (Å)	v_{int}^a (km s ⁻¹)	$\log N_{\text{AODM}}$	Rest EW (Å)
A				
C II	1334.5323	[−363, 88]	< 13.66	0.000 ± 0.030
C II*	1335.7077	[−363, 88]	< 13.70	0.005 ± 0.030
C IV	1548.1950	[−363, 88]	14.07 ± 0.03	0.419 ± 0.025
Si II	1260.4221	[−363, 88]	< 12.55	0.028 ± 0.016
	1526.7066	[−363, 88]	< 13.45	−0.028 ± 0.025
Si IV	1393.7550	[−363, 88]	< 12.94	0.038 ± 0.026
	1402.7700	[−363, 88]	< 13.29	0.080 ± 0.025
B				
C II	1334.5323	[88, 498]	< 13.62	0.024 ± 0.027
C II*	1335.7077	[88, 498]	< 13.67	0.065 ± 0.027
C IV	1548.1950	[88, 498]	14.28 ± 0.03	0.609 ± 0.023
Si II	1260.4221	[88, 498]	< 12.54	0.036 ± 0.016
	1526.7066	[88, 498]	< 13.44	0.004 ± 0.024
Si IV	1393.7550	[88, 498]	13.39 ± 0.05	0.184 ± 0.024
	1402.7700	[88, 498]	13.36 ± 0.06	0.121 ± 0.024
			13.47 ± 0.08	
C				
C II	1334.5323	[498, 827]	< 13.58	0.042 ± 0.024
C II*	1335.7077	[498, 827]	< 13.63	0.028 ± 0.025
C IV	1550.7700	[498, 827]	13.69 ± 0.10	0.091 ± 0.022
Si II	1260.4221	[498, 827]	< 12.48	−0.016 ± 0.014
	1526.7066	[498, 827]	< 13.40	0.032 ± 0.021
Si IV	1393.7550	[498, 827]	< 12.86	0.032 ± 0.021
	1402.7700	[498, 827]	< 13.17	0.041 ± 0.022

^a Velocity interval for the AODM column density measurement. Velocities are relative to the redshift of the foreground quasar J0225+0048FG, $z_{\text{fg}} = 2.7265$.

TABLE 8
IONIC COLUMN DENSITIES FOR J0341+0000FG

Ion	λ_{rest} (Å)	v_{int}^a (km s ⁻¹)	$\log N_{\text{AODM}}$	Rest EW (Å)
A				
C II	1334.5323	[120, 470]	< 14.00	0.146 ± 0.028
C II*	1335.7077	[120, 470]	< 13.69	0.006 ± 0.029
C IV	1548.1950	[120, 470]	< 13.28	−0.003 ± 0.026
	1550.7700	[120, 470]	< 13.59	0.029 ± 0.026
N V	1238.8210	[120, 470]	< 13.54	0.038 ± 0.024
Al II	1670.7874	[120, 470]	< 12.18	0.031 ± 0.023
Si II	1526.7066	[120, 470]	< 13.42	−0.033 ± 0.023
Fe II	1608.4511	[120, 470]	< 13.62	0.035 ± 0.018

TABLE 8 — *Continued*

Ion	λ_{rest} (Å)	v_{int}^a (km s ⁻¹)	$\log N_{\text{AODM}}$	Rest EW (Å)
-----	--------------------------------	---	------------------------	----------------

^a Velocity interval for the AODM column density measurement. Velocities are relative to the redshift of the foreground quasar J0341+0000FG, $z_{\text{fg}} = 2.1233$.

TABLE 9
IONIC COLUMN DENSITIES FOR J0409-0411FG

Ion	λ_{rest} (Å)	v_{int}^a (km s ⁻¹)	$\log N_{\text{AODM}}$	Rest EW (Å)
A				
C II	1334.5323	[−1458, −1238]	< 13.97	0.156 ± 0.038
C IV	1548.1950	[−1458, −1238]	< 13.31	−0.033 ± 0.028
	1550.7700	[−1458, −1238]	< 13.64	0.024 ± 0.029
Al II	1670.7874	[−1458, −1238]	< 12.26	−0.050 ± 0.029
Si II	1526.7066	[−1458, −1238]	< 13.48	−0.005 ± 0.026
Fe II	1608.4511	[−1458, −1238]	< 14.12	0.128 ± 0.027

^a Velocity interval for the AODM column density measurement. Velocities are relative to the redshift of the foreground quasar J0409-0411FG, $z_{\text{fg}} = 1.7155$.

TABLE 10
IONIC COLUMN DENSITIES FOR J0853-0011FG

Ion	λ_{rest} (Å)	v_{int}^a (km s ⁻¹)	$\log N_{\text{AODM}}$	Rest EW (Å)
A				
C II	1334.5323	[−271, −51]	13.89 ± 0.03	0.139 ± 0.010
C IV	1548.1950	[−271, −51]	13.45 ± 0.04	0.118 ± 0.010
	1550.7700	[−271, −51]	13.49 ± 0.04	0.035 ± 0.010
N V	1242.8040	[−271, −51]	13.26 ± 0.13	0.080 ± 0.010
O I	1302.1685	[−271, −51]	< 13.90	0.016 ± 0.006
Al II	1670.7874	[−271, −51]	< 13.36	0.016 ± 0.006
Al III	1854.7164	[−271, −51]	< 13.36	0.053 ± 0.008
	1862.7895	[−271, −51]	12.08 ± 0.07	0.005 ± 0.012
Si II	1193.2897	[−271, −51]	< 12.33	0.039 ± 0.013
	1260.4221	[−271, −51]	< 12.33	0.101 ± 0.010
	1526.7066	[−271, −51]	< 12.33	0.201 ± 0.008
	1808.0130	[−271, −51]	13.26 ± 0.03	0.060 ± 0.009
Si III	1206.5000	[−271, −51]	13.37 ± 0.06	0.036 ± 0.010
Si IV	1393.7550	[−271, −51]	< 14.76	0.315 ± 0.008
	1402.7700	[−271, −51]	> 13.30	0.037 ± 0.009
Fe II	1608.4511	[−271, −51]	> 13.30	0.039 ± 0.008
	2344.2140	[−271, −51]	12.72 ± 0.07	−0.006 ± 0.009
	2374.4612	[−271, −51]	12.63 ± 0.10	0.004 ± 0.030
	2382.7650	[−271, −51]	12.94 ± 0.09	0.013 ± 0.023
	2586.6500	[−271, −51]	< 12.67	−0.012 ± 0.026
	2600.1729	[−271, −51]	< 13.29	0.084 ± 0.026
Fe III	1122.5260	[−271, −51]	< 13.33	0.013 ± 0.035
			< 12.88	0.046 ± 0.011

TABLE 10 — *Continued*

Ion	λ_{rest} (Å)	v_{int}^a (km s ⁻¹)	$\log N_{\text{AODM}}$	Rest EW (Å)
B				
C II	1334.5323	[−51, 209]	> 14.40	0.345 ± 0.011
C IV	1548.1950	[−51, 209]	13.24 ± 0.06	0.064 ± 0.011
	1550.7700	[−51, 209]	13.21 ± 0.07	0.044 ± 0.011
N V	1242.8040	[−51, 209]	13.35 ± 0.11	< 14.07
O I	1302.1685	[−51, 209]	< 14.07	0.119 ± 0.011
Al II	1670.7874	[−51, 209]	14.68 ± 0.03	0.287 ± 0.005
Al III	1854.7164	[−51, 209]	14.68 ± 0.03	0.156 ± 0.009
	1862.7895	[−51, 209]	12.58 ± 0.03	< 12.38
Si II	1193.2897	[−51, 209]	< 12.37	0.000 ± 0.013
	1260.4221	[−51, 209]	< 12.78	0.049 ± 0.013
	1304.3702	[−51, 209]	13.91 ± 0.03	> 13.79
	1526.7066	[−51, 209]	> 13.49	0.278 ± 0.010
	1808.0130	[−51, 209]	14.02 ± 0.03	0.304 ± 0.008
Si III	1206.5000	[−51, 209]	14.02 ± 0.03	0.132 ± 0.006
Si IV	1393.7550	[−51, 209]	13.82 ± 0.03	0.152 ± 0.009
Fe II	2382.7650	[−51, 209]	< 14.79	0.038 ± 0.010
	2586.6500	[−51, 209]	> 13.58	0.443 ± 0.009
	2600.1729	[−51, 209]	> 13.58	0.056 ± 0.009
			12.81 ± 0.07	0.028 ± 0.009
			12.80 ± 0.14	0.028 ± 0.009
			13.10 ± 0.04	< 13.31
			13.21 ± 0.11	0.025 ± 0.009
			< 13.69	0.083 ± 0.022
			13.01 ± 0.08	0.018 ± 0.026
			13.31 ± 0.11	0.129 ± 0.028
			13.12 ± 0.05	0.079 ± 0.020
				0.166 ± 0.022
C				
C II	1334.5323	[209, 379]	14.10 ± 0.03	0.195 ± 0.009
C II*	1335.7077	[209, 379]	< 13.24	0.011 ± 0.010
C IV	1548.1950	[209, 379]	< 13.24	0.031 ± 0.009
	1550.7700	[209, 379]	12.90 ± 0.12	0.019 ± 0.009
N V	1242.8040	[209, 379]	12.90 ± 0.12	< 13.16
O I	1302.1685	[209, 379]	< 13.88	0.076 ± 0.009
O VI	1037.6167	[209, 379]	< 13.88	14.31 ± 0.03
Al II	1670.7874	[209, 379]	14.31 ± 0.03	0.135 ± 0.005
Al III	1854.7164	[209, 379]	< 14.07	0.014 ± 0.024
	1862.7895	[209, 379]	< 14.07	12.34 ± 0.04
Si II	1193.2897	[213, 379]	12.34 ± 0.04	0.092 ± 0.008
	1304.3702	[209, 379]	< 12.27	< 12.27
	1526.7066	[209, 379]	< 12.57	−0.006 ± 0.010
	1808.0130	[209, 379]	13.65 ± 0.03	0.010 ± 0.010
Si III	1206.5000	[213, 379]	> 13.43	0.139 ± 0.008
Si IV	1393.7550	[209, 379]	13.70 ± 0.03	0.065 ± 0.005
	1402.7700	[209, 379]	13.59 ± 0.04	0.093 ± 0.009
Fe II	1608.4511	[209, 379]	< 14.61	0.005 ± 0.008
	2344.2140	[209, 379]	> 13.18	0.232 ± 0.007
	2374.4612	[209, 379]	> 13.18	12.97 ± 0.04
	2382.7650	[209, 379]	13.02 ± 0.04	0.089 ± 0.007
	2586.6500	[209, 379]	12.71 ± 0.14	0.022 ± 0.007
	2600.1729	[209, 379]	12.90 ± 0.06	0.017 ± 0.007
Fe III	1122.5260	[209, 379]	< 13.21	0.096 ± 0.025
			13.27 ± 0.11	0.020 ± 0.020
			< 13.60	0.126 ± 0.023
			12.94 ± 0.08	< 13.10
			< 13.10	0.032 ± 0.017
			12.75 ± 0.13	0.075 ± 0.023
			< 13.68	< 13.68
			< 13.68	0.006 ± 0.009

TABLE 10 — *Continued*

Ion	λ_{rest} (Å)	v_{int}^a (km s ⁻¹)	$\log N_{\text{AODM}}$	Rest EW (Å)
-----	--------------------------------	---	------------------------	----------------

^a Velocity interval for the AODM column density measurement. Velocities are relative to the redshift of the foreground quasar J0853-0011FG, $z_{\text{fg}} = 2.4014$.

TABLE 11
IONIC COLUMN DENSITIES FOR J0932+0925FG

Ion	λ_{rest} (Å)	v_{int}^a (km s ⁻¹)	$\log N_{\text{AODM}}$	Rest EW (Å)
A				
C II			13.72 ± 0.11	
	1334.5323	[−237, 316]	13.72 ± 0.11	0.100 ± 0.025
C II*			< 13.62	
	1335.7077	[−190, 316]	< 13.62	0.069 ± 0.025
C IV			13.62 ± 0.06	
	1548.1950	[−237, 316]	13.62 ± 0.06	0.159 ± 0.023
	1550.7700	[−237, 316]	< 14.83	0.786 ± 0.022
N V			< 15.36	
	1242.8040	[−237, 316]	< 15.36	1.004 ± 0.026
Al II			< 12.07	
	1670.7874	[−237, 316]	< 12.07	0.005 ± 0.018
Al III			< 12.61	
	1854.7164	[−237, 316]	< 12.61	-0.005 ± 0.022
	1862.7895	[−237, 316]	< 13.05	0.072 ± 0.030
Si II			< 13.40	
	1526.7066	[−237, 316]	< 13.40	0.063 ± 0.020
	1808.0130	[−237, 316]	< 14.94	0.013 ± 0.018
Si III			13.31 ± 0.03	
	1206.5000	[−140, 316]	13.31 ± 0.03	0.350 ± 0.020
Si IV			13.23 ± 0.05	
	1393.7550	[−237, 316]	13.23 ± 0.05	0.145 ± 0.018
	1402.7700	[−237, 316]	< 13.09	0.002 ± 0.019
Fe II			< 13.04	
	1608.4511	[−237, 316]	< 14.22	0.210 ± 0.018
	2344.2140	[−237, 316]	< 13.47	0.156 ± 0.040
	2374.4612	[−237, 316]	< 14.16	0.215 ± 0.046
	2382.7650	[−237, 316]	< 13.04	0.167 ± 0.054
	2586.6500	[−237, 316]	< 13.56	0.061 ± 0.049
	2600.1729	[−237, 316]	< 13.13	0.128 ± 0.056
B				
C II			< 13.52	
	1334.5323	[316, 684]	< 13.52	0.048 ± 0.022
C II*			< 13.57	
	1335.7077	[316, 684]	< 13.57	0.059 ± 0.022
C IV			14.56 ± 0.03	
	1548.1950	[316, 684]	> 14.52	0.755 ± 0.017
	1550.7700	[316, 684]	14.56 ± 0.03	0.537 ± 0.018
N V			< 14.25	
	1242.8040	[316, 684]	< 14.25	0.178 ± 0.024
Al II			< 11.98	
	1670.7874	[316, 684]	< 11.98	-0.003 ± 0.015
Al III			< 12.54	
	1854.7164	[316, 684]	< 12.54	0.014 ± 0.019
	1862.7895	[316, 684]	< 12.87	0.012 ± 0.020
Si II			< 13.27	
	1526.7066	[316, 684]	< 13.27	-0.002 ± 0.016
	1808.0130	[316, 684]	< 14.85	0.008 ± 0.015
Si III			13.10 ± 0.04	
	1206.5000	[316, 684]	13.10 ± 0.04	0.212 ± 0.019
Si IV			13.06 ± 0.07	
	1393.7550	[316, 684]	13.06 ± 0.07	0.098 ± 0.015
	1402.7700	[316, 684]	< 13.01	0.008 ± 0.016
Fe II			< 12.90	
	1608.4511	[316, 684]	< 13.91	0.104 ± 0.015
	2344.2140	[316, 684]	< 13.35	0.021 ± 0.041
	2374.4612	[316, 684]	< 13.90	0.080 ± 0.041
	2382.7650	[316, 684]	< 13.09	0.184 ± 0.042
	2586.6500	[316, 684]	< 13.41	0.030 ± 0.035
	2600.1729	[316, 684]	< 12.90	-0.005 ± 0.039

TABLE 11 — *Continued*

Ion	λ_{rest} (Å)	v_{int}^a (km s ⁻¹)	$\log N_{\text{AODM}}$	Rest EW (Å)
C				
C II	1334.5323	[685, 1018]	< 13.50	0.057 ± 0.021
C II*	1335.7077	[685, 1018]	< 13.55	0.038 ± 0.021
C IV	1548.1950	[685, 1018]	13.61 ± 0.11	0.355 ± 0.018
	1550.7700	[685, 1018]	> 14.07	0.079 ± 0.020
N V	1242.8040	[685, 1018]	< 14.53	0.299 ± 0.022
Al II	1670.7874	[685, 1018]	< 14.53	0.055 ± 0.015
Al III	1854.7164	[685, 1018]	12.09 ± 0.11	0.050 ± 0.019
	1862.7895	[685, 1018]	< 12.56	0.022 ± 0.020
Si II	1526.7066	[685, 1018]	< 12.86	0.016 ± 0.016
	1808.0130	[685, 1018]	< 13.26	0.062 ± 0.014
Si III	1206.5000	[685, 1018]	< 15.00	0.150 ± 0.018
Si IV	1393.7550	[685, 1018]	12.89 ± 0.05	0.018 ± 0.015
	1402.7700	[685, 1018]	< 12.69	0.000 ± 0.015
Fe II	1608.4511	[685, 1018]	< 12.99	0.183 ± 0.013
	2344.2140	[685, 1018]	< 12.90	0.002 ± 0.033
	2374.4612	[685, 1018]	< 14.18	0.028 ± 0.042
	2382.7650	[685, 1018]	< 13.25	0.269 ± 0.040
	2586.6500	[685, 1018]	< 13.91	0.006 ± 0.030
	2600.1729	[685, 1018]	< 13.27	0.087 ± 0.038
			< 13.35	
			< 12.90	

^a Velocity interval for the AODM column density measurement. Velocities are relative to the redshift of the foreground quasar J0932+0925FG, $z_{\text{fg}} = 2.4170$.

TABLE 12
IONIC COLUMN DENSITIES FOR J1026+4614FG

Ion	λ_{rest} (Å)	v_{int}^a (km s ⁻¹)	$\log N_{\text{AODM}}$	Rest EW (Å)
A				
C II	1334.5323	[240, 360]	< 13.02	0.008 ± 0.007
C II*	1335.7077	[240, 360]	< 13.06	-0.016 ± 0.007
C IV	1548.1950	[240, 360]	13.98 ± 0.03	0.182 ± 0.006
	1550.7700	[240, 360]	> 13.76	0.156 ± 0.006
N II	1083.9900	[240, 360]	13.98 ± 0.03	0.001 ± 0.007
N V	1238.8210	[240, 360]	< 13.32	0.007 ± 0.005
	1242.8040	[240, 360]	< 13.32	-0.002 ± 0.008
Si II	1260.4221	[240, 360]	13.67 ± 0.03	0.007 ± 0.005
	1526.7066	[240, 360]	13.66 ± 0.03	0.086 ± 0.004
Si IV	1393.7550	[240, 360]	13.70 ± 0.04	0.049 ± 0.004
	1402.7700	[240, 360]	< 11.98	0.068 ± 0.007
			< 11.99	0.005 ± 0.007
			< 12.97	
			12.91 ± 0.05	
			12.91 ± 0.05	
			< 12.64	
B				
C II	1334.5323	[357, 446]	< 12.95	-0.009 ± 0.006
C II*	1335.7077	[357, 446]	< 12.96	-0.004 ± 0.006
C IV	1548.1950	[357, 446]	< 13.01	0.060 ± 0.005
	1550.7700	[357, 446]	< 13.01	0.055 ± 0.005
N V			13.27 ± 0.03	
			13.21 ± 0.04	
			13.46 ± 0.05	
			< 12.67	

TABLE 12 — *Continued*

Ion	λ_{rest} (Å)	v_{int}^a (km s ⁻¹)	$\log N_{\text{AODM}}$	Rest EW (Å)
Si II	1238.8210	[357, 446]	< 12.67	0.005 ± 0.003
	1242.8040	[357, 446]	< 13.03	0.004 ± 0.004
			< 11.96	
Si IV	1260.4221	[357, 446]	< 11.96	0.001 ± 0.004
	1526.7066	[357, 446]	< 12.92	0.001 ± 0.007
			12.57 ± 0.08	
	1393.7550	[357, 446]	12.57 ± 0.08	0.032 ± 0.006
	1402.7700	[357, 446]	< 12.59	0.009 ± 0.006

^a Velocity interval for the AODM column density measurement. Velocities are relative to the redshift of the foreground quasar J1026+4614FG, $z_{\text{fg}} = 3.3401$.

TABLE 13
IONIC COLUMN DENSITIES FOR J1038+5027FG

Ion	λ_{rest} (Å)	v_{int}^a (km s ⁻¹)	$\log N_{\text{AODM}}$	Rest EW (Å)
A				
C II	1334.5323	[466, 676]	< 13.38	-0.011 ± 0.016
C II*			< 13.38	
C IV	1335.7077	[536, 676]	< 13.35	0.016 ± 0.013
			< 13.35	
			14.08 ± 0.03	
Si II	1548.1950	[466, 676]	14.08 ± 0.03	0.364 ± 0.019
	1550.7700	[466, 676]	14.09 ± 0.04	0.211 ± 0.019
			< 13.39	
Si IV	1526.7066	[466, 676]	< 13.39	0.029 ± 0.021
	1808.0130	[466, 676]	< 15.17	0.044 ± 0.029
			13.00 ± 0.10	
	1393.7550	[466, 676]	13.00 ± 0.10	0.079 ± 0.019
	1402.7700	[466, 676]	< 13.13	-0.023 ± 0.021

^a Velocity interval for the AODM column density measurement. Velocities are relative to the redshift of the foreground quasar J1038+5027FG, $z_{\text{fg}} = 3.1323$.

TABLE 14
IONIC COLUMN DENSITIES FOR J1144+0959FG

Ion	λ_{rest} (Å)	v_{int}^a (km s ⁻¹)	$\log N_{\text{AODM}}$	Rest EW (Å)
A				
C II	1334.5323	[-1690, -1605]	< 12.72	-0.004 ± 0.004
C III			< 12.72	
C IV	977.0200	[-1690, -1605]	> 13.66	0.157 ± 0.005
			> 13.66	
			13.98 ± 0.03	
Si II	1548.1950	[-1690, -1605]	13.92 ± 0.03	0.196 ± 0.002
	1550.7700	[-1690, -1605]	14.09 ± 0.03	0.169 ± 0.003
			< 12.53	
Si IV	1526.7066	[-1690, -1605]	< 12.53	0.007 ± 0.003
			< 12.08	
	1393.7550	[-1690, -1605]	< 12.08	-0.002 ± 0.004
	1402.7700	[-1690, -1605]	< 12.31	0.002 ± 0.003
B				
C II	1334.5323	[-1352, -1192]	13.15 ± 0.07	0.025 ± 0.005
C IV			13.15 ± 0.07	
Si II	1548.1950	[-1352, -1192]	14.25 ± 0.03	0.411 ± 0.003
	1550.7700	[-1352, -1192]	> 14.24	0.267 ± 0.004
			14.25 ± 0.03	
Si III	1260.4221	[-1352, -1192]	< 12.04	0.006 ± 0.005
	1526.7066	[-1352, -1192]	< 12.92	-0.046 ± 0.009
			< 13.54	

TABLE 14 — *Continued*

Ion	λ_{rest} (Å)	v_{int}^a (km s ^{−1})	log N_{AODM}	Rest EW (Å)
Si IV	1206.5000	[−1317, −1192]	< 13.54	0.347 ± 0.003
	1393.7550	[−1352, −1192]	13.21 ± 0.03	0.119 ± 0.005
	1402.7700	[−1352, −1192]	13.20 ± 0.03	0.065 ± 0.005
C				
C II	1334.5323	[−1192, −1142]	13.27 ± 0.04	0.030 ± 0.003
C IV			13.27 ± 0.04	
Si II	1550.7700	[−1192, −1142]	13.03 ± 0.07	0.020 ± 0.003
	1260.4221	[−1192, −1142]	12.48 ± 0.04	0.033 ± 0.003
Si III	1526.7066	[−1192, −1142]	12.48 ± 0.04	0.009 ± 0.004
	1206.5000	[−1192, −1142]	< 12.60	0.147 ± 0.002
Si IV	1393.7550	[−1192, −1142]	< 13.14	0.021 ± 0.004
	1402.7700	[−1192, −1142]	< 13.14	
	1402.7700	[−1192, −1142]	12.41 ± 0.06	
	1393.7550	[−1192, −1142]	12.44 ± 0.08	0.010 ± 0.002
	1402.7700	[−1192, −1142]	12.37 ± 0.10	
D				
C II	1334.5323	[−1070, −870]	13.47 ± 0.04	0.053 ± 0.005
C II*			13.47 ± 0.04	
C IV	1335.7077	[−1070, −870]	< 12.97	0.010 ± 0.005
	1548.1950	[−1070, −870]	< 12.97	0.248 ± 0.004
	1550.7700	[−1070, −870]	13.86 ± 0.03	
Si II	1526.7066	[−1070, −870]	13.88 ± 0.03	0.121 ± 0.004
	1526.7066	[−1070, −870]	13.82 ± 0.03	0.007 ± 0.004
Si IV	1393.7550	[−1070, −870]	< 12.71	
	1402.7700	[−1070, −870]	< 12.71	0.118 ± 0.005
	1402.7700	[−1070, −870]	13.16 ± 0.03	
	1393.7550	[−1070, −870]	13.17 ± 0.03	0.058 ± 0.005
	1402.7700	[−1070, −870]	13.14 ± 0.03	
E				
C II	1334.5323	[−145, −70]	12.84 ± 0.10	0.013 ± 0.003
C IV			12.84 ± 0.10	
Al II	1548.1950	[−145, −70]	13.67 ± 0.03	0.130 ± 0.002
	1550.7700	[−145, −70]	13.66 ± 0.03	
	1670.7874	[−145, −70]	13.70 ± 0.03	0.083 ± 0.002
Al III	1862.7895	[−145, −70]	11.24 ± 0.14	0.008 ± 0.002
	1862.7895	[−145, −70]	11.24 ± 0.14	
Si II	1526.7066	[−145, −70]	< 12.21	0.013 ± 0.003
	1526.7066	[−145, −70]	< 12.21	
Si IV	1393.7550	[−145, −70]	< 12.51	−0.002 ± 0.003
	1402.7700	[−145, −70]	< 12.51	
	1402.7700	[−145, −70]	12.88 ± 0.03	
Fe II	1608.4511	[−145, −70]	12.88 ± 0.03	0.058 ± 0.003
	1608.4511	[−145, −70]	12.88 ± 0.04	0.031 ± 0.003
	1608.4511	[−145, −70]	< 12.65	0.005 ± 0.002
1608.4511	[−145, −70]	< 12.65		
F				
C II	1334.5323	[−73, 62]	> 14.24	0.168 ± 0.004
C II*			> 14.24	
C IV	1335.7077	[−73, 62]	< 12.86	0.009 ± 0.004
	1548.1950	[−73, 62]	< 12.86	
	1550.7700	[−73, 62]	> 14.73	0.519 ± 0.003
O I	1302.1685	[−73, 22]	> 14.55	
	1302.1685	[−73, 22]	> 14.73	0.456 ± 0.002
Al II	1670.7874	[−73, 62]	13.16 ± 0.13	0.009 ± 0.003
	1670.7874	[−73, 62]	13.16 ± 0.13	
Al III	1862.7895	[−73, 62]	12.52 ± 0.03	0.094 ± 0.003
	1862.7895	[−73, 62]	12.52 ± 0.03	
Si II	1190.4158	[−23, 62]	13.06 ± 0.03	0.073 ± 0.004
	1260.4221	[−48, 57]	13.07 ± 0.03	
	1304.3702	[−73, 62]	13.91 ± 0.03	0.096 ± 0.003
Si IV	1526.7066	[−73, 62]	> 13.81	
	1808.0130	[−73, 62]	> 13.41	0.174 ± 0.003
	1808.0130	[−73, 62]	14.03 ± 0.03	0.101 ± 0.004
			13.85 ± 0.03	0.100 ± 0.004
			< 15.00	0.048 ± 0.004
			> 13.92	

TABLE 14 — *Continued*

Ion	λ_{rest} (Å)	v_{int}^a (km s ⁻¹)	$\log N_{\text{AODM}}$	Rest EW (Å)
Fe II	1393.7550	[−73, 62]	> 13.74	0.255 ± 0.004
	1402.7700	[−73, 62]	> 13.92	0.196 ± 0.004
			13.25 ± 0.05	
	1608.4511	[−73, 22]	13.25 ± 0.05	0.021 ± 0.002

^a Velocity interval for the AODM column density measurement. Velocities are relative to the redshift of the foreground quasar J1144+0959FG, $z_{\text{fg}} = 2.9731$.

TABLE 15
IONIC COLUMN DENSITIES FOR J1145+0322FG

Ion	λ_{rest} (Å)	v_{int}^a (km s ⁻¹)	$\log N_{\text{AODM}}$	Rest EW (Å)
A				
C II			> 14.71	
C II*	1334.5323	[−278, 122]	> 14.71	0.504 ± 0.022
			< 13.61	
C IV	1335.7077	[−258, 122]	< 13.61	0.055 ± 0.024
			> 14.59	
	1548.1950	[−278, 122]	> 14.55	0.777 ± 0.028
	1550.7700	[−278, 122]	> 14.59	0.523 ± 0.029
O I			14.08 ± 0.14	
Mg I	1302.1685	[−278, 72]	14.08 ± 0.14	0.083 ± 0.027
			< 11.98	
Mg II	2852.9642	[−278, 122]	< 11.98	0.077 ± 0.041
			> 13.72	
	2796.3520	[−278, 122]	> 13.53	0.859 ± 0.029
	2803.5310	[−278, 122]	> 13.72	0.758 ± 0.034
Al II			12.73 ± 0.05	
Al III	1670.7874	[−278, 122]	12.73 ± 0.05	0.204 ± 0.023
			12.92 ± 0.06	
	1854.7164	[−278, 122]	12.90 ± 0.07	0.120 ± 0.019
	1862.7895	[−278, 122]	13.00 ± 0.11	0.078 ± 0.020
Si II			13.97 ± 0.05	
	1190.4158	[−278, 122]	< 14.19	0.371 ± 0.069
	1260.4221	[−278, 122]	> 13.82	0.496 ± 0.043
	1304.3702	[−278, 122]	< 14.41	0.315 ± 0.025
Si III	1526.7066	[−278, 122]	13.97 ± 0.05	0.201 ± 0.025
			> 13.77	
Si IV	1206.5000	[−278, 122]	> 13.77	0.602 ± 0.092
			13.74 ± 0.03	
Fe II	1393.7550	[−278, 122]	13.70 ± 0.03	0.320 ± 0.025
	1402.7700	[−278, 122]	13.84 ± 0.04	0.256 ± 0.024
			13.53 ± 0.09	
	1608.4511	[−278, 122]	< 13.69	0.045 ± 0.021
	2344.2140	[−278, 122]	13.53 ± 0.09	0.178 ± 0.039
	2374.4612	[−278, 122]	< 13.84	0.043 ± 0.036
	2586.6500	[−278, 122]	< 13.68	0.189 ± 0.036

^a Velocity interval for the AODM column density measurement. Velocities are relative to the redshift of the foreground quasar J1145+0322FG, $z_{\text{fg}} = 1.7652$.

TABLE 16
IONIC COLUMN DENSITIES FOR J1204+0221FG

Ion	λ_{rest} (Å)	v_{int}^a (km s ⁻¹)	$\log N_{\text{AODM}}$	Rest EW (Å)
A				
C II			> 14.63	
	1036.3367	[57, 207]	> 14.63	0.248 ± 0.009
C IV	1334.5323	[77, 247]	> 14.58	0.363 ± 0.005
			13.60 ± 0.03	
N I	1548.1950	[77, 247]	13.60 ± 0.03	0.141 ± 0.007
			13.34 ± 0.05	
	1199.5496	[107, 207]	13.33 ± 0.05	0.032 ± 0.004

TABLE 16 — *Continued*

Ion	λ_{rest} (Å)	v_{int}^a (km s ⁻¹)	$\log N_{\text{AODM}}$	Rest EW (Å)
N II	1083.9900	[77, 247]	> 14.45	0.166 ± 0.005
N V	1242.8040	[107, 187]	> 14.45 < 13.10	0.013 ± 0.001
O I	1039.2304	[107, 167]	14.36 ± 0.04 14.55 ± 0.06	0.023 ± 0.004
O VI	1302.1685	[77, 247]	14.32 ± 0.05 < 13.67	0.081 ± 0.007
Al II	1031.9261	[87, 167]	< 13.67 < 13.67	0.050 ± 0.006
Al III	1670.7874	[87, 207]	> 12.74 < 12.41	0.151 ± 0.006
Si II	1854.7164	[87, 207]	< 12.41 13.89 ± 0.03	0.038 ± 0.011
Si II*	1190.4158	[87, 207]	> 13.88	0.139 ± 0.004
Si III	1260.4221	[57, 217]	> 13.60	0.262 ± 0.003
Si IV	1526.7066	[107, 207]	13.89 ± 0.03 < 11.93	0.116 ± 0.005
Fe II	1264.7377	[57, 217]	< 11.93 > 13.66	0.007 ± 0.004
Fe III	1206.5000	[57, 237]	> 13.66 12.93 ± 0.03	0.441 ± 0.004
Fe II	1393.7550	[77, 207]	12.90 ± 0.03	0.065 ± 0.005
Fe III	1402.7700	[77, 207]	13.03 ± 0.05 13.34 ± 0.10	0.046 ± 0.005
Fe II	1608.4511	[107, 187]	13.34 ± 0.10 < 13.37	0.025 ± 0.006
Fe III	1122.5260	[87, 187]	< 13.37	-0.000 ± 0.005
B				
C II	1036.3367	[269, 519]	> 15.24 > 15.24	0.779 ± 0.008
C IV	1334.5323	[309, 519]	> 15.10 14.09 ± 0.03	0.889 ± 0.004
N I	1548.1950	[309, 519]	14.11 ± 0.03	0.382 ± 0.007
N II	1550.7700	[309, 519]	14.06 ± 0.03	0.195 ± 0.008
N V	1199.5496	[269, 449]	> 14.01 > 14.01	0.143 ± 0.005
N II	1083.9900	[269, 519]	> 15.10 > 15.10	0.589 ± 0.005
N V	1242.8040	[309, 519]	< 13.81 < 13.81	0.065 ± 0.002
O I	1039.2304	[309, 519]	15.61 ± 0.03 15.61 ± 0.03	0.225 ± 0.006
O VI	1302.1685	[269, 529]	> 15.35 < 14.58	0.692 ± 0.007
Al II	1031.9261	[309, 519]	< 14.58 < 14.58	0.308 ± 0.010
Al III	1670.7874	[269, 519]	13.32 ± 0.03 13.32 ± 0.03	0.619 ± 0.009
Si II	1854.7164	[369, 519]	12.68 ± 0.08 12.68 ± 0.08	0.068 ± 0.014
Si II*	1304.3702	[269, 519]	14.60 ± 0.03 14.64 ± 0.03	0.416 ± 0.009
Si III	1526.7066	[269, 519]	14.58 ± 0.03 < 14.65	0.582 ± 0.008
Si IV	1808.0130	[319, 419]	< 12.04 < 12.04	0.005 ± 0.009
Fe II	1264.7377	[269, 529]	< 12.04 > 14.02	-0.002 ± 0.005
Fe III	1206.5000	[269, 529]	> 14.02 13.50 ± 0.03	0.823 ± 0.004
Fe II	1393.7550	[309, 519]	13.50 ± 0.03 13.50 ± 0.03	0.234 ± 0.006
Fe III	1402.7700	[309, 519]	13.50 ± 0.03 13.87 ± 0.04	0.128 ± 0.007
Fe II	1608.4511	[319, 469]	13.87 ± 0.04 13.87 ± 0.04	0.088 ± 0.008
Fe III	1122.5260	[319, 419]	< 13.35 < 13.35	0.008 ± 0.004
C				
C II	1036.3367	[618, 718]	> 14.79 > 14.79	0.281 ± 0.004
C II*	1334.5323	[588, 748]	> 14.67 13.62 ± 0.03	0.364 ± 0.004
C II*	1335.7077	[588, 748]	13.62 ± 0.03	0.061 ± 0.005

TABLE 16 — *Continued*

Ion	λ_{rest} (Å)	v_{int}^a (km s ⁻¹)	$\log N_{\text{AODM}}$	Rest EW (Å)
C IV	1548.1950	[588, 748]	13.66 ± 0.03	
	1550.7700	[588, 748]	13.71 ± 0.03	0.158 ± 0.007
N I			13.48 ± 0.06	0.051 ± 0.008
	1134.9803	[638, 718]	14.29 ± 0.03	
	1199.5496	[618, 748]	14.13 ± 0.04	0.049 ± 0.004
N II			14.33 ± 0.03	0.213 ± 0.004
	1083.9900	[618, 748]	> 14.80	
N V			> 14.80	0.272 ± 0.004
	1242.8040	[638, 738]	< 12.58	
O I			< 12.58	-0.000 ± 0.001
	1039.2304	[618, 718]	> 15.25	
	1302.1685	[588, 748]	> 15.25	0.088 ± 0.004
O VI			> 14.97	0.284 ± 0.007
	1031.9261	[698, 838]	< 13.70	
Al II			< 13.70	0.054 ± 0.009
	1670.7874	[618, 738]	12.79 ± 0.03	
Al III			12.79 ± 0.03	0.181 ± 0.007
	1854.7164	[668, 738]	< 12.28	
Si II			< 12.28	0.001 ± 0.010
	1190.4158	[618, 748]	> 14.14	
	1526.7066	[618, 738]	> 14.14	0.225 ± 0.004
	1808.0130	[618, 738]	> 14.08	0.170 ± 0.006
Si II*			< 14.66	-0.012 ± 0.010
	1264.7377	[648, 748]	< 11.82	
Si III			< 11.82	-0.002 ± 0.003
	1206.5000	[648, 748]	> 13.59	
Si IV			> 13.59	0.339 ± 0.003
	1393.7550	[618, 738]	12.79 ± 0.04	
	1402.7700	[618, 738]	12.74 ± 0.05	0.039 ± 0.006
Fe II			12.90 ± 0.07	0.032 ± 0.005
	1608.4511	[618, 738]	13.57 ± 0.07	
Fe III			13.57 ± 0.07	0.045 ± 0.007
	1122.5260	[698, 798]	< 13.37	
			< 13.37	-0.001 ± 0.005

^a Velocity interval for the AODM column density measurement. Velocities are relative to the redshift of the foreground quasar J1204+0221FG, $z_{\text{fg}} = 2.4358$.

TABLE 17
IONIC COLUMN DENSITIES FOR J1420+1603FG

Ion	λ_{rest} (Å)	v_{int}^a (km s ⁻¹)	$\log N_{\text{AODM}}$	Rest EW (Å)
A				
C II			< 13.65	
	1334.5323	[-543, -305]	< 13.65	0.083 ± 0.027
C IV			13.63 ± 0.04	
	1548.1950	[-543, -305]	13.63 ± 0.04	0.155 ± 0.014
N V			< 13.56	
	1238.8210	[-543, -305]	< 13.56	0.008 ± 0.026
	1242.8040	[-543, -305]	< 13.92	0.011 ± 0.030
O I			< 14.01	
	1302.1685	[-543, -305]	< 14.01	0.032 ± 0.024
Mg I			< 11.84	
	2852.9642	[-543, -305]	< 11.83	0.028 ± 0.029
Mg II			< 12.61	
	2796.3520	[-543, -305]	< 12.61	0.029 ± 0.055
Al II			< 12.01	
	1670.7874	[-543, -305]	< 12.01	0.029 ± 0.016
Al III			< 12.45	
	1854.7164	[-543, -305]	< 12.45	-0.032 ± 0.016
	1862.7895	[-543, -305]	< 12.75	-0.043 ± 0.016
Si II			< 12.66	
	1260.4221	[-543, -305]	< 12.66	0.046 ± 0.021
	1526.7066	[-543, -305]	< 13.42	0.010 ± 0.023
Si IV			12.87 ± 0.14	
	1393.7550	[-543, -305]	12.87 ± 0.14	0.061 ± 0.020
	1402.7700	[-543, -305]	< 13.18	-0.016 ± 0.023
Fe II			< 12.81	
	1608.4511	[-543, -305]	< 13.56	0.002 ± 0.016

TABLE 17 — *Continued*

Ion	λ_{rest} (Å)	v_{int}^a (km s ⁻¹)	$\log N_{\text{AODM}}$	Rest EW (Å)
Fe III	2344.2140	[−543, −305]	< 13.37	0.125 ± 0.022
	2374.4612	[−543, −305]	< 13.74	0.031 ± 0.028
	2382.7650	[−543, −305]	< 13.08	0.178 ± 0.029
	2586.6500	[−543, −305]	< 13.37	−0.002 ± 0.031
	2600.1729	[−543, −305]	< 12.81	−0.025 ± 0.031
	1122.5260	[−543, −305]	< 14.60	0.035 ± 0.071
B				
C II			> 14.44	
C IV	1334.5323	[−305, −84]	> 14.44	0.341 ± 0.023
			< 13.83	
N V	1548.1950	[−305, −84]	< 13.83	0.239 ± 0.013
			< 13.60	
O I	1238.8210	[−305, −84]	< 13.60	0.031 ± 0.028
	1242.8040	[−305, −84]	< 13.91	−0.004 ± 0.029
Mg I	1302.1685	[−305, −84]	< 14.01	
			< 14.01	0.055 ± 0.024
Mg II	2852.9642	[−305, −84]	< 11.81	
			< 11.81	0.072 ± 0.027
Al II	2796.3520	[−305, −84]	> 13.24	
			> 13.24	0.523 ± 0.030
Al III	1670.7874	[−305, −84]	12.60 ± 0.04	
			12.60 ± 0.04	0.152 ± 0.014
Si II	1854.7164	[−305, −84]	< 12.43	
	1862.7895	[−305, −84]	< 12.43	−0.003 ± 0.015
Si III			< 12.73	−0.018 ± 0.015
			13.49 ± 0.12	
Si IV	1260.4221	[−305, −84]	> 13.44	0.281 ± 0.018
	1526.7066	[−305, −84]	13.49 ± 0.12	0.073 ± 0.021
Fe II	1808.0130	[−305, −84]	< 14.94	−0.015 ± 0.018
			> 13.31	
Fe III	1206.5000	[−305, −124]	> 13.31	0.302 ± 0.024
			13.27 ± 0.06	
Fe II	1393.7550	[−305, −84]	13.27 ± 0.06	0.149 ± 0.019
	1402.7700	[−305, −84]	< 13.18	0.032 ± 0.022
Fe III			< 12.79	
	1608.4511	[−305, −84]	< 13.54	−0.008 ± 0.016
Fe II	2344.2140	[−305, −84]	< 13.42	0.137 ± 0.021
	2374.4612	[−305, −84]	< 13.73	0.048 ± 0.027
Fe III	2382.7650	[−305, −84]	< 13.19	0.220 ± 0.028
	2586.6500	[−305, −84]	< 13.27	0.047 ± 0.025
Fe II	2600.1729	[−305, −84]	< 12.79	0.072 ± 0.029
			< 14.54	
Fe III	1122.5260	[−305, −84]	< 14.54	0.010 ± 0.066
C				
C II			> 14.44	
C IV	1334.5323	[−84, 183]	> 14.44	0.328 ± 0.026
			> 14.23	
N V	1548.1950	[−84, 183]	> 14.23	0.398 ± 0.013
			< 13.62	
O I	1238.8210	[−84, 183]	< 13.62	−0.016 ± 0.030
	1242.8040	[−84, 183]	< 13.95	0.021 ± 0.031
Mg I	1302.1685	[−84, 183]	14.38 ± 0.07	
			14.38 ± 0.07	0.159 ± 0.025
Mg II	2852.9642	[−84, 183]	< 11.90	
			< 11.90	0.070 ± 0.033
Al II	2796.3520	[−84, 183]	> 13.51	
	2803.5310	[−84, 183]	> 13.16	0.435 ± 0.032
Al III			> 13.51	0.525 ± 0.046
			12.42 ± 0.06	
Si II	1670.7874	[−84, 183]	12.42 ± 0.06	0.107 ± 0.015
			< 12.47	
Si III	1854.7164	[−84, 183]	< 12.47	0.010 ± 0.016
	1862.7895	[−84, 183]	< 12.77	−0.032 ± 0.016
Si IV			13.87 ± 0.06	
			> 13.35	0.238 ± 0.020
Fe II	1260.4221	[−84, 183]	13.87 ± 0.06	0.160 ± 0.022
	1526.7066	[−84, 183]	13.57 ± 0.07	
Fe III	1393.7550	[−84, 183]	> 13.46	0.204 ± 0.021
	1402.7700	[−84, 183]	13.57 ± 0.07	0.147 ± 0.024
Fe II			< 12.94	

TABLE 17 — *Continued*

Ion	λ_{rest} (Å)	v_{int}^a (km s ⁻¹)	$\log N_{\text{AODM}}$	Rest EW (Å)
Fe III	1608.4511	[−84, 183]	< 13.58	−0.005 ± 0.017
	2344.2140	[−84, 183]	< 13.38	0.129 ± 0.024
	2374.4612	[−84, 183]	< 13.98	0.142 ± 0.030
	2382.7650	[−84, 183]	< 13.29	0.290 ± 0.030
	2586.6500	[−84, 183]	< 13.37	0.004 ± 0.032
	2600.1729	[−84, 183]	< 12.94	0.040 ± 0.041
	1122.5260	[−84, 183]	< 14.60	0.017 ± 0.070
D				
C II	1334.5323	[184, 428]	> 14.91	0.756 ± 0.020
C IV	1548.1950	[184, 428]	> 14.57	0.815 ± 0.010
	1238.8210	[184, 428]	< 13.62	−0.004 ± 0.029
N V	1242.8040	[184, 428]	< 13.94	0.021 ± 0.030
	1302.1685	[184, 428]	> 15.01	0.456 ± 0.022
Mg I	2852.9642	[184, 428]	12.33 ± 0.07	0.255 ± 0.039
Mg II	2796.3520	[184, 428]	> 13.97	1.500 ± 0.033
	2803.5310	[184, 428]	> 13.97	1.149 ± 0.026
Al II	1670.7874	[184, 428]	> 13.29	0.557 ± 0.012
Al III	1854.7164	[184, 428]	12.87 ± 0.06	0.103 ± 0.015
	1862.7895	[184, 428]	< 12.75	0.010 ± 0.015
	1260.4221	[184, 428]	14.35 ± 0.03	0.673 ± 0.016
Si II	1526.7066	[184, 428]	14.35 ± 0.03	0.423 ± 0.019
	1808.0130	[184, 428]	< 15.35	0.127 ± 0.018
	1206.5000	[184, 428]	> 14.03	0.933 ± 0.021
Si III	1393.7550	[184, 428]	> 13.92	0.492 ± 0.019
	1402.7700	[184, 428]	14.02 ± 0.03	0.354 ± 0.021
Fe II	1608.4511	[184, 428]	13.76 ± 0.03	0.068 ± 0.016
	2344.2140	[184, 428]	13.73 ± 0.10	0.345 ± 0.022
	2374.4612	[184, 428]	13.85 ± 0.03	0.356 ± 0.029
	2382.7650	[184, 428]	< 14.40	0.692 ± 0.028
	2586.6500	[184, 428]	13.77 ± 0.03	0.692 ± 0.028
	2600.1729	[184, 428]	13.82 ± 0.05	0.240 ± 0.027
Fe III	1122.5260	[184, 428]	13.70 ± 0.03	0.544 ± 0.033
			< 14.59	0.141 ± 0.063
E				
C II	1334.5323	[428, 650]	> 14.86	0.650 ± 0.019
C IV	1550.7700	[428, 650]	> 14.86	0.391 ± 0.011
	1238.8210	[428, 650]	14.39 ± 0.03	0.021 ± 0.028
N V	1242.8040	[428, 650]	14.39 ± 0.03	0.011 ± 0.028
	1302.1685	[428, 650]	< 13.61	0.174 ± 0.024
O I	1302.1685	[428, 650]	< 13.61	0.174 ± 0.024
Mg I	2852.9642	[428, 650]	< 14.44	0.115 ± 0.042
	2852.9642	[428, 650]	< 12.01	0.115 ± 0.042
Mg II	2803.5310	[428, 650]	< 12.01	0.115 ± 0.042
	2803.5310	[428, 650]	> 13.70	0.727 ± 0.026
Al II	1670.7874	[428, 650]	> 13.70	0.254 ± 0.013
Al III	1854.7164	[428, 650]	12.82 ± 0.03	0.073 ± 0.015
	1862.7895	[428, 650]	12.83 ± 0.03	0.008 ± 0.015
	1862.7895	[428, 650]	12.67 ± 0.09	0.008 ± 0.015
Si II	1260.4221	[428, 650]	12.67 ± 0.09	0.424 ± 0.017
	1304.3702	[428, 650]	< 12.73	0.176 ± 0.025
	1526.7066	[428, 650]	13.93 ± 0.04	0.167 ± 0.019
	1808.0130	[428, 650]	> 13.66	−0.045 ± 0.018
Si III			14.15 ± 0.07	0.167 ± 0.019
			13.89 ± 0.05	−0.045 ± 0.018

TABLE 17 — *Continued*

Ion	λ_{rest} (Å)	v_{int}^a (km s ⁻¹)	$\log N_{\text{AODM}}$	Rest EW (Å)
Si IV	1206.5000	[428, 650]	> 13.84 13.52 ± 0.03	0.636 ± 0.022
	1393.7550	[428, 650]	13.51 ± 0.04	0.246 ± 0.019
	1402.7700	[428, 650]	13.57 ± 0.07	0.148 ± 0.023
Fe II			13.41 ± 0.03	
	1608.4511	[428, 650]	< 13.57	0.045 ± 0.016
	2344.2140	[428, 650]	13.45 ± 0.07	0.142 ± 0.022
	2374.4612	[428, 650]	< 13.98	0.139 ± 0.028
	2382.7650	[428, 650]	13.48 ± 0.03	0.390 ± 0.028
	2586.6500	[428, 650]	< 13.49	0.075 ± 0.037
	2600.1729	[428, 650]	13.29 ± 0.06	0.245 ± 0.030
Fe III			< 14.69	
	1122.5260	[428, 650]	< 14.69	0.200 ± 0.061
F				
C II			13.97 ± 0.06	
C II*	1334.5323	[651, 808]	13.97 ± 0.06	0.154 ± 0.019
			14.06 ± 0.05	
C IV	1335.7077	[651, 808]	14.06 ± 0.05	0.164 ± 0.019
			14.12 ± 0.03	
N V	1550.7700	[651, 808]	14.12 ± 0.03	0.208 ± 0.009
			< 13.53	
	1238.8210	[651, 808]	< 13.53	-0.009 ± 0.024
O I	1242.8040	[651, 808]	< 13.82	0.007 ± 0.023
			< 14.45	
	1302.1685	[651, 808]	< 14.45	0.160 ± 0.022
Mg I			< 11.95	
	2852.9642	[651, 808]	< 11.95	0.035 ± 0.038
Mg II			12.82 ± 0.04	
	2796.3520	[651, 808]	12.80 ± 0.05	0.242 ± 0.026
	2803.5310	[651, 808]	12.87 ± 0.07	0.146 ± 0.024
Al II			11.98 ± 0.12	
Al III	1670.7874	[651, 808]	11.98 ± 0.12	0.043 ± 0.012
			< 12.36	
	1854.7164	[651, 808]	< 12.36	-0.002 ± 0.013
Si II	1862.7895	[651, 808]	< 12.68	-0.006 ± 0.013
			13.00 ± 0.06	
	1260.4221	[651, 808]	13.00 ± 0.06	0.126 ± 0.018
	1304.3702	[651, 808]	< 13.72	0.027 ± 0.024
	1526.7066	[651, 808]	< 13.28	0.018 ± 0.016
Si II*			< 12.62	
	1264.7377	[651, 808]	< 12.62	0.021 ± 0.017
Si III			13.04 ± 0.06	
	1206.5000	[651, 808]	13.04 ± 0.06	0.179 ± 0.021
Si IV			12.94 ± 0.11	
	1393.7550	[651, 808]	12.94 ± 0.11	0.070 ± 0.017
	1402.7700	[651, 808]	< 13.12	0.033 ± 0.019
Fe II			< 12.69	
	1608.4511	[651, 808]	< 13.49	-0.021 ± 0.014
	2344.2140	[651, 808]	< 13.02	0.010 ± 0.019
	2374.4612	[651, 808]	< 14.22	0.231 ± 0.023
	2382.7650	[651, 808]	< 12.69	0.040 ± 0.026
	2586.6500	[651, 808]	< 13.22	-0.008 ± 0.023
	2600.1729	[651, 808]	< 12.77	-0.017 ± 0.028
Fe III			< 14.56	
	1122.5260	[651, 808]	< 14.56	0.166 ± 0.048

^a Velocity interval for the AODM column density measurement. Velocities are relative to the redshift of the foreground quasar J1420+1603FG, $z_{\text{fg}} = 2.0197$.

TABLE 18
IONIC COLUMN DENSITIES FOR J1427-0121FG

Ion	λ_{rest} (Å)	v_{int}^a (km s ⁻¹)	$\log N_{\text{AODM}}$	Rest EW (Å)
A				
C II			13.91 ± 0.03	
C IV	1334.5323	[183, 313]	13.91 ± 0.03	0.106 ± 0.006
			14.26 ± 0.03	

TABLE 18 — *Continued*

Ion	λ_{rest} (Å)	v_{int}^a (km s ⁻¹)	$\log N_{\text{AODM}}$	Rest EW (Å)
O I	1548.1950	[183, 313]	> 14.12	0.280 ± 0.011
	1550.7700	[183, 313]	14.26 ± 0.03	0.236 ± 0.011
Si II	1302.1685	[183, 313]	< 13.42	0.005 ± 0.006
	1260.4221	[183, 313]	12.73 ± 0.03	0.060 ± 0.004
Si III	1206.5000	[183, 313]	12.72 ± 0.03	0.158 ± 0.006
	1393.7550	[183, 313]	13.06 ± 0.03	0.052 ± 0.005
Si IV	1402.7700	[183, 313]	12.86 ± 0.04	0.031 ± 0.006
	2374.4612	[183, 313]	12.85 ± 0.04	0.052 ± 0.005
Fe II	2382.7650	[183, 313]	12.90 ± 0.08	0.031 ± 0.006
	2600.1729	[183, 313]	< 12.24	-0.000 ± 0.009
	2374.4612	[183, 313]	< 13.23	0.020 ± 0.009
	2382.7650	[183, 313]	< 12.24	0.014 ± 0.011
B				
C II	1334.5323	[316, 684]	14.03 ± 0.03	0.179 ± 0.010
C II*	1335.7077	[364, 484]	14.04 ± 0.03	0.007 ± 0.006
	1550.7700	[316, 684]	< 12.99	0.674 ± 0.018
C IV	1548.1950	[316, 684]	< 12.99	0.480 ± 0.019
	1550.7700	[316, 684]	14.52 ± 0.03	0.005 ± 0.006
O I	1302.1685	[364, 484]	< 13.40	0.005 ± 0.006
Si II	1260.4221	[316, 684]	< 13.40	0.090 ± 0.006
	1393.7550	[316, 684]	12.84 ± 0.03	0.088 ± 0.010
Si IV	1402.7700	[316, 684]	12.84 ± 0.03	0.054 ± 0.010
	2374.4612	[316, 684]	13.14 ± 0.05	-0.004 ± 0.016
Fe II	2382.7650	[316, 684]	13.12 ± 0.08	0.019 ± 0.016
	2600.1729	[316, 684]	13.16 ± 0.07	-0.022 ± 0.018
	2374.4612	[316, 684]	< 12.48	
C				
C II	1334.5323	[754, 834]	14.07 ± 0.03	0.130 ± 0.004
C II*	1335.7077	[754, 834]	14.07 ± 0.03	0.048 ± 0.004
	1550.7700	[754, 834]	13.50 ± 0.04	0.023 ± 0.009
C IV	1548.1950	[754, 834]	< 13.15	0.080 ± 0.005
	1550.7700	[754, 834]	< 13.15	0.054 ± 0.003
O I	1302.1685	[754, 834]	14.22 ± 0.03	0.034 ± 0.013
Si II	1260.4221	[754, 834]	14.22 ± 0.03	0.007 ± 0.004
	1526.7066	[754, 834]	12.73 ± 0.03	-0.004 ± 0.005
Si IV	1393.7550	[754, 834]	< 13.24	0.002 ± 0.009
	1402.7700	[754, 834]	< 12.16	0.009 ± 0.007
Fe II	2374.4612	[754, 834]	< 12.16	0.014 ± 0.008
	2382.7650	[754, 834]	< 12.52	
	2600.1729	[754, 834]	< 12.10	

^a Velocity interval for the AODM column density measurement. Velocities are relative to the redshift of the foreground quasar J1427-0121FG, $z_{\text{fg}} = 2.2736$.

TABLE 19
IONIC COLUMN DENSITIES FOR J1553+1921FG

Ion	λ_{rest} (Å)	v_{int}^a (km s ⁻¹)	$\log N_{\text{AODM}}$	Rest EW (Å)
A				
C II	1334.5323	[-62, 535]	> 14.92	0.950 ± 0.067
C II*	1335.7077	[166, 535]	> 14.92	-0.034 ± 0.052
			< 13.93	
			< 13.93	

TABLE 19 — *Continued*

Ion	λ_{rest} (Å)	v_{int}^a (km s ⁻¹)	$\log N_{\text{AODM}}$	Rest EW (Å)
C IV	1548.1950	[−62, 535]	14.57 ± 0.03	
	1550.7700	[−62, 535]	> 14.47	0.757 ± 0.036
O I	1302.1685	[−62, 535]	14.57 ± 0.03	0.566 ± 0.036
			> 15.05	
Mg I	2852.9642	[−62, 535]	> 15.05	0.436 ± 0.053
Mg II	2796.3520	[−62, 535]	12.46 ± 0.07	
	2803.5310	[−62, 535]	12.46 ± 0.07	0.320 ± 0.056
			> 14.09	
Al II	1670.7874	[−62, 535]	> 13.94	1.953 ± 0.070
			> 14.09	1.405 ± 0.055
Al III	1854.7164	[−62, 535]	> 13.36	
	1862.7895	[−62, 535]	> 13.36	0.633 ± 0.031
			> 13.36	
Si II	1190.4158	[−62, 535]	13.11 ± 0.07	0.188 ± 0.033
	1260.4221	[−62, 535]	13.11 ± 0.07	0.075 ± 0.033
	1304.3702	[−62, 535]	< 13.08	
	1526.7066	[−62, 535]	15.26 ± 0.14	
	1808.0130	[−62, 386]	> 14.68	0.749 ± 0.093
Si III			> 14.11	0.968 ± 0.032
			> 14.61	0.358 ± 0.055
			> 14.48	0.512 ± 0.055
			15.26 ± 0.14	0.110 ± 0.035
Si IV	1206.5000	[−62, 535]	> 14.03	
			> 14.03	1.199 ± 0.064
			13.82 ± 0.10	
Fe II	1393.7550	[−62, 535]	> 14.09	0.718 ± 0.049
	1402.7700	[−62, 535]	13.82 ± 0.10	0.188 ± 0.059
			14.02 ± 0.03	
	1608.4511	[−62, 535]	14.28 ± 0.06	0.222 ± 0.032
	2344.2140	[−62, 535]	13.91 ± 0.05	0.345 ± 0.044
	2374.4612	[−62, 535]	14.32 ± 0.07	0.292 ± 0.051
	2382.7650	[−62, 535]	> 14.03	1.184 ± 0.051
	2586.6500	[−62, 535]	14.09 ± 0.05	0.400 ± 0.058
	2600.1729	[−62, 535]	> 13.86	0.673 ± 0.056
Fe III			< 15.13	
	1122.5260	[−62, 535]	< 15.13	0.416 ± 0.197

^a Velocity interval for the AODM column density measurement. Velocities are relative to the redshift of the foreground quasar J1553+1921FG, $z_{\text{fg}} = 2.0098$.

TABLE 20
IONIC COLUMN DENSITIES FOR J1627+4605FG

Ion	λ_{rest} (Å)	v_{int}^a (km s ⁻¹)	$\log N_{\text{AODM}}$	Rest EW (Å)
A				
C II	1334.5323	[−828, −508]	< 13.17	
			< 13.17	0.008 ± 0.010
C IV	1548.1950	[−828, −358]	13.63 ± 0.04	
	1550.7700	[−828, −358]	13.67 ± 0.04	0.168 ± 0.017
			13.47 ± 0.11	0.056 ± 0.015
O I	1302.1685	[−828, −358]	< 13.53	
			< 13.53	-0.002 ± 0.008
Al II	1670.7874	[−828, −358]	< 12.06	
			< 12.06	-0.040 ± 0.018
Si II	1304.3702	[−828, −358]	< 13.25	
	1526.7066	[−828, −358]	< 13.25	-0.007 ± 0.008
			< 13.36	0.021 ± 0.020
Si IV			< 12.66	
	1393.7550	[−828, −358]	< 12.66	0.020 ± 0.014
	1402.7700	[−828, −358]	< 12.96	-0.009 ± 0.014

^a Velocity interval for the AODM column density measurement. Velocities are relative to the redshift of the foreground quasar J1627+4605FG, $z_{\text{fg}} = 3.8137$.

TABLE 21
H I COLUMN DENSITY MEASUREMENTS

Subsystem	Velocity Range (km s ⁻¹)	Adopted log N_{HI}^a	Component Centroid (km s ⁻¹)	Component log N_{HI}	Doppler b (km s ⁻¹)
J0225+0048 $z_{\text{fg}} = 2.7265$ $N_{\text{HI}}^{\text{total}} = 17.9$					
A	[-362, 88)	$17.5^{+1.0}_{-1.0}$	-217 ± 2 -59 ± 5 +33 ± 4	17.5 14.0 ± 0.2 14.1 ± 0.1	34 15 60
B	[88, 498)	$16.9^{+1.0}_{-1.0}$	+303 ± 2	16.9 ± 0.2	60
C	[498, 827)	$17.5^{+0.8}_{-0.8}$	+536 ± 7 +694 ± 2 +905 +1067	13.4 ± 0.1 17.5 13.6 ± 0.2 13.3 ± 0.2	15 37 59 ± 12 44 ± 16
J0341+0000 $z_{\text{fg}} = 2.1233$ $N_{\text{HI}}^{\text{total}} = 14.2$					
A	[-500, 200)	$14.2^{+0.2}_{-0.2}$	+264 ± 4 +395 ± 5	13.8 ± 0.1 13.9 ± 0.1	15 56 ± 8
J0409-0411 $z_{\text{fg}} = 1.7155$ $N_{\text{HI}}^{\text{total}} = 14.2$					
A	[-300, 400)	$14.2^{+0.2}_{-0.2}$	-1346 ± 6	14.2 ± 0.2	51 ± 9
J0853-0011 $z_{\text{fg}} = 2.4014$ $N_{\text{HI}}^{\text{total}} = 18.8$					
A	[-274, -60)	$16.8^{+0.6}_{-0.6}$	-163 ± 1	17.2 ± 0.4	22 ± 1
B	[-60, 203)	$18.6^{+0.2}_{-0.6}$	+47 ± 32 +102 ± 10	15.5 ± 0.4 18.4 ± 0.1	46 ± 12 15 ± 3
C	[203, 379)	$18.2^{+0.3}_{-0.6}$	+274 ± 1	18.3 ± 0.2	20
J0932+0925 $z_{\text{fg}} = 2.4170$ $N_{\text{HI}}^{\text{total}} = 15.7$					
A	[-245, 307)	$15.5^{+0.4}_{-0.4}$	-168 ± 1 +24 +146	15.4 ± 0.4 14.3 14.1	34 ± 4 55 45
B	[307, 675)	$15.1^{+0.3}_{-0.3}$	+325 +438 +519 ± 3	13.7 14.0 15.0 ± 0.1	40 40 58 ± 3
C	[675, 959)	$14.3^{+0.1}_{-0.1}$	+775 +911 +985	14.0 13.6 13.9	55 45 35
J1026+4614 $z_{\text{fg}} = 3.3401$ $N_{\text{HI}}^{\text{total}} = 15.5$					
A	[296, 450)	$15.4^{+0.2}_{-0.2}$	+208 ± 4 +308 ± 3	15.0 ± 0.1 15.0 ± 0.1	51 ± 2 20 ± 4
B	[450, 539)	$14.6^{+0.1}_{-0.1}$	+412 ± 2	14.6 ± 0.1	60
J1038+5027 $z_{\text{fg}} = 3.1323$ $N_{\text{HI}}^{\text{total}} = 16.6$					
A	[451, 701)	$16.6^{+0.5}_{-0.5}$	+517 ± 7 +671 ± 8	16.6 ± 1.4 14.3 ± 0.2	42 ± 23 29 ± 9
J1144+0959 $z_{\text{fg}} = 2.9731$ $N_{\text{HI}}^{\text{total}} = 18.8$					
A	[-1696, -1483)	$13.5^{+0.2}_{-0.2}$	-1674 ± 1 -1637 ± 5 -1600 ± 2 -1541 ± 12	13.2 ± 0.1 12.4 ± 0.1 12.8 ± 0.2 12.5 ± 0.2	21 ± 1 15 18 ± 3 38 ± 21

TABLE 21 — *Continued*

Subsystem	Velocity Range (km s ⁻¹)	Adopted log N_{HI}^a	Component Centroid (km s ⁻¹)	Component log N_{HI}	Doppler b (km s ⁻¹)
B	[-1483, -1195)	$18.1^{+0.2}_{-0.4}$	-1261	18.1 ± 0.2	48
C	[-1195, -1075)	$18.3^{+0.2}_{-0.4}$	-1169	18.3 ± 0.2	26
D	[-1075, -535)	$17.9^{+0.5}_{-0.5}$	-956 -801 \pm 2 -710 \pm 1 -585	17.7 ± 0.2 14.7 ± 0.1 15.2 ± 0.1 14.3 ± 0.1	37 ± 1 33 ± 2 48 ± 1 26
E	[-535, -68)	$15.6^{+0.2}_{-0.2}$	-513 \pm 1 -444 \pm 2 -259 \pm 2 -108	13.0 ± 0.1 13.2 ± 0.1 12.8 ± 0.2 15.8 ± 0.1	18 ± 2 38 ± 3 26 ± 3 15
F	[-68, 197)	$18.4^{+0.2}_{-0.4}$	-21 \pm 3 +26 \pm 5 +127 \pm 5	15.4 ± 0.1 18.3 ± 0.1 16.8 ± 0.3	60 15 ± 2 28 ± 1
J1145+0322 $z_{\text{fg}} = 1.7652$ $N_{\text{HI}}^{\text{total}} = 18.4$					
A	[-271, 119)	$18.4^{+0.4}_{-0.4}$	-75 \pm 4	18.4 ± 0.1	49 ± 2
J1204+0221 $z_{\text{fg}} = 2.4358$ $N_{\text{HI}}^{\text{total}} = 19.7$					
A	[67, 217)	$18.6^{+0.4}_{-0.4}$	+6 \pm 2 +144	13.7 ± 0.1 18.6 ± 0.1	25 ± 2 25
B	[217, 617)	$19.6^{+0.2}_{-0.2}$	+392	19.8 ± 0.1	40
C	[617, 767)	$18.6^{+0.4}_{-0.4}$	+687 +850 \pm 3 +971 \pm 1 +1071 +1297 \pm 4 +1513 \pm 2 +1626 \pm 1	18.6 ± 0.1 12.8 ± 0.1 13.5 ± 0.1 14.4 ± 0.1 12.7 ± 0.2 12.8 ± 0.1 13.0 ± 0.1	22 19 ± 5 30 ± 1 25 30 ± 6 29 ± 3 23 ± 2
J1420+1603 $z_{\text{fg}} = 2.0197$ $N_{\text{HI}}^{\text{total}} = 19.1$					
A	[-656, -420)	$15.8^{+1.0}_{-1.0}$	-343	16.0 ± 2.0	40 ± 28
B	[-420, -199)	$18.5^{+0.4}_{-0.4}$	-184	18.5 ± 0.1	37 ± 3
C	[-199, 69)	$18.0^{+0.6}_{-0.6}$	+93	17.4 ± 0.7	34 ± 40
D	[69, 313)	$18.6^{+0.4}_{-0.4}$	+272 +331	18.3 18.3	15 15
E	[313, 535)	$18.6^{+0.4}_{-0.4}$	+490	18.6	46 ± 1
F	[535, 693)	$17.5^{+1.0}_{-1.0}$	+718	17.5 ± 0.2	16 ± 2
J1427-0121 $z_{\text{fg}} = 2.2736$ $N_{\text{HI}}^{\text{total}} = 18.8$					
A	[172, 293)	$17.3^{+0.5}_{-1.0}$	+232	17.3 ± 0.1	15
B	[293, 739)	$18.3^{+0.2}_{-1.0}$	+321 +390 \pm 3 +455 \pm 3 +524 \pm 4 +568 \pm 1	13.2 ± 0.2 15.0 ± 0.4 18.3 ± 0.2 13.7 ± 0.2 14.7 ± 0.2	15 15 15 15 15
C	[739, 842)	$18.6^{+0.2}_{-1.0}$	+771 +803 +899 \pm 7 +979 \pm 1	17.1 ± 0.3 18.6 ± 0.1 14.3 ± 0.2 13.7 ± 0.1	15 15 41 ± 8 18 ± 1

TABLE 21 — *Continued*

Subsystem	Velocity Range (km s ⁻¹)	Adopted log N_{HI}^a	Component Centroid (km s ⁻¹)	Component log N_{HI}	Doppler b (km s ⁻¹)
J1553+1921 $z_{\text{fg}} = 2.0098$ $N_{\text{HI}}^{\text{total}} = 20.2$					
A	[-342, 258)	$20.2^{+0.1}_{-0.1}$	+323 ± 15	20.2 ± 0.1	15
J1627+4605 $z_{\text{fg}} = 3.8137$ $N_{\text{HI}}^{\text{total}} = 16.9$					
A	[-824, -356)	$16.9^{+0.8}_{-0.8}$	-862 ± 4 -704 ± 1 -535 ± 1 -401 ± 5	13.6 ± 0.1 16.6 ± 0.5 14.2 ± 0.1 13.5 ± 0.1	47 ± 6 34 ± 3 36 ± 2 60

^a The adopted N_{HI} values match approximately the middle of lower bounds from equivalent widths and upper bounds from wings of the Lyman series absorptions. The N_{HI} values of the individual components of a subsystem come from ALIS voigt profile modeling outputs, which serve as guides to our adopted N_{HI} for a subsystem. The two need not agree and ALIS tends to give biased high values.

REFERENCES

- Adelberger, K. L., Shapley, A. E., Steidel, C. C., Pettini, M., Erb, D. K., & Reddy, N. A. 2005a, *ApJ*, 629, 636
- Adelberger, K. L., Steidel, C. C., Pettini, M., Shapley, A. E., Reddy, N. A., & Erb, D. K. 2005b, *ApJ*, 619, 697
- Andreon, S. 2012, *A&A*, 546, A6
- Antonucci, R. 1993, *ARA&A*, 31, 473
- Arrigoni Battaia, F., Hennawi, J. F., Cantalupo, S., & Prochaska, J. X. 2016, *ArXiv e-prints*
- Arrigoni Battaia, F., Hennawi, J. F., Prochaska, J. X., & Cantalupo, S. 2015a, *ApJ*, 809, 163
- Arrigoni Battaia, F., Yang, Y., Hennawi, J. F., Prochaska, J. X., Matsuda, Y., Yamada, T., & Hayashino, T. 2015b, *ApJ*, 804, 26
- Asplund, M., Grevesse, N., Sauval, A. J., & Scott, P. 2009, *ARA&A*, 47, 481
- Baldi, A., Etti, S., Molendi, S., Balestra, I., Gastaldello, F., & Tozzi, P. 2012, *A&A*, 537, A142
- Behroozi, P. S., Wechsler, R. H., & Conroy, C. 2013, *ApJ*, 770, 57
- Bergeron, J., & Boisse, P. 1991, *Advances in Space Research*, 11, 241
- Boksenberg, A., & Sargent, W. L. W. 2014, *ArXiv e-prints*
- Borison, T. 2005, *AJ*, 130, 381
- Bovy, J., Hennawi, J. F., Hogg, D. W., Myers, A. D., Kirkpatrick, J. A., Schlegel, D. J., Ross, N. P., Sheldon, E. S., McGreer, I. D., Schneider, D. P., & Weaver, B. A. 2011, *ApJ*, 729, 141
- Bovy, J., Myers, A. D., Hennawi, J. F., Hogg, D. W., McMahon, R. G., Schiminovich, D., Sheldon, E. S., Brinkmann, J., Schneider, D. P., & Weaver, B. A. 2012, *ApJ*, 749, 41
- Bowen, D. V., Hennawi, J. F., Ménard, B., Chelouche, D., Inada, N., Oguri, M., Richards, G. T., Strauss, M. A., Vanden Berk, D. E., & York, D. G. 2006, *ApJ*, 645, L105
- Cai, Z., Fan, X., Noterdaeme, P., Wang, R., McGreer, I., Carithers, B., Bian, F., Miralda-Escudé, J., Finley, H., Pâris, I., Schneider, D. P., Zakamska, N. L., Ge, J., Petitjean, P., & Slosar, A. 2014, *ApJ*, 793, 139
- Cantalupo, S., Arrigoni-Battaia, F., Prochaska, J. X., Hennawi, J. F., & Madau, P. 2014, *Nature*, 506, 63
- Cantalupo, S., Lilly, S. J., & Haehnelt, M. G. 2012, *MNRAS*, 425, 1992
- Chen, H.-W., Helsby, J. E., Gauthier, J.-R., Shectman, S. A., Thompson, I. B., & Tinker, J. L. 2010, *ApJ*, 714, 1521
- Churchill, C. W., Kacprzak, G. G., Steidel, C. C., Spitler, L. R., Holtzman, J., Nielsen, N. M., & Trujillo-Gomez, S. 2012, *ApJ*, 760, 68
- Conroy, C., Graves, G. J., & van Dokkum, P. G. 2014, *ApJ*, 780, 33
- Cooke, R. J., Pettini, M., Jorgenson, R. A., Murphy, M. T., & Steidel, C. C. 2014, *ApJ*, 781, 31
- Cooksey, K. L., Kao, M. M., Simcoe, R. A., O'Meara, J. M., & Prochaska, J. X. 2013, *The Astrophysical Journal*, 763, 37
- Crichton, N. H. M., Bielby, R., Shanks, T., Infante, L., Bornancini, C. G., Bouché, N., Lambas, D. G., Lowenthal, J. D., Minniti, D., Morris, S. L., Padilla, N., Péroux, C., Petitjean, P., Theuns, T., Tummuangpak, P., Weilbacher, P. M., Wisotzki, L., & Worseck, G. 2011, *MNRAS*, 414, 28
- Crichton, N. H. M., Hennawi, J. F., & Prochaska, J. X. 2013, *ApJ*, 776, L18
- Crichton, N. H. M., Hennawi, J. F., Simcoe, R. A., Cooksey, K. L., Murphy, M. T., Fumagalli, M., Prochaska, J. X., & Shanks, T. 2015, *MNRAS*, 446, 18
- Croft, R. A. C. 2004, *ApJ*, 610, 642
- Dey, A., Bian, C., Soifer, B. T., Brand, K., Brown, M. J. I., Chaffee, F. H., Le Floch, E., Hill, G., Houck, J. R., Jannuzi, B. T., Rieke, M., Weedman, D., Brodwin, M., & Eisenhardt, P. 2005, *ApJ*, 629, 654
- D'Odorico, V., Bruscoli, M., Saitta, F., Fontanot, F., Viel, M., Cristiani, S., & Monaco, P. 2008, *MNRAS*, 389, 1727
- Elias, J. H., Joyce, R. R., Liang, M., Muller, G. P., Hileman, E. A., & George, J. R. 2006, in *Presented at the Society of Photo-Optical Instrumentation Engineers (SPIE) Conference, Vol. 6269, Ground-based and Airborne Instrumentation for Astronomy*. Edited by McLean, Ian S.; Iye, Masanori. Proceedings of the SPIE, Volume 6269, pp. 62694C (2006).
- Erb, D. K. 2008, *ApJ*, 674, 151
- Farina, E. P., Falomo, R., Decarli, R., Treves, A., & Kotilainen, J. K. 2013, *MNRAS*, 429, 1267
- Farina, E. P., Falomo, R., Scarpa, R., Decarli, R., Treves, A., & Kotilainen, J. K. 2014, *MNRAS*, 441, 886
- Faucher-Giguère, C.-A., Feldmann, R., Quataert, E., Keres, D., Hopkins, P. F., & Murray, N. 2016, *ArXiv e-prints*
- Faucher-Giguère, C.-A., Hopkins, P. F., Keres, D., Muratov, A. L., Quataert, E., & Murray, N. 2015, *MNRAS*, 449, 987
- Faucher-Giguère, C.-A., Lidz, A., Hernquist, L., & Zaldarriaga, M. 2008, *ApJ*, 688, 85
- Faucher-Giguère, C.-A., & Quataert, E. 2012, *MNRAS*, 425, 605
- Ferland, G. J., Porter, R. L., van Hoof, P. A. M., Williams, R. J. R., Abel, N. P., Lykins, M. L., Shaw, G., Henney, W. J., & Stancil, P. C. 2013, *RMxAA*, 49, 137
- Finley, H., Petitjean, P., Pâris, I., Noterdaeme, P., Brinkmann, J., Myers, A. D., Ross, N. P., Schneider, D. P., Bizyaev, D., Brewington, H., Ebelke, G., Malanushenko, E., Malanushenko, V., Oravetz, D., Pan, K., Simmons, A., & Snedden, S. 2013, *A&A*, 558, A111
- Fox, A. J., Prochaska, J. X., Ledoux, C., Petitjean, P., Wolfe, A. M., & Srianand, R. 2009, *A&A*, 503, 731
- Fu, H., & Stockton, A. 2007, *ApJ*, 666, 794
- Fumagalli, M., Hennawi, J. F., Prochaska, J. X., Kasen, D., Dekel, A., Ceverino, D., & Primack, J. 2014, *ApJ*, 780, 74
- Gabor, J. M., Davé, R., Oppenheimer, B. D., & Finlator, K. 2011, *MNRAS*, 417, 2676
- Gauthier, J.-R. 2013, *MNRAS*, 432, 1444

- Gonçalves, T. S., Steidel, C. C., & Pettini, M. 2008, *ApJ*, 676, 816
- Haardt, F., & Madau, P. 2012, *ApJ*, 746, 125
- Haiman, Z., & Hui, L. 2001, *ApJ*, 547, 27
- Hamann, F. 1998, *ApJ*, 500, 798
- Hennawi, J. F., Myers, A. D., Shen, Y., Strauss, M. A., Djorgovski, S. G., Fan, X., Glikman, E., Mahabal, A., Martin, C. L., Richards, G. T., Schneider, D. P., & Shankar, F. 2010, *ApJ*, 719, 1672
- Hennawi, J. F., & Prochaska, J. X. 2007, *ApJ*, 655, 735
- . 2013, *ApJ*, 766, 58
- Hennawi, J. F., Prochaska, J. X., Burles, S., Strauss, M. A., Richards, G. T., Schlegel, D. J., Fan, X., Schneider, D. P., Zakamska, N. L., Oguri, M., Gunn, J. E., Lupton, R. H., & Brinkmann, J. 2006a, *ApJ*, 651, 61
- Hennawi, J. F., Prochaska, J. X., Cantalupo, S., & Arrigoni-Battaia, F. 2015, *Science*, 348, 779
- Hennawi, J. F., Prochaska, J. X., Kollmeier, J., & Zheng, Z. 2009, *ApJ*, 693, L49
- Hennawi, J. F., Strauss, M. A., Oguri, M., Inada, N., Richards, G. T., Pindor, B., Schneider, D. P., Becker, R. H., Gregg, M. D., Hall, P. B., Johnston, D. E., Fan, X., Burles, S., Schlegel, D. J., Gunn, J. E., Lupton, R. H., Bahcall, N. A., Brunner, R. J., & Brinkmann, J. 2006b, *AJ*, 131, 1
- Henry, R. B. C., Edmunds, M. G., & Köppen, J. 2000, *ApJ*, 541, 660
- Hodapp, K. W., Jensen, J. B., Irwin, E. M., Yamada, H., Chung, R., Fletcher, K., Robertson, L., Hora, J. L., Simons, D. A., Mays, W., Nolan, R., Bec, M., Merrill, M., & Fowler, A. M. 2003, *PASP*, 115, 1388
- Hopkins, P. F., Cox, T. J., Kereš, D., & Hernquist, L. 2008, *ApJS*, 175, 390
- Hopkins, P. F., Hernquist, L., Martini, P., Cox, T. J., Robertson, B., Di Matteo, T., & Springel, V. 2005, *ApJ*, 625, L71
- Humphrey, A., Villar-Martín, M., Fosbury, R., Binette, L., Vernet, J., De Breuck, C., & di Serego Alighieri, S. 2007, *MNRAS*, 375, 705
- Jakobsen, P., Jansen, R. A., Wagner, S., & Reimers, D. 2003, *A&A*, 397, 891
- Johnson, S. D., Chen, H.-W., & Mulchaey, J. S. 2015, *MNRAS*, 452, 2553
- Jones, A., Noll, S., Kausch, W., Szyszka, C., & Kimeswenger, S. 2013, *A&A*, 560, A91
- Kereš, D., Katz, N., Weinberg, D. H., & Davé, R. 2005, *MNRAS*, 363, 2
- Kimm, T., Somerville, R. S., Yi, S. K., van den Bosch, F. C., Salim, S., Fontanot, F., Monaco, P., Mo, H., Pasquali, A., Rich, R. M., & Yang, X. 2009, *MNRAS*, 394, 1131
- Kirkman, D., & Tytler, D. 1997, *ApJ*, 484, 672
- . 2008, *MNRAS*, 391, 1457
- Konami, S., Matsushita, K., Nagino, R., & Tamagawa, T. 2014, *ApJ*, 783, 8
- Kormendy, J., & Richstone, D. 1995, *ARA&A*, 33, 581
- Kravtsov, A. V., & Borgani, S. 2012, *ARA&A*, 50, 353
- Lanzetta, K. M., Bowen, D. V., Tytler, D., & Webb, J. K. 1995, *ApJ*, 442, 538
- Lee, K.-G., Suzuki, N., & Spergel, D. N. 2012, *AJ*, 143, 51
- Loewenstein, M., & Davis, D. S. 2010, *ApJ*, 716, 384
- . 2012, *ApJ*, 757, 121
- Lu, Y., Mo, H. J., Katz, N., & Weinberg, M. D. 2012, *MNRAS*, 421, 1779
- Markwardt, C. B. 2009, in *Astronomical Society of the Pacific Conference Series*, Vol. 411, *Astronomical Data Analysis Software and Systems XVIII*, ed. D. A. Bohlender, D. Durand, & P. Dowler, 251
- Martin, C. L. 2005, *ApJ*, 621, 227
- Martin, D. C., Chang, D., Matuszewski, M., Morrissey, P., Rahman, S., Moore, A., & Steidel, C. C. 2014, *ApJ*, 786, 106
- Martini, P. 2004, in *Coevolution of Black Holes and Galaxies*, ed. L. C. Ho, 169+
- Martini, P., & Weinberg, D. H. 2001, *ApJ*, 547, 12
- Matteucci, F. 1994, *A&A*, 288, 57
- McLean, I. S., Becklin, E. E., Bendiksen, O., Brims, G., Canfield, J., Figer, D. F., Graham, J. R., Hare, J., Lacayanga, F., Larkin, J. E., Larson, S. B., Levenson, N., Magnone, N., Teplitz, H., & Wong, W. 1998, in *Society of Photo-Optical Instrumentation Engineers (SPIE) Conference Series*, Vol. 3354, *Infrared Astronomical Instrumentation*, ed. A. M. Fowler, 566–578
- Meiksin, A., Bolton, J. S., & Tittley, E. R. 2015, *MNRAS*, 453, 899
- Moehler, S., Modigliani, A., Freudling, W., Giammichele, N., Gianninas, A., Gonneau, A., Kausch, W., Lançon, A., Noll, S., Rauch, T., & Vinther, J. 2014, *A&A*, 568, A9
- Mushotzky, R., Loewenstein, M., Arnaud, K. A., Tamura, T., Fukazawa, Y., Matsushita, K., Kikuchi, K., & Hatsukade, I. 1996, *ApJ*, 466, 686
- Muzahid, S., Kacprzak, G. G., Churchill, C. W., Charlton, J. C., Nielsen, N. M., Mathes, N. L., & Trujillo-Gomez, S. 2015, *ApJ*, 811, 132
- Navarro, J. F., Frenk, C. S., & White, S. D. M. 1997, *ApJ*, 490, 493
- Neeleman, M., Wolfe, A. M., Prochaska, J. X., & Rafelski, M. 2013, *ApJ*, 769, 54
- Noll, S., Kausch, W., Barden, M., Jones, A. M., Szyszka, C., Kimeswenger, S., & Vinther, J. 2012, *A&A*, 543, A92
- Nomoto, K., Tominaga, N., Umeda, H., Kobayashi, C., & Maeda, K. 2006, *Nuclear Physics A*, 777, 424
- Oosterloo, T., Fraternali, F., & Sancisi, R. 2007, *AJ*, 134, 1019
- Oosterloo, T., & van Gorkom, J. 2005, *A&A*, 437, L19
- Oppenheimer, B. D., & Schaye, J. 2013, *MNRAS*, 434, 1063
- Peeples, M. S., Werk, J. K., Tumlinson, J., Oppenheimer, B. D., Prochaska, J. X., Katz, N., & Weinberg, D. H. 2014, *ApJ*, 786, 54
- Porciani, C., Magliocchetti, M., & Norberg, P. 2004, *MNRAS*, 355, 1010
- Prochaska, J. X. 1999, *ApJ*, 511, L71
- Prochaska, J. X., Chen, H.-W., & Bloom, J. S. 2006, *ApJ*, 648, 95
- Prochaska, J. X., & Hennawi, J. F. 2009, *ApJ*, 690, 1558
- Prochaska, J. X., Hennawi, J. F., Lee, K.-G., Cantalupo, S., Bovy, J., Djorgovski, S. G., Ellison, S. L., Lau, M. W., Martin, C. L., Myers, A., Rubin, K. H. R., & Simcoe, R. A. 2013a, *ApJ*, 776, 136
- Prochaska, J. X., Hennawi, J. F., & Simcoe, R. A. 2013b, *ApJ*, 762, L19
- Prochaska, J. X., Lau, M. W., & Hennawi, J. F. 2014, *ApJ*, 796, 140
- Prochaska, J. X., O'Meara, J. M., Fumagalli, M., Bernstein, R. A., & Burles, S. M. 2015, *ApJS*, 221, 2
- Prochaska, J. X., Weiner, B., Chen, H.-W., Mulchaey, J., & Cooksey, K. 2011, *ApJ*, 740, 91
- Prochaska, J. X., & Wolfe, A. M. 1997, *ApJ*, 487, 73
- Rahmati, A., Schaye, J., Bower, R. G., Crain, R. A., Furlong, M., Schaller, M., & Theuns, T. 2015, *MNRAS*, 452, 2034
- Richards, G. T., Vanden Berk, D. E., Reichard, T. A., Hall, P. B., Schneider, D. P., SubbaRao, M., Thakar, A. R., & York, D. G. 2002, *AJ*, 124, 1
- Rosario, D. J., Trakhtenbrot, B., Lutz, D., Netzer, H., Trump, J. R., Silverman, J. D., Schramm, M., Lusso, E., Berta, S., Bongiorno, A., Brusa, M., Förster-Schreiber, N. M., Genzel, R., Lilly, S., Magnelli, B., Mainieri, V., Maiolino, R., Merloni, A., Mignoli, M., Nordon, R., Popesso, P., Salvato, M., Santini, P., Tacconi, L. J., & Zamorani, G. 2013, *A&A*, 560, A72
- Rosdahl, J., & Blaizot, J. 2012, *MNRAS*, 423, 344
- Rubin, K. H. R., Prochaska, J. X., Koo, D. C., Phillips, A. C., Martin, C. L., & Winstrom, L. O. 2014, *ApJ*, 794, 156
- Rubin, K. H. R., Weiner, B. J., Koo, D. C., Martin, C. L., Prochaska, J. X., Coil, A. L., & Newman, J. A. 2010, *ApJ*, 719, 1503
- Rudie, G. C., Steidel, C. C., Trainor, R. F., Rakic, O., Bogosavljević, M., Pettini, M., Reddy, N., Shapley, A. E., Erb, D. K., & Law, D. R. 2012, *ApJ*, 757, 67
- Rupke, D. S., Veilleux, S., & Sanders, D. B. 2005, *ApJS*, 160, 115
- Sargent, W. L. W., Young, P. J., Boksenberg, A., Carswell, R. F., & Whelan, J. A. J. 1979, *ApJ*, 230, 49
- Sato, K., Yamasaki, N. Y., Ishida, M., Ishisaki, Y., Ohashi, T., Kawahara, H., Kitaguchi, T., Kawaharada, M., Kokubun, M., Makishima, K., Ota, N., Nakazawa, K., Tamura, T., Matsushita, K., Kawano, N., Fukazawa, Y., & Hughes, J. P. 2007, *PASJ*, 59, 299
- Savage, B. D., & Sembach, K. R. 1991, *ApJ*, 379, 245
- Scannapieco, E., & Oh, S. P. 2004, *ApJ*, 608, 62
- Shen, Y., & Ho, L. C. 2014, *Nature*, 513, 210

- Shen, Y., Horne, K., Grier, C. J., Peterson, B. M., Denney, K. D., Trump, J. R., Sun, M., Brandt, W. N., Kochanek, C. S., Dawson, K. S., Green, P. J., Greene, J. E., Hall, P. B., Ho, L. C., Jiang, L., Kinemuchi, K., McGreer, I. D., Petitjean, P., Richards, G. T., Schneider, D. P., Strauss, M. A., Tao, C., Wood-Vasey, W. M., Zu, Y., Pan, K., Bizyaev, D., Ge, J., Oravetz, D., & Simmons, A. 2016, *ApJ*, 818, 30
- Silva, A. I., & Viegas, S. M. 2002, *MNRAS*, 329, 135
- Simcoe, R. A., Sargent, W. L. W., & Rauch, M. 2002, *ApJ*, 578, 737
- . 2004, *ApJ*, 606, 92
- Simcoe, R. A., Sargent, W. L. W., Rauch, M., & Becker, G. 2006, *ApJ*, 637, 648
- Simionescu, A., Werner, N., Urban, O., Allen, S. W., Ichinohe, Y., & Zhuravleva, I. 2015, *ApJ*, 811, L25
- Steidel, C. C., Erb, D. K., Shapley, A. E., Pettini, M., Reddy, N., Bogosavljević, M., Rudie, G. C., & Rakic, O. 2010, *ApJ*, 717, 289
- Stockton, A., MacKenty, J. W., Hu, E. M., & Kim, T.-S. 2002, *ApJ*, 572, 735
- Sukhbold, T., Ertl, T., Woosley, S. E., Brown, J. M., & Janka, H.-T. 2016, *ApJ*, 821, 38
- Sutherland, R. S., & Dopita, M. A. 1993, *ApJS*, 88, 253
- Thomas, D. 1999, *MNRAS*, 306, 655
- Tinsley, B. M. 1979, *ApJ*, 229, 1046
- Tormen, G. 1997, *MNRAS*, 290, 411
- Trager, S. C., Faber, S. M., Worthey, G., & González, J. J. 2000, *AJ*, 120, 165
- Tripp, T. M., Meiring, J. D., Prochaska, J. X., Willmer, C. N. A., Howk, J. C., Werk, J. K., Jenkins, E. B., Bowen, D. V., Lehner, N., Sembach, K. R., Thom, C., & Tumlinson, J. 2011, *Science*, 334, 952
- Tripp, T. M., Sembach, K. R., Bowen, D. V., Savage, B. D., Jenkins, E. B., Lehner, N., & Richter, P. 2008, *ApJS*, 177, 39
- Trump, J. R., Hall, P. B., Reichard, T. A., Richards, G. T., Schneider, D. P., Vanden Berk, D. E., Knapp, G. R., Anderson, S. F., Fan, X., Brinkman, J., Kleinman, S. J., & Nitta, A. 2006, *ApJS*, 165, 1
- Tumlinson, J., Thom, C., Werk, J. K., Prochaska, J. X., Tripp, T. M., Katz, N., Davé, R., Oppenheimer, B. D., Meiring, J. D., Ford, A. B., O'Meara, J. M., Peebles, M. S., Sembach, K. R., & Weinberg, D. H. 2013, *ApJ*, 777, 59
- Tumlinson, J., Thom, C., Werk, J. K., Prochaska, J. X., Tripp, T. M., Weinberg, D. H., Peebles, M. S., O'Meara, J. M., Oppenheimer, B. D., Meiring, J. D., Katz, N. S., Davé, R., Ford, A. B., & Sembach, K. R. 2011, *Science*, 334, 948
- Turner, M. L., Schaye, J., Steidel, C. C., Rudie, G. C., & Strom, A. L. 2014, *MNRAS*, 445, 794
- Vernet, J., Dekker, H., D'Odorico, S., Kaper, L., Kjaergaard, P., Hammer, F., Randich, S., Zerbi, F., Groot, P. J., Hjorth, J., Guinouard, I., Navarro, R., Adolfse, T., Albers, P. W., Amans, J.-P., Andersen, J. J., Andersen, M. I., Binetruy, P., Bristow, P., Castillo, R., Chemla, F., Christensen, L., Conconi, P., Conzelmann, R., Dam, J., de Caprio, V., de Ugarte Postigo, A., Delabre, B., di Marcantonio, P., Downing, M., Elswijk, E., Finger, G., Fischer, G., Flores, H., François, P., Goldoni, P., Guglielmi, L., Haignon, R., Hanenburg, H., Hendriks, I., Horrobin, M., Horville, D., Jessen, N. C., Kerber, F., Kern, L., Kiebusch, M., Kleszcz, P., Klougart, J., Kragt, J., Larsen, H. H., Lizon, J.-L., Lucuix, C., Mainieri, V., Manuputy, R., Martayan, C., Mason, E., Mazzoleni, R., Michaelsen, N., Modigliani, A., Moehler, S., Möller, P., Norup Sørensen, A., Nørregaard, P., Péroux, C., Patat, F., Pena, E., Pragat, J., Reinero, C., Rigal, F., Riva, M., Roelfsema, R., Royer, F., Sacco, G., Santin, P., Schoenmaker, T., Spano, P., Sweers, E., Ter Horst, R., Tintori, M., Tromp, N., van Dael, P., van der Vliet, H., Venema, L., Vidali, M., Vinther, J., Vola, P., Winters, R., Wistisen, D., Wulterkens, G., & Zacchei, A. 2011, *A&A*, 536, A105
- Vikas, S., Wood-Vasey, W. M., Lundgren, B., Ross, N. P., Myers, A. D., AlSaiyad, Y., York, D. G., Schneider, D. P., Brinkmann, J., Bizyaev, D., Brewington, H., Ge, J., Malanushenko, E., Malanushenko, V., Muna, D., Oravetz, D., Pan, K., Pâris, I., Petitjean, P., Snedden, S., Shelden, A., Simmons, A., & Weaver, B. A. 2013, *ApJ*, 768, 38
- Werk, J. K., Prochaska, J. X., Thom, C., Tumlinson, J., Tripp, T. M., O'Meara, J. M., & Peebles, M. S. 2013, *ApJS*, 204, 17
- Werk, J. K., Prochaska, J. X., Tumlinson, J., Peebles, M. S., Tripp, T. M., Fox, A. J., Lehner, N., Thom, C., O'Meara, J. M., Ford, A. B., Bordoloi, R., Katz, N., Tejos, N., Oppenheimer, B. D., Davé, R., & Weinberg, D. H. 2014, *ApJ*, 792, 8
- Weymann, R. J., Morris, S. L., Foltz, C. B., & Hewett, P. C. 1991, *ApJ*, 373, 23
- Whitaker, K. E., Franx, M., Leja, J., van Dokkum, P. G., Henry, A., Skelton, R. E., Fumagalli, M., Momcheva, I. G., Brammer, G. B., Labbé, I., Nelson, E. J., & Rigby, J. R. 2014, *ApJ*, 795, 104
- White, M., Myers, A. D., Ross, N. P., Schlegel, D. J., Hennawi, J. F., Shen, Y., McGreer, I., Strauss, M. A., Bolton, A. S., Bovy, J., Fan, X., Miralda-Escude, J., Palanque-Delabrouille, N., Paris, I., Petitjean, P., Schneider, D. P., Viel, M., Weinberg, D. H., Yèche, C., Zehavi, I., Pan, K., Snedden, S., Bizyaev, D., Brewington, H., Brinkmann, J., Malanushenko, V., Malanushenko, E., Oravetz, D., Simmons, A., Sheldon, A., & Weaver, B. A. 2012, *MNRAS*, 424, 933
- Wolfe, A. M., & Prochaska, J. X. 2000, *ApJ*, 545, 603
- Zahedy, F. S., Chen, H.-W., Rauch, M., Wilson, M. L., & Zabludoff, A. 2016, *MNRAS*, 458, 2423